J. Fluid Mech. (2023), *vol*. 962, A38, doi:10.1017/jfm.2023.260

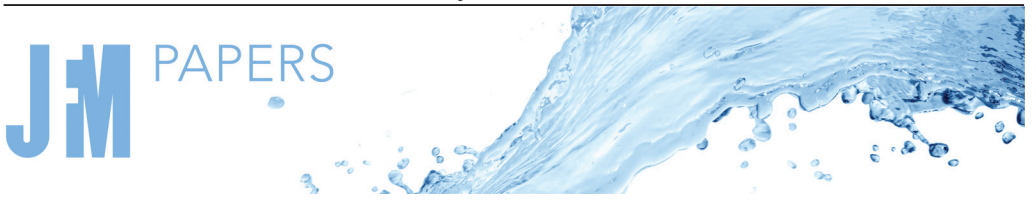

Neural-network-based mixed subgrid-scale model for turbulent flow

Myeongseok Kang[1],‡, **Youngmin Jeon**[1],‡ **and Donghyun You**[1],†

[1]Department of Mechanical Engineering, Pohang University of Science and Technology, 77 Cheongam-ro, Nam-gu, Pohang, Gyeongbuk 37673, Republic of Korea

(Received 6 September 2022; revised 17 March 2023; accepted 21 March 2023)

An artificial neural-network-based subgrid-scale (SGS) model, which is capable of predicting turbulent flows at untrained Reynolds numbers and on untrained grid resolution is developed. Providing the grid-scale strain-rate tensor alone as an input leads the model to predict a SGS stress tensor that aligns with the strain-rate tensor, and the model performs similarly to the dynamic Smagorinsky model. On the other hand, providing the resolved stress tensor as an input in addition to the strain-rate tensor is found to significantly improve the prediction of the SGS stress and dissipation, and thereby the accuracy and stability of the solution. In an attempt to apply the neural-network-based model trained for turbulent flows with a limited range of the Reynolds number and grid resolution to turbulent flows at untrained conditions on untrained grid resolution, special attention is given to the normalisation of the input and output tensors. It is found that the successful generalization of the model to turbulence for various untrained conditions and resolution is possible if distributions of the normalised inputs and outputs of the neural network remain unchanged as the Reynolds number and grid resolution vary. In *a posteriori* tests of the forced and the decaying homogeneous isotropic turbulence and turbulent channel flows, the developed neural-network model is found to predict turbulence statistics more accurately, maintain the numerical stability without *ad hoc* stabilisation such as clipping of the excessive backscatter, and to be computationally more efficient than the algebraic dynamic SGS models.

Key words: turbulence modelling, turbulence simulation

1. Introduction

Large-eddy simulation (LES) is a technique in which large-scale turbulent motions are directly resolved on the computational grid while the effect of filtered subgrid-scale (SGS)

† Email address for correspondence: dhyou@postech.ac.kr
‡ Co-first author.

turbulent motions are modelled using an SGS model. In order to model the dissipative nature of the SGS stress tensor, which is known to be the essential component of the SGS modelling (Liu, Meneveau & Katz 1994), eddy-viscosity SGS models are often utilised (Smagorinsky 1963; Lilly 1967; Germano *et al.* 1991; Vreman 2004; Silvis, Remmerswaal & Verstappen 2017). In eddy-viscosity SGS models the deviatoric part of the SGS stress tensor τ_{ij} is modelled as an algebraic function of the resolved strain-rate tensor $\bar{S}_{ij}$ such that $\tau_{ij} - \frac{1}{3}\tau_{kk}\delta_{ij} = -2\nu_t\bar{S}_{ij}$, where $\overline{(\cdot)}$ denotes the spatial filter operation, S_{ij} is the strain-rate tensor, δ_{ij} is the Kronecker delta and ν_t denotes the eddy viscosity (Silvis *et al.* 2017). While ν_t is modelled as $C\Pi^g$, where C and Π^g are the model coefficient and the SGS kernel at the grid-filter level, respectively, the dynamic procedure developed by Germano *et al.* (1991) enabled dynamic determination of C.

However, eddy-viscosity SGS models have the shortcoming that they correlate poorly with the true SGS stress tensor since eddy-viscosity models are aligned with $\bar{S}_{ij}$ (Bardina, Ferziger & Reynolds 1983; Anderson & Meneveau 1999; da Silva & Métais 2002) and are not able to predict backscatter to the resolved scales (Zang, Street & Koseff 1993). To alleviate the problems, various mixed SGS models that combine eddy-viscosity models with the modified Leonard term (Zang *et al.* 1993; Bardina *et al.* 1983; Germano 1986), the resolved stress $L_{ij}(=\widehat{\bar{u}_i\bar{u}_j} - \hat{\bar{u}}_i\hat{\bar{u}}_j)$ (Anderson & Meneveau 1999; Liu *et al.* 1994) and the Clark model (Anderson & Meneveau 1999) were proposed. The dynamic procedure (Germano *et al.* 1991) was also applied to one-parameter (Zang *et al.* 1993) and two-parameter (Liu *et al.* 1994; Salvetti & Banerjee 1995; Anderson & Meneveau 1999) mixed models, where the parameter refers to the model coefficients. Although dynamic mixed models are reported to exhibit smaller fluctuations in model coefficients, dynamic eddy-viscosity models and dynamic mixed models require *ad hoc* procedures such as averaging of model coefficients in statistically homogeneous directions and clipping of negative model coefficients (Zang *et al.* 1993; Salvetti & Banerjee 1995) to avoid numerical instability. Despite this issue, dynamic eddy-viscosity and dynamic mixed models have been successfully applied to various turbulent flows (Germano *et al.* 1991; Zang *et al.* 1993; Salvetti & Banerjee 1995; Anderson & Meneveau 1999; Vreman 2004; Silvis *et al.* 2017).

Recently, there have been studies to develop SGS models using an artificial neural network (ANN) (Wang *et al.* 2018; Xie & Wang 2019; Xie *et al.* 2019; Xie, Wang & Weinan 2020*a*; Xie, Yuan & Wang 2020*b*; Yuan, Xie & Wang 2020). An ANN constructs a nonlinear mapping between a set of resolved flow variables and unresolved SGS stress using a series of matrix multiplications and nonlinear activation functions, while the conventional models represent the SGS stress in an algebraic function of resolved flow variables. As a result, ANN-based models are often expected to provide a more accurate flow description than algebraic dynamic SGS models (Xie & Wang 2019; Xie *et al.* 2019, 2020*a*). For instance, Xie *et al.* (2020*a*) showed from an *a posteriori* test of forced homogeneous isotropic turbulence that their ANN-based model predicted the energy spectrum and probability density functions (p.d.f.s) of the vorticity and velocity increment more accurately than the dynamic Smagorinsky model (DSM) and the dynamic mixed model. The ANN-based SGS models (hereafter ANN-SGS models) are also often known to be free from *ad hoc* procedures such as averaging and clipping of model coefficients for a certain set of input variables, which will be discussed later (Wang *et al.* 2018; Xie & Wang 2019; Xie *et al.* 2019, 2020*a*,*b*; Yuan *et al.* 2020). Therefore, ANN-SGS models have the potential to be not only free from the requirement of a statistically homogeneous direction but also provide improved prediction of the SGS stress.

Despite such potentially favourable features, ANN-SGS models raise three issues. The first issue is that although the performance of ANN-based models is known to be sensitive to the types of variables and the number of data points used for inputs, there is still no general consensus on which input variables and how many data points for each input variable are appropriate (Wang *et al.* 2018; Xie & Wang 2019; Xie *et al.* 2019, 2020*a*; Park & Choi 2021). Wang *et al.* (2018) performed an *a priori* study of decaying homogeneous isotropic turbulence to test the utility of single-point input variables such as the filtered velocity vector $\bar{u}_i$, the velocity gradient tensor $\partial\bar{u}_i/\partial x_j$ and the second-order velocity derivative $\partial^2\bar{u}_i/(\partial x_j\partial x_k)$. They found that $\partial\bar{u}_i/\partial x_j$ and $\bar{u}_i$ were the most and least important, respectively, for predictive accuracy. Xie *et al.* (2020*a*) found that the multi-point input $\partial\bar{u}_i/\partial x_j$ led to higher correlation coefficients between the true and predicted SGS stresses than the single-point input $\partial\bar{u}_i/\partial x_j$ from an *a priori* study of forced homogeneous isotropic turbulence.

Park & Choi (2021), on the other hand, tested both single-point and multi-point resolved strain-rate tensors $\bar{S}_{ij}$ and $\partial\bar{u}_i/\partial x_j$ as inputs for ANN-based LES of a turbulent channel flow and found from an *a posteriori* test that the use of multi-point inputs required backscatter clipping due to numerical instabilities, while the use of single point $\bar{S}_{ij}$ resulted in the best performance. These are interesting results because, firstly, the use of a single-point input was essential for numerical stability, at least in the case of near-wall turbulence; secondly, the elaborate selection of input variables such as $\bar{S}_{ij}$ led to a better performance of ANN-SGS models than the use of general input variables such as $\bar{u}_i$ or $\partial\bar{u}_i/\partial x_j$.

Based on the knowledge from the algebraic SGS modelling in the framework of mixed modelling and from the recent reports on the selection of input variables and the number of input points, it is expected that an improved ANN-SGS model can be designed. For example, the drawback associated with misalignment of the SGS stress tensor can be overcome in a numerically stable manner by forming an ANN-based mixed model that utilises both the resolved strain-rate tensor and the resolved stress $L_{ij}(=\widehat{\bar{u}_i\bar{u}_j}-\hat{\bar{u}}_i\hat{\bar{u}}_j)$ (Liu *et al.* 1994; Anderson & Meneveau 1999) as inputs at a single point.

The second issue for ANN-based models is the generalization to untrained flow conditions, untrained grid resolution, and untrained types of flow. A few studies have reported application of an ANN-based model that was trained for a certain flow at low Reynolds numbers to the same flow at untrained higher Reynolds numbers (Maulik *et al.* 2018, 2019; Park & Choi 2021). However, generalization to flow on an untrained grid resolution has not been successful. Park & Choi (2021) reported that an ANN-based model trained at a certain grid resolution did not accurately predict the turbulent statistics on untrained coarser or finer resolution, while it was possible to predict flow on an untrained grid resolution when the network was trained on coarser and finer resolution than the target resolution. Similarly, Zhou *et al.* (2019) reported that predicting turbulent flow on a different grid resolution was difficult using an ANN-based model trained on other than the target grid resolution.

Most studies on ANN-based models addressed application of an ANN trained for a particular type of flow to the same type of flow. Although Xie *et al.* (2020*a*,*b*) briefly discussed application of ANN-based models trained with forced homogeneous isotropic turbulence to weakly compressible homogeneous shear flow, both flows are statistically stationary at the same Reynolds number and on the same grid resolution. Therefore, it is important to identify conditions of inputs and outputs of an ANN to achieve better generalization to flow on a different grid resolution and eventually to a different type of flow from trained flows.

The last issue is that the computational cost of ANN-based models has been reported to be higher than that of the algebraic dynamic eddy-viscosity and the dynamic mixed models. Park & Choi (2021), Wang *et al.* (2018), Yuan *et al.* (2020), Xie & Wang (2019) and Xie *et al.* (2020*a*) reported 1.3, 1.8, 2.4, 15 and 256 times higher computational cost than that of the DSM for simulations of turbulent channel flow (Park & Choi 2021) and homogeneous isotropic turbulence (Wang *et al.* 2018; Xie & Wang 2019; Xie *et al.* 2020*a*; Yuan *et al.* 2020), respectively. Yuan *et al.* (2020), Xie & Wang (2019) and Xie *et al.* (2020*a*) also reported that the computational cost of their ANN-based models is higher than that of the dynamic mixed model (Anderson & Meneveau 1999). To make ANN-SGS models be practical, both accuracy and computational efficiency that are superior to those of the conventional algebraic SGS models should be achieved.

The primary objective of the present study is to develop a new ANN-based mixed SGS model that predicts the SGS stress tensor more accurately and stably. Analogously to the philosophy of the algebraic mixed SGS models, the present model is designed to consider both the resolved stress and strain-rate tensors as inputs and thereby produce the SGS stress associated with both the inputs as an output. The new model is also designed to be applicable to turbulent flow at untrained Reynolds numbers and on an untrained grid resolution, and, at the same time, to be computationally more efficient than the conventional algebraic SGS models. As noted by Park & Choi (2021), the numerical stability is sought by conducting the input–output data sampling on a single grid point. The single-point data sampling is also beneficial in minimizing the computational cost. To achieve the goal, extensive analyses for finding optimal input–output scalings are conducted through *a priori* and *a posteriori* tests of homogeneous isotropic turbulence. The predictive capability, accuracy and stability of the ANN-based mixed SGS model for LES of homogeneous isotropic turbulence at untrained Reynolds numbers as well as on an untrained grid resolution are evaluated in detail. The applicability to other types of turbulent flow, especially the wall-bounded turbulent flow is investigated by performing LES of a turbulent channel flow.

This paper is organised as follows. Numerical methods for direct numerical simulation (DNS), LES and ANN are presented in § 2. In § 3 the performance and the characteristics of ANN-SGS models with different input sets are discussed based on results of *a priori* and *a posteriori* tests of forced isotropic turbulence. Application of the present ANN-based mixed SGS model to decaying isotropic turbulence at untrained Reynolds numbers and on an untrained grid resolution and untrained turbulent channel flow are presented in § 3. Comparison of the predictive capability as well as the computational cost of the developed ANN-based mixed SGS model with those of algebraic dynamic mixed models are also discussed in § 3, followed by concluding remarks in § 4.

2. Numerical methods

2.1. *Direct numerical simulation of forced homogeneous isotropic turbulence*

The incompressible Navier–Stokes equations for DNS are

$$\frac{\partial u_i}{\partial x_i} = 0, \tag{2.1}$$

$$\frac{\partial u_i}{\partial t} + \frac{\partial u_i u_j}{\partial x_j} = -\frac{1}{\rho}\frac{\partial p}{\partial x_i} + \nu \frac{\partial^2 u_i}{\partial x_j \partial x_j}, \tag{2.2}$$

Re_λ	N	ν	ε_p	k_f	η	ηk_{max}	N_S
106	192	1/263	1.0	2.0	1.5×10^{-2}	1.4	37
164	256	1/150	62.9	3.0	8.4×10^{-3}	1.0	50
286	512	1/2225	0.12	1.5	5.3×10^{-3}	1.3	50

Table 1. Parameters for DNS of forced homogeneous isotropic turbulence. Here Re_λ is the Taylor-scale Reynolds number, N is the number of grid points in each direction, ν is the viscosity, ε_p is the prescribed dissipation rate, k_f is the upper bound of the forcing wavenumber, η is the Kolmogorov length scale and k_{max} is the maximum resolved wavenumber.

where x_i $(= x, y, z)$ are the Cartesian coordinates, u_i $(= u, v, w)$ are the corresponding velocity components, t is time, p is pressure, ρ is density and ν is kinematic viscosity.

Forced homogeneous isotropic turbulence at $Re_\lambda = 106$, 164 and 286, which were simulated by Mohan, Fitzsimmons & Moser (2017), Langford & Moser (1999) and Chumakov (2008), respectively, are simulated in this study with the computational parameters shown in table 1. A pseudospectral code HIT3D (Chumakov 2007, 2008) is used to solve the incompressible Navier–Stokes equations in a periodic cubic box with the length of 2π with N grid points in each direction. Simulation results are quoted in arbitrary units (Yang & Lei 1998; Langford & Moser 1999; Meneguz & Reeks 2011) of each case (Langford & Moser 1999; Chumakov 2008; Mohan *et al.* 2017) in which the domain size is 2π. A combination of spherical truncation and phase shifting (Canuto *et al.* 1988) is used for dealiasing. The second-order Adams–Bashforth scheme is used for time integration (Kang & You 2021).

The initial flow field of the Gaussian distribution and random phases is fully developed, and then instantaneous fields are sampled at every eddy turnover time. The number of samples N_S for each case is summarized in table 1. Validation of the present DNS is discussed in the following section.

2.2. *Validation of DNS results*

Mohan *et al.* (2017) and Langford & Moser (1999) used a negative viscosity forcing (Jiménez *et al.* 1993; Mohan *et al.* 2017) for forced homogeneous isotropic turbulence at $Re_\lambda = 106$ and 164, respectively, and Chumakov (2008) used a deterministic forcing (Machiels 1997) for forced homogeneous isotropic turbulence at $Re_\lambda = 286$. The negative viscosity forcing is given as

$$\hat{f}_i^V(\boldsymbol{k}, t) = \begin{cases} \varepsilon_p \hat{u}_i |\boldsymbol{k}|^2(\boldsymbol{k}, t) / \left[2E_f^V(t)\right], & 0 < k \leqslant k_f, \\ 0, & k_f < k, \end{cases} \tag{2.3}$$

where ε_p denotes the prescribed mean dissipation rate, k is the spherical wavenumber defined as $k = |\boldsymbol{k}|$, k_f is the upper bound of the forcing wavenumber and $E_f^V(t) = \int_0^{k_f} |\boldsymbol{k}|^2 E(k, t)\, \mathrm{d}k$, where $E(k, t)$ is the energy spectrum at time t. The combined forcing and viscous term in the Fourier space becomes $-(\nu - \alpha)|\boldsymbol{k}|^2 \hat{u}_i(\boldsymbol{k})$, where $\alpha = \varepsilon_p / [2E_f^V(t)]$.

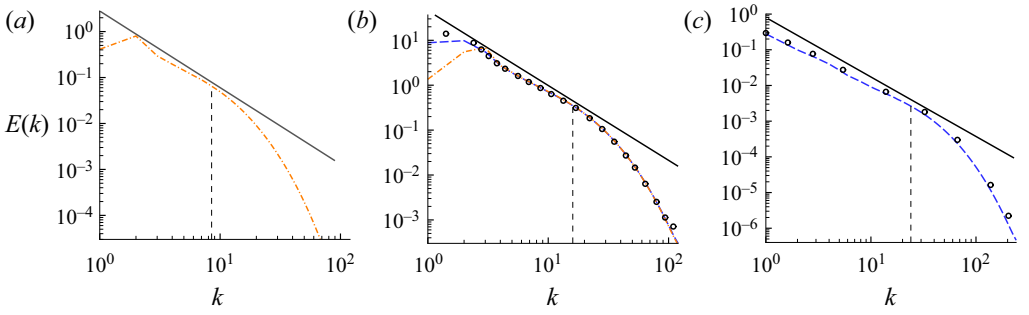

Figure 1. Energy spectra from DNS of forced homogeneous isotropic turbulence at (*a*) $Re_\lambda = 106$, (*b*) $Re_\lambda = 164$ and (*c*) $Re_\lambda = 286$. The open circles, ∘, represent DNS by (*b*) Langford & Moser (1999) and (*c*) Chumakov (2008); – – – (yellow orange dashed-dot line) represents the present DNS with the negative viscosity forcing; – – - (dark blue dashed line) represents the present DNS with the deterministic forcing of Machiels; —— (black line) represents the $k^{-5/3}$ line; vertical dashed lines indicate the grid-filter cutoff wavenumbers in the inertial subrange in which *a priori* tests are performed.

The deterministic forcing of Machiels (1997) is given as

$$\hat{f}_i^M(\boldsymbol{k}, t) = \begin{cases} \varepsilon_p \hat{u}_i(\boldsymbol{k}, t) / \left[2E_f^M(t)\right], & 0 < k \leqslant k_f, \\ 0, & k_f < k, \end{cases} \tag{2.4}$$

where $E_f^M(t) = \int_0^{k_f} E(k, t)\,\mathrm{d}k$.

Three-dimensional energy spectra of forced homogeneous isotropic turbulence are compared with the reference DNS results in figure 1, except for the case at $Re_\lambda = 106$ for which a reference energy spectrum is not available. The case at $Re_\lambda = 164$ is firstly simulated using the negative viscosity forcing following Langford & Moser (1999). The resulting energy spectrum shown in figure 1(*b*) exhibits an undershoot in the forcing wavenumber range. Another simulation at $Re_\lambda = 164$ with the deterministic forcing of Machiels, on the other hand, shows improved agreement with the reference DNS data in the forcing range. While the differences caused by the use of different forcing schemes are further discussed in Appendix A, DNS data obtained using the deterministic forcing of Machiels is used for analyses in the present study, as it better reproduces DNS results of Langford & Moser (1999). For the case of $Re_\lambda = 286$, a slight underprediction of the energy spectrum is observed and it is discussed in Appendix B to conclude that the present DNS is statistically well converged.

2.3. *Large-eddy simulation and filter operations*

By applying the spatial filter operation $\overline{(\cdot)}$ to (2.1) and (2.2), the filtered Navier–Stokes equations for LES are obtained as

$$\frac{\partial \bar{u}_i}{\partial x_i} = 0, \tag{2.5}$$

$$\frac{\partial \bar{u}_i}{\partial t} + \frac{\partial \bar{u}_i \bar{u}_j}{\partial x_j} = -\frac{1}{\rho}\frac{\partial \bar{p}}{\partial x_i} + \nu \frac{\partial^2 \bar{u}_i}{\partial x_j \partial x_j} - \frac{\partial \tau_{ij}}{\partial x_j}, \tag{2.6}$$

where x_i $(= x, y, z)$ are the Cartesian coordinates, $\bar{u}_i$ $(= \bar{u}, \bar{v}, \bar{w})$ are the corresponding filtered velocity components, t is time, $\bar{p}$ is filtered pressure, ρ is density, ν is kinematic viscosity and $\tau_{ij} = \overline{u_i u_j} - \bar{u}_i \bar{u}_j$ is the SGS stress.

Low-pass spatial filter operations are defined at the grid- and test-filter levels. A grid-filter operation on a scalar variable $\bar{\phi}$ is defined as

$$\bar{\phi}(\boldsymbol{x}) = \int_{\Omega} G(\boldsymbol{x}, \boldsymbol{\xi})\, \phi(\boldsymbol{\xi})\, \mathrm{d}\boldsymbol{\xi}, \tag{2.7}$$

where $\boldsymbol{x}$ and $\boldsymbol{\xi}$ are the spatial coordinate vectors in the flow domain of Ω. The filter kernel G satisfies the normalisation condition and depends on the filter width defined as $\bar{\Delta}$ for the grid filter. The filter width in three-dimensional space is calculated using the expression given by Deardorff (1970),

$$\Delta = \sqrt[3]{\Delta_1 \Delta_2 \Delta_3}, \tag{2.8}$$

where Δ_i denotes the filter width in the i direction. In line with the definition of the grid filter in (2.7), a test-filter operator $\widehat{(\cdot)}$ is similarly defined but with the test-filter width $\hat{\Delta}$ instead of $\bar{\Delta}$.

The filter-to-grid ratio is defined as $\hat{\Delta}/\bar{\Delta}$, where $\hat{\Delta}$ is the filter width associated with the filtering operator $\widehat{(\cdot)}$. Since the Gaussian filter is adopted for both grid and test filters, the filter-to-grid ratio is set to $\sqrt{5}$ (Pope 2001). Moreover, because the implicit numerical grid filter for a pseudospectral method is known to be the Fourier cutoff filter, the grid-filter width is chosen to be twice the grid spacing in order to approximate the Gaussian filter (Kang, Chester & Meneveau 2003).

The Gaussian filter is chosen to be the representative of the graded filter of which the filter shape is similar to the implicit numerical filter shape of finite-difference and finite-volume methods that are more commonly used for simulations than the pseudospectral method. The reason for using the pseudospectral method in the present study is to minimize the effect of numerical errors. The top-hat filter also has been tested, but there are no considerable differences in the results.

2.4. *Artificial neural network for SGS modelling*

A fully connected neural network, also known as a multi-layer perceptron, is adopted in the present study. Six components of the SGS stress tensor τ_{ij} are predicted by an ANN from a set of filtered input variables. The ANN is trained using input and output data from the filtered DNS (fDNS) fields, which are obtained by applying a spatial filter to the instantaneous fields from DNS of forced homogeneous isotropic turbulence in § 2.1. The filter width of the fDNS dataset is the same as the grid size of LES with $N^3 = 48^3$ cells at $Re_\lambda = 106$, and $N^3 = 128^3$ cells at $Re_\lambda = 286$. Through sufficient training, the ANN constructs a nonlinear mapping between a set of inputs and a target SGS stress tensor using a series of linear matrix multiplications and nonlinear activation functions. The mathematical operation from the $(n-1)$th layer to the nth layer takes the form of

$$X_i^n = \sigma\left(\sum_j W_{ij}^n X_j^{n-1} + b_i^n\right), \tag{2.9}$$

where $\sigma(\cdot)$ is the activation function, and W_{ij}^n and b_i^n are weights and biases, respectively. The output layer is linearly activated as $X_i^N = \sum_j W_{ij}^N X_j^{N-1} + b_i^N$, where X_i^N is the output of the ANN.

The present ANN, which is shown in figure 2, consists of an input layer, 2 hidden layers with 12 neurons per hidden layer, and an output layer. Since the number of trainable

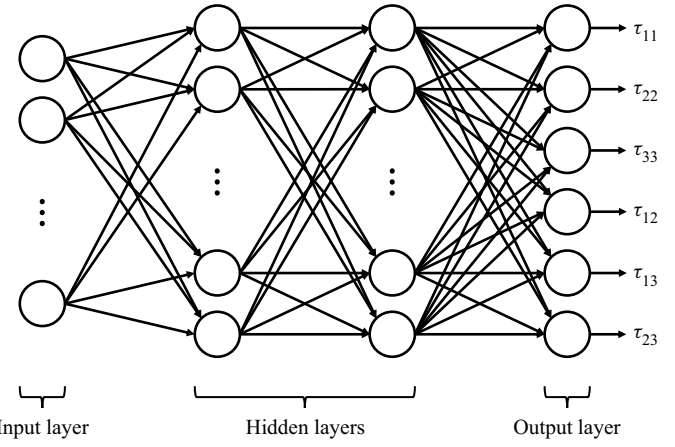

Figure 2. Schematic diagram of the ANN to predict the SGS stress (two hidden layers and 12 neurons per hidden layer).

parameters of an ANN directly affects its computational cost, a parameter study on the number of neurons per hidden layer is conducted in § 3.4. Based on the results in § 3.4, it is found that 12 neurons and 2 hidden layers are sufficient, and additional neurons or hidden layers do not improve the performance of the ANN. A Leaky–ReLu activation function ($\sigma(x) = \max[-0.02x, x]$) is applied at each hidden layer. Leaky–ReLu is known to perform better than ReLu (Xu *et al.* 2015), as it is capable of resolving the gradient vanishing problem of the ReLu. During the training process, weights W_{ij}^n and biases b_i^n are optimised to minimise the mean-squared error loss function for six components of τ_{ij} defined as

$$L = \frac{1}{N_{batch}} \frac{1}{6} \sum_{n=1}^{N_{batch}} \sum_{j=1}^{3} \sum_{i=1}^{j} \left(\tau_{ij,n}^{fDNS} - \tau_{ij,n} \right)^2, \tag{2.10}$$

where τ_{ij}^{fDNS} and τ_{ij} are the true SGS stress obtained from fDNS and the predicted SGS stress, respectively. Mini-batch training is utilised in the present study and the iteration in figure 3 represents the mini-batch iteration. In each mini-batch iteration a subset of the training dataset (i.e. mini batch) is utilised to update the weights and biases of the ANN. Here N_{batch} represents the size of the mini batch and is set to 128 (Park & Choi 2021).

The sets of input and output variables and Reynolds numbers of the training datasets for ANN-SGS models are listed in table 2. Each ANN-SGS model is named such that the character and the number represent the input variables and the Reynolds number at which the ANN is trained, respectively. The character H at the end of the model names denotes homogeneous isotropic turbulence. For example, S-106H uses six components of $\bar{S}_{ij}$ as inputs, whereas the other models use 12 components, six from $\bar{S}_{ij}$ and six from L_{ij}, as inputs. Effects of input variables on the characteristics and the accuracy of ANN-SGS models are discussed in § 3.1. In addition, the use of the resolved stress L_{ij} among various scale-similarity terms is discussed in Appendix C. The ANN-SGS models are trained with fDNS datasets of forced homogeneous isotropic turbulence at the given Reynolds number.

The Adam optimiser with a learning rate of 10^{-4} is utilised to optimise the trainable parameters. The ANN-SGS models listed in table 2 are trained for 5×10^5 iterations using the Python library PyTorch (Paszke *et al.* 2017). A total of 2×10^8 data points sampled from 30 snapshots of fDNS results are used for the training, whereas the rest are used

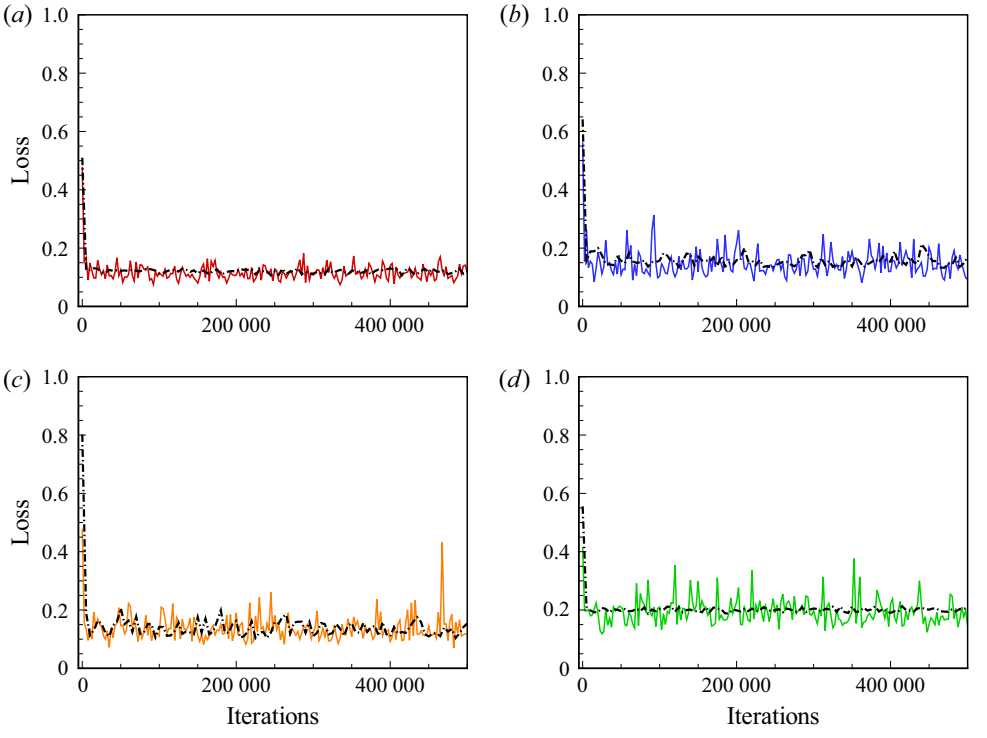

Figure 3. Learning curves of ANN-SGS models. Training and testing losses of (*a*) SL-106H, (*b*) SL-286H, (*c*) SL-106 + 286H and (*d*) S-106H. Coloured lines correspond to the training loss of each model, and black dashed-dot lines correspond to the testing loss of each model. The iteration in the horizontal axes represents the mini-batch iteration.

Model	S-106H	SL-106H	SL-286H	SL-106 + 286H
Inputs	$\{\bar{S}_{ij}\}$	$\{\bar{S}_{ij}, L_{ij}\}$	$\{\bar{S}_{ij}, L_{ij}\}$	$\{\bar{S}_{ij}, L_{ij}\}$
Outputs	τ_{ij}	τ_{ij}	τ_{ij}	τ_{ij}
Re_λ of training data	106	106	286	106, 286

Table 2. Input variables and Reynolds numbers of training datasets for different ANN-SGS models.

for testing (80 % of the snapshots for training and 20 % for testing). Figure 3 shows the learning curve of the ANN-SGS models. The training loss and the testing loss show similar values and converge to a stationary value, indicating that all ANN-SGS models are trained without overfitting.

The performance of an ANN is highly affected by the normalisation of the input and output variables (Sola & Sevilla 1997). In the present study, the input and the output tensors are normalised as $\bar{S}^*_{ij} = \bar{S}_{ij}/\langle|\bar{S}|\rangle$, $L^*_{ij} = L_{ij}/\langle|L|\rangle$ and $\tau^*_{ij} = \tau_{ij}/\langle|\tau|\rangle$, where $\langle\cdot\rangle$ and $|\cdot|$ denote a volume average and an L_2 norm of the tensor, respectively. However, since the denominator $\langle|\tau|\rangle$ is unknown in actual LES, the normalisation factor for the SGS stress should be estimated. A detailed discussion regarding the normalisation factor for the SGS stress, particularly in the context of generalization to untrained conditions, is presented in § 3.2.

3. Results and discussion

In § 3.1 the performance of S-106H is compared with that of DSM from *a priori* and *a posteriori* tests of forced isotropic turbulence at $Re_\lambda = 106$. Based on the above results, S-106H is improved by providing an additional input L_{ij} (SL-106H). Accordingly, S-106H and SL-106H are compared in terms of the correlation coefficients, the p.d.f. of the SGS dissipation, the p.d.f. of the SGS stress and the energy spectrum. In § 3.2 special attention is given to the normalisation of the input and output tensors for the generalization of ANN-SGS models. Consequently, the generalizability of ANN-SGS models to transient flow is investigated in LES of decaying isotropic turbulence at various untrained conditions (i.e. initial Reynolds numbers and grid resolution). In §§ 3.3 and 3.4, the performance and the computational cost of the developed ANN-SGS models are compared with those of conventional algebraic dynamic mixed models. Finally, the application of the developed models to LES of turbulent channel flow is presented in §§ 3.5–3.7.

3.1. *Effects of input variables: a priori and a posteriori tests*

Before conducting an actual LES, the effects of input variables on ANN-SGS models are investigated in an *a priori* test of forced homogeneous isotropic turbulence at $Re_\lambda = 106$. Although consistent predictive capability in the *a priori* and *a posteriori* tests is not always guaranteed (Park, Lee & Choi 2005; Park & Choi 2021), *a priori* tests are still considered to be a useful step for evaluating SGS models (Piomelli, Moin & Ferziger 1988; Salvetti & Banerjee 1995). It is also worth noting that the performance of ANN-SGS models are actually assessed in *a posteriori* tests in the present study. While the use of $\bar{S}_{ij}$ is expected to be preferable for homogeneous isotropic turbulence in terms of the accuracy and stability (Park & Choi 2021), it is of interest to investigate how differently the predicted SGS stress aligns with respect to $\bar{S}_{ij}$. To examine the alignment, the correlation coefficients between $\bar{S}_{ij}$ and the predicted SGS stress (τ_{ij}^{ANN}) are calculated and listed in table 3. The correlation coefficient between the components of arbitrary second-order tensors α_{ij} and β_{ij} is defined as

$$Corr(\alpha_{ij}, \beta_{ij}) = \frac{\langle \alpha_{ij}\beta_{ij} \rangle}{\langle \alpha_{ij}^2 \rangle^{1/2} \langle \beta_{ij}^2 \rangle^{1/2}}, \tag{3.1}$$

where $\langle \cdot \rangle$ denotes the ensemble averaging. As shown in table 3, S-106H has much higher correlation coefficients between $\bar{S}_{ij}$ and τ_{ij}^{ANN} than fDNS with the value exceeding -0.8, which indicates that the predicted SGS stress is aligned closer to the strain-rate tensor rather than the true SGS stress.

Additionally, the p.d.f. of the SGS dissipation ε_{SGS} $(= -\tau_{ij}\bar{S}_{ij})$ predicted by S-106H is shown in figure 4(*a*). Negative SGS dissipation corresponds to the backscatter, which is the kinetic energy transfer from the subgrid scale to the resolved scale. Interestingly, S-106H shows a similar characteristic to that of the eddy-viscosity models that are not capable of predicting backscatter. It can be considered that an ANN-SGS model that uses the resolved strain-rate tensor alone as the input only rescales the given input $\bar{S}_{ij}$ to predict the SGS stress while maintaining its alignment.

Based on this observation, the performance of S-106H in actual LES is compared with that of DSM by conducting *a posteriori* tests of forced isotropic turbulence at $Re_\lambda = 106$. The energy spectrum and p.d.f.s of the SGS dissipation and the SGS stress from S-106H are compared with those from DSM and fDNS. The SGS stress of DSM

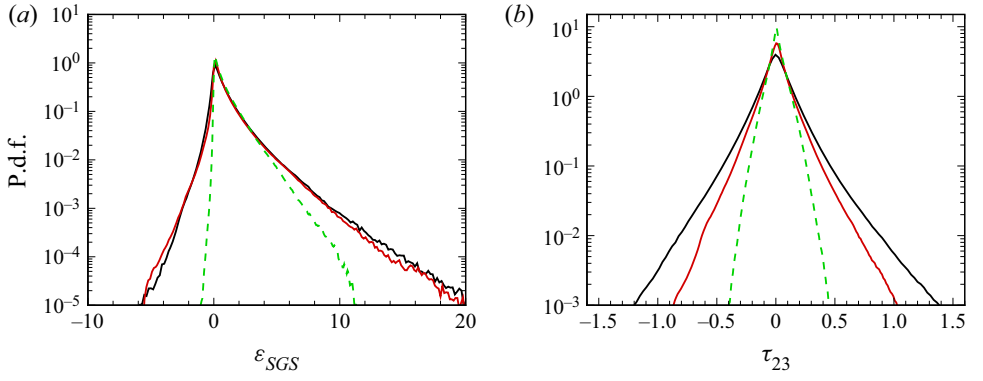

Figure 4. Results from an *a priori* test of forced homogeneous isotropic turbulence at $Re_\lambda = 106$. (*a*) P.d.f. of the SGS dissipation ε_{SGS} ($= -\tau_{ij}\bar{S}_{ij}$); (*b*) p.d.f. of τ_{23}. Here —— (thick black solid line), fDNS; —— (thick red solid line), SL-106H; – – - (thick green dashed line), S-106H.

(Germano *et al.* 1991; Lilly 1992) is given as

$$\tau_{ij} - \tfrac{1}{3}\delta_{ij}\tau_{kk} = -2C\bar{\Delta}^2|\bar{S}|\bar{S}_{ij}, \tag{3.2}$$

where $|\bar{S}| = \sqrt{2\bar{S}_{ij}\bar{S}_{ij}}$, $\bar{S}_{ij} = \frac{1}{2}(\partial\bar{u}_i/\partial x_j + \partial\bar{u}_j/\partial x_i)$, $C = \langle L_{ij}M_{ij}\rangle/\langle M_{ij}M_{ij}\rangle$, $L_{ij} = \widehat{\bar{u}_i\bar{u}_j} - \hat{\bar{u}}_i\hat{\bar{u}}_j$, $M_{ij} = -2\hat{\Delta}^2|\hat{\bar{S}}|\hat{\bar{S}}_{ij} + 2\bar{\Delta}^2\widehat{|\bar{S}|\bar{S}_{ij}}$, $\bar{\Delta}$ and $\hat{\Delta}(=\sqrt{5}\bar{\Delta})$ are the grid-filter and test-filter scales, respectively. $\overline{(\cdot)}$ denotes the grid-level filter at $\bar{\Delta}$ scale, $\widehat{(\cdot)}$ denotes the test filter at $\hat{\Delta}$ scale and $\langle\cdot\rangle$ denotes averaging over homogeneous directions (volume averaging for homogeneous isotropic turbulence). The LES are performed using a pseudospectral code HIT3D (Chumakov 2007, 2008) with the dealiasing method of the 2/3 rule. The second-order Adams–Bashforth scheme is used for time integration and the time step size is set so that the Courant–Friedrichs–Lewy number of LES is the same as that of DNS (Wang *et al.* 2018). The present ANN-SGS models predict the SGS stress tensor at each local grid point using resolved flow variables at the corresponding grid point as inputs. Large-eddy simulations with ANN-SGS models are performed without any *ad hoc* stabilisation procedures.

Figure 5 shows energy spectra from LES of forced isotropic turbulence at $Re_\lambda = 106$ with a grid resolution of 48^3, which is the same as that of the training data. The DSM is found to overestimate the energy spectrum in the range of $k \leqslant 5$. Interestingly, S-106H shows nearly identical performance to that of DSM in predicting the energy spectrum. In addition, from the p.d.f. of the SGS dissipation shown in figure 6(*a*), S-106H and DSM have the same characteristic that they are not capable of predicting backscatter. Note that the p.d.f. of the SGS stress (τ_{23}) predicted by S-106H is almost identical to that of DSM as both p.d.f.s are narrower than that of fDNS (figure 6*b*). This indicates that S-106H produces the SGS stress similar to that of DSM.

From the above observation, it can be concluded that the ANN-SGS model with $\bar{S}_{ij}$ as an input predicts the SGS stress that is closely aligned with the given input tensor, and performs similarly to DSM. Consequently, it is expected that S-106H can be improved by the similar concept employed in dynamic mixed models (Liu *et al.* 1994; Anderson & Meneveau 1999). It is reported that a linear combination of the eddy-viscosity model with the resolved stress $L_{ij}(= \widehat{\bar{u}_i\bar{u}_j} - \hat{\bar{u}}_i\hat{\bar{u}}_j)$ improves the accuracy of the predicted SGS stress with better alignment to the true SGS stress.

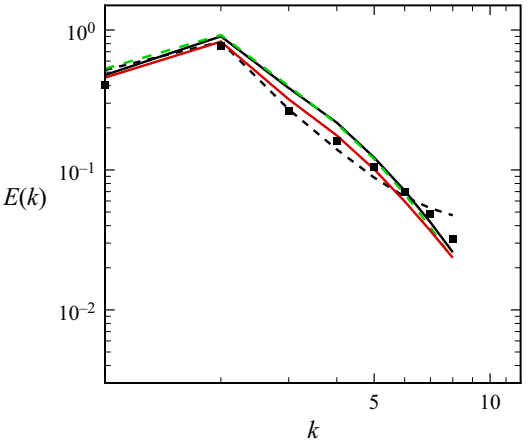

Figure 5. Energy spectra from fDNS and LES of forced homogeneous isotropic turbulence at $Re_\lambda = 106$ with grid resolution of 48^3. Here ■, fDNS; —— (thick black solid line), DSM; – – – (thick black dashed line), no-SGS; —— (thick red solid line), SL-106H; – – - (thick green dashed line), S-106H.

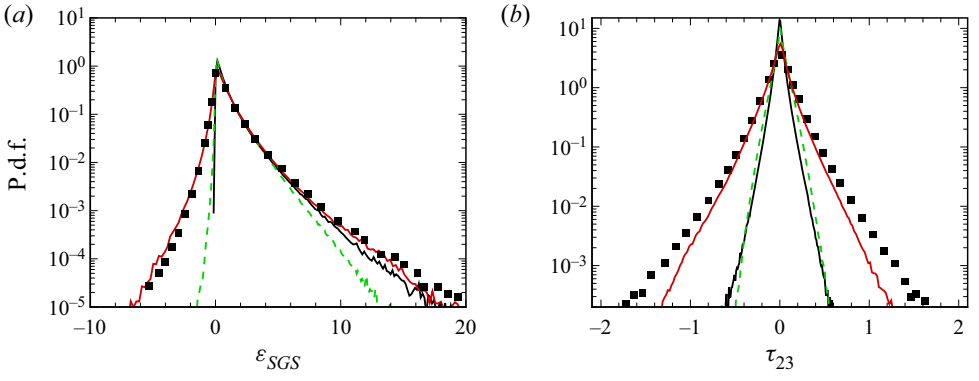

Figure 6. Results from an *a posteriori* test of forced homogeneous isotropic turbulence at $Re_\lambda = 106$ with grid resolution of 48^3. (*a*) P.d.f. of the SGS dissipation ε_{SGS} $(= -\tau_{ij}\bar{S}_{ij})$; (*b*) p.d.f. of τ_{23}. Here ■, fDNS; —— (thick black solid line), DSM; —— (thick red solid line), SL-106H; – – - (thick green dashed line), S-106H.

Similarly to the algebraic dynamic mixed models, it is expected that an ANN-SGS model can achieve closer alignment to the true SGS stress and more accurate prediction of the magnitude of the SGS stress if the resolved stress tensor L_{ij} is considered as an input in addition to the strain-rate tensor $\bar{S}_{ij}$ (i.e. ANN-SGS mixed model). A total of 12 components, six from $\bar{S}_{ij}$ and six from the resolved stress L_{ij}, are simultaneously provided as inputs for the ANN-SGS mixed model. To investigate the effect of the additional input variable, results of S-106H and SL-106H are compared in *a priori* and *a posteriori* tests of forced homogeneous isotropic turbulence at $Re_\lambda = 106$. Results of SL-106H are also compared with those of the algebraic dynamic mixed models in § 3.3.

The performance of SL-106H is compared with that of S-106H in an *a priori* test. The correlation coefficients between the true and the predicted SGS stress tensors are calculated following the definition of (3.1) and shown in table 4. The correlation coefficients of SL-106H are significantly improved compared with those of S-106H, which indicates that SL-106H reconstructs the instantaneous SGS stress closer to the true

	$Corr(\bar{S}_{12}, \tau_{12})$	$Corr(\bar{S}_{13}, \tau_{13})$	$Corr(\bar{S}_{23}, \tau_{23})$
fDNS	−0.2806	−0.2849	−0.2825
S-106H	−0.8217	−0.8370	−0.8172
SL-106H	−0.3992	−0.3993	−0.3806

Table 3. Correlation coefficients ($Corr(\bar{S}_{ij}, \tau_{ij})$) between $\bar{S}_{ij}$ and the predicted SGS stress by ANN-SGS models from an *a priori* test of forced homogeneous isotropic turbulence at $Re_\lambda = 106$.

	τ_{11}	τ_{22}	τ_{33}	τ_{12}	τ_{13}	τ_{23}
S-106H	0.3581	0.3538	0.3509	0.3692	0.3663	0.3661
SL-106H	0.7102	0.7176	0.7162	0.7057	0.7040	0.7172

Table 4. Correlation coefficients ($Corr(\tau_{ij}^{fDNS}, \tau_{ij}^{ANN})$) between the traceless parts of the true SGS stress (τ_{ij}^{fDNS}) and the predicted SGS stress by ANN-SGS models (τ_{ij}^{ANN}) from an *a priori* test of forced homogeneous isotropic turbulence at $Re_\lambda = 106$.

SGS stress. In table 3 the correlation coefficients between $\bar{S}_{ij}$ and the predicted SGS stress τ_{ij} ($Corr(\bar{S}_{ij}, \tau_{ij})$) from SL-106H are found to be closer to those of fDNS than those from S-106H, indicating that SL-106H is capable of aligning the principal axes of the predicted SGS stress closer to the true SGS stress. In addition, SL-106H provides excellent prediction of the p.d.f. of the SGS dissipation (figure 4*a*), which almost overlaps with that of fDNS. At the same time, SL-106H predicts the p.d.f. of the SGS stress (τ_{23}) closer to that of fDNS, whereas S-106H predicts a narrower p.d.f. as shown in figure 4(*b*).

An *a posteriori* test of forced isotropic turbulence at $Re_\lambda = 106$ is also conducted using SL-106H. As shown in figure 5, SL-106H predicts the energy spectrum closer to that of fDNS than S-106H and DSM in the range of $k \leqslant 5$. Furthermore, SL-106H noticeably better predicts the p.d.f. of the SGS dissipation than S-106H (figure 6*a*). It is worth noting that SL-106H is capable of accurately predicting the backscatter even in the *a posteriori* test; consequently, LES becomes stable without any *ad hoc* procedures, which is a clear advantage over the algebraic dynamic SGS models. Model SL-106H is found to predict the p.d.f. of the SGS stress (τ_{23}) more accurately, as shown in figure 6(*b*).

Figure 7 shows p.d.f.s of the resolved strain-rate tensor from fDNS and LES. Both SL-106H and DSM accurately predict the p.d.f. of $\bar{S}_{11}$, while S-106H shows slight overestimation from the right tail of the p.d.f. On the other hand, no significant differences in the p.d.f.s of $\bar{S}_{23}$ from DSM, SL-106H and S-106H are observed.

Contours of the SGS dissipation (ε_{SGS}) from fDNS and LES are shown in figure 8 for qualitative comparison. Snapshots are sampled after 21.5 large-eddy turnover times and at the centre of the domain in the z direction. The SGS dissipation of SL-106H shows a relatively closer spatial distribution to that of fDNS than those of DSM and S-106H, since the backscatter (i.e. negative regions in the contours) is observed in the contours of SL-106H and fDNS, while DSM and S-106H are not capable of predicting the backscatter. This result is consistent with the p.d.f.s in figure 6(*a*).

The second-order longitudinal velocity structure functions from fDNS and LES of forced homogeneous isotropic turbulence at $Re_\lambda = 106$ with a grid resolution of 24^3, 48^3

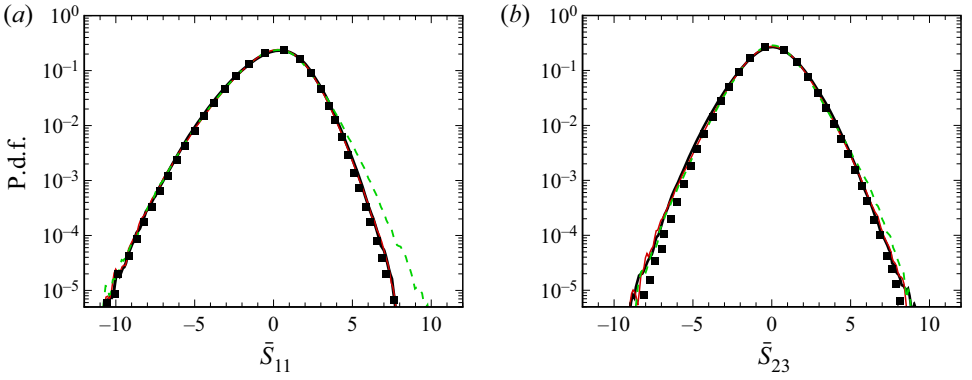

Figure 7. The p.d.f.s of the resolved strain-rate tensor (*a*) $\bar{S}_{11}$ and (*b*) $\bar{S}_{23}$ from an *a posteriori* test of forced homogeneous isotropic turbulence at $Re_\lambda = 106$ with grid resolution of 48^3. Here ■, fDNS; —— (thick black solid line), DSM; —— (thick red solid line), SL-106H; – – - (thick green dashed line), S-106H.

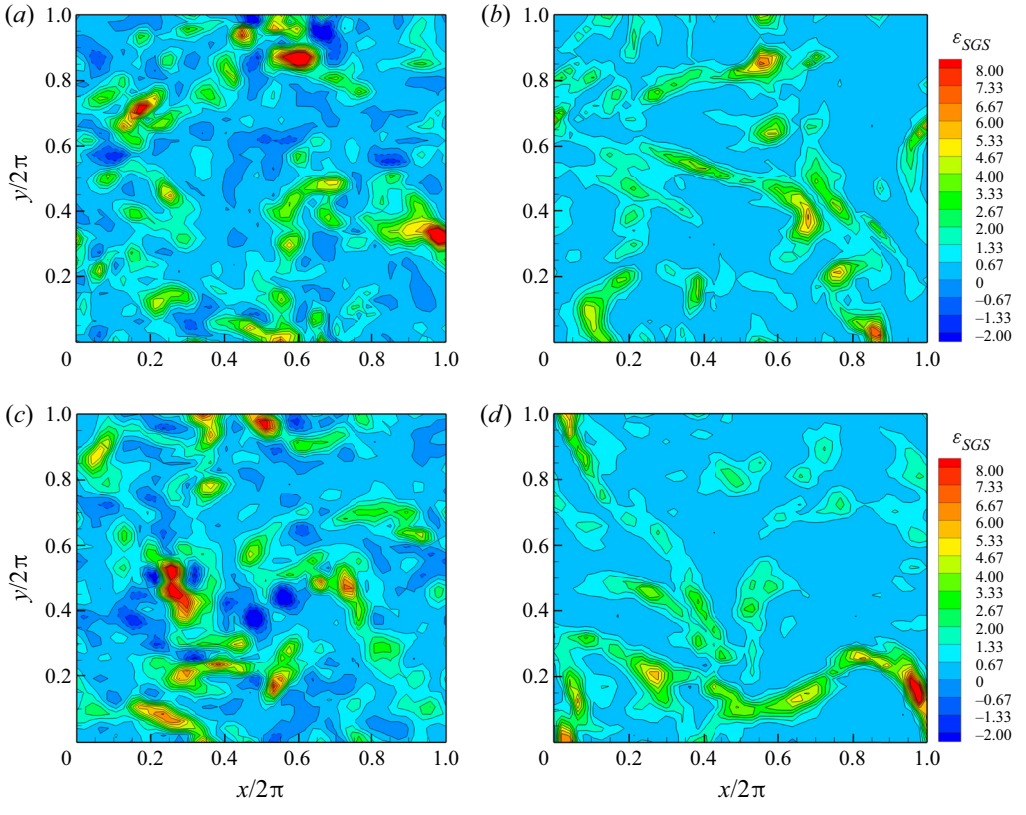

Figure 8. Contours of the SGS dissipation ε_{SGS} ($= -\tau_{ij}\bar{S}_{ij}$) from an *a posteriori* test of forced homogeneous isotropic turbulence at $Re_\lambda = 106$ with grid resolution of 48^3. Results are shown for (*a*) fDNS, (*b*) DSM, (*c*) SL-106H, (*d*) S-106H.

and 96^3 are compared in figure 9. Note that SL-106H and S-106H are trained only for fDNS data with the filter size for 48^3 resolution. Generalization to untrained resolution will be discussed in § 3.2. The second-order longitudinal velocity structure function $S_2^L(r)$

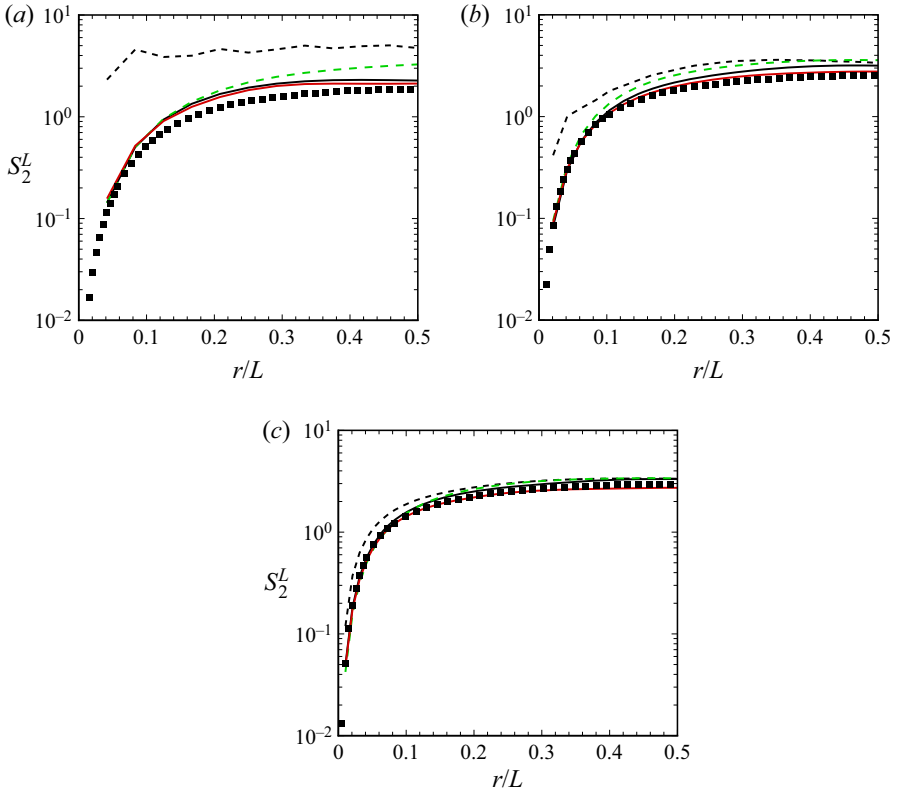

Figure 9. The second-order longitudinal velocity structure functions $S_2^L(r)$ from fDNS and LES of forced homogeneous isotropic turbulence at $Re_\lambda = 106$ with a grid resolution of (*a*) 24^3, (*b*) 48^3 and (*c*) 96^3. The domain size 2π is denoted by L. Here ■, fDNS; —— (thick black solid line), DSM; – – - (thick black dashed line), no-SGS; —— (thick red solid line), SL-106H; – – - (thick green dashed line), S-106H.

is defined as

$$S_2^L(r) \equiv \left\langle (\Delta u^L)^2 \right\rangle, \quad \Delta u^L \equiv \left[\bar{\boldsymbol{u}}(\boldsymbol{x}+\boldsymbol{r}) - \bar{\boldsymbol{u}}(\boldsymbol{x}) \right] \cdot \hat{\boldsymbol{r}}, \tag{3.3a,b}$$

where $\bar{\boldsymbol{u}}(\boldsymbol{x})$ is the filtered velocity vector at $\boldsymbol{x}$, $\hat{\boldsymbol{r}} = \boldsymbol{r}/|\boldsymbol{r}|$ is a unit vector in the direction of the separation $\boldsymbol{r}$. No distinctive differences in the structure functions at small separations are observed except for those of the no-SGS case that shows notable errors at small separations, indicating an inaccurate prediction of small-scale fluctuations. For all tested grid resolutions, SL-106H shows a more accurate prediction of the structure functions at large separations than DSM and S-106H.

Results of *a priori* and *a posteriori* tests using SL-106H clearly indicate that considering the resolved stress L_{ij} as an input in addition to $\bar{S}_{ij}$ improves the performance of the ANN-SGS model. Unlike the SGS stress predicted by S-106H that is closely aligned with the given input $\bar{S}_{ij}$, the SGS stress predicted by SL-106H is closely aligned with the true SGS stress. Although the performance of S-106H is almost identical to that of DSM, both S-106H and SL-106H have advantages over DSM as they are free from the requirement of a stabilisation process such as averaging over statistically homogeneous directions or clipping of the negative model coefficients.

3.2. *Generalization to untrained conditions: decaying homogeneous isotropic turbulence*

In this section the application of ANN-SGS models trained with only forced homogeneous isotropic turbulence data to untrained decaying isotropic turbulence is discussed. For successful generalization to decaying isotropic turbulence, ANN-SGS models have to provide an accurate prediction of the SGS stress for various Reynolds numbers and grid resolution.

In this regard, normalisation of variables is important, as it plays a critical role for the consistent performance of an ANN under various conditions. As explained in § 2.4, the input and output tensors are normalised as $\bar{S}^*_{ij} = \bar{S}_{ij}/\langle|\bar{S}|\rangle$, $L^*_{ij} = L_{ij}/\langle|L|\rangle$ and $\tau^*_{ij} = \tau_{ij}/\langle|\tau|\rangle$, where the denominator $\langle|\tau|\rangle$ requires an approximation in actual LES. The input variables ($\bar{S}_{ij}$ and L_{ij}) are properly normalised by the magnitudes of the variables to have similar distributions for various conditions. However, normalising the SGS stress tensor to have similar distributions for various conditions is a challenging task because the approximation for $\langle|\tau|\rangle$ is not accurate enough. In other words, an inaccurate approximation of the normalisation factor of the output SGS stress results in a significantly different distribution of the normalised output for different conditions. In this situation, an ANN-based model could suffer from the prior probability shift issue, which occurs when the output variable distributions are different at training and test conditions (i.e. $P_{train}(y) \neq P_{test}(y)$, where $P(y)$ is a probability distribution of an output variable y) (Quiñonero-Candela *et al.* 2009; Moreno-Torres *et al.* 2012). Dataset shift, including the prior probability shift, is not desirable for ANNs as it can cause significant changes in their performance during testing with untrained data (Gawlikowski *et al.* 2021). Consequently, the performance of an ANN-SGS model trained at a specific Reynolds number and on a certain grid resolution could be different from that at other flow conditions.

Therefore, it is suggested that a normalisation factor, which enables the distributions of the normalised inputs and outputs to remain unchanged for various Reynolds numbers and grid resolution, should be selected to avoid such performance inconsistency of an ANN-SGS model during the generalization. The modified Leonard term $\mathcal{L}^m_{ij}$ ($= \overline{\bar{u}_i\bar{u}_j} - \bar{\bar{u}}_i\bar{\bar{u}}_j$), the resolved stress L_{ij} ($= \widehat{\bar{u}_i\bar{u}_j} - \hat{\bar{u}}_i\hat{\bar{u}}_j$) and the gradient model term τ^{grad}_{ij} ($= \frac{1}{12}\bar{\Delta}^2(\partial\bar{u}_i/\partial x_k)(\partial\bar{u}_j/\partial x_k)$) are considered to approximate the normalisation factor for the SGS stress. Among the three candidates, the term that has the most constant ratio to the true SGS stress $\langle|\tau|\rangle$ for various Reynolds numbers and grid resolution should be selected. Figure 10 shows ratios of $\langle|\tau^{grad}|\rangle$, $\langle|\mathcal{L}^m|\rangle$ and $\langle|L|\rangle$ to $\langle|\tau^{fDNS}|\rangle$, obtained at three different Reynolds numbers on a fixed grid resolution and three different grid resolutions at $Re_\lambda = 106$. The gradient model term $\langle|\tau^{grad}|\rangle$ shows the most constant ratio to the true SGS stress $\langle|\tau^{fDNS}|\rangle$ for various Reynolds numbers and grid resolution, compared with the other two terms. Therefore, in the present study, the averaged L_2 norm of the gradient model term is selected to normalise and rescale the output SGS stress tensor as $\tau^*_{ij} = \tau_{ij}/\langle|\tau^{grad}|\rangle$.

Figure 11 shows the p.d.f. of the SGS stress from fDNS of forced isotropic turbulence with and without normalisation. Distributions of the SGS stress without normalisation vary significantly depending on the Reynolds number and grid resolution, while the normalised SGS stress tensors show similar distributions for various Reynolds numbers and grid resolution, which enables an ANN-SGS model trained at a single condition to be successfully generalized to other conditions. In figure 12 effectiveness of the normalisation is verified in LES of forced homogeneous isotropic turbulence at $Re_\lambda = 106$ with a grid resolution of 24^3 and 96^3, which are coarser and finer by a factor of 2 than that

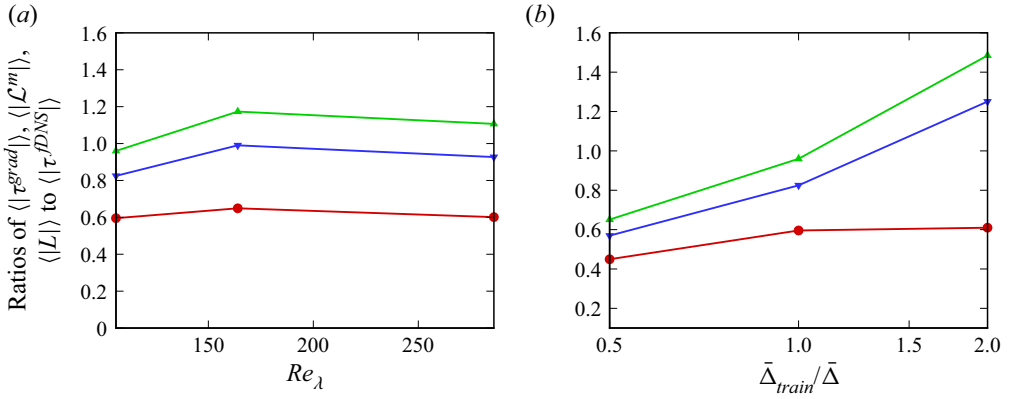

Figure 10. Ratios of $\langle|\tau^{grad}|\rangle$, $\langle|\mathcal{L}^m|\rangle$ and $\langle|L|\rangle$ to $\langle|\tau^{fDNS}|\rangle$ at (*a*) $Re_\lambda = 106$, 168 and 286 for $\bar{\Delta}_{train}/\bar{\Delta} = 1$, and for (*b*) $\bar{\Delta}_{train}/\bar{\Delta} = 1/2$, 1, 2 at $Re_\lambda = 106$. Here —— (thick red solid line), $\langle|\tau^{grad}|\rangle / \langle|\tau^{fDNS}|\rangle$; —— (thick blue solid line), $\langle|\mathcal{L}^m|\rangle / \langle|\tau^{fDNS}|\rangle$; —— (thick green solid line), $\langle|L|\rangle / \langle|\tau^{fDNS}|\rangle$.

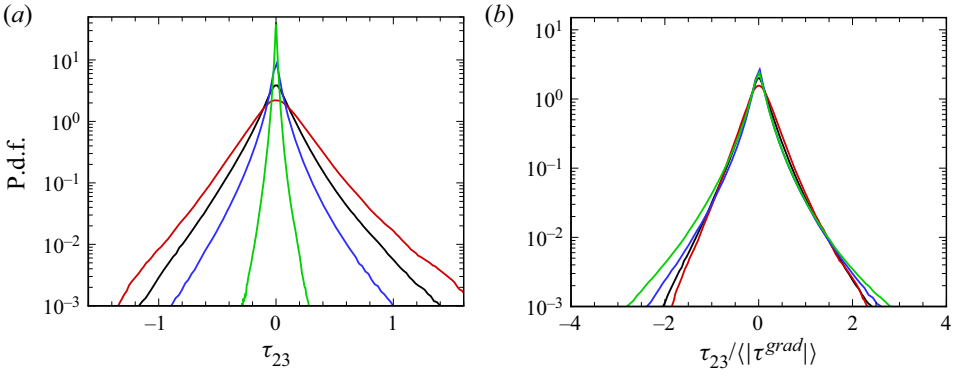

Figure 11. The p.d.f.s of the SGS stress τ_{23} from fDNS of forced isotropic turbulence with various Reynolds numbers and grid resolution. (*a*) The p.d.f.s of τ_{23} without normalisation; (*b*) the p.d.f.s of normalised τ_{23} with $\langle|\tau^{grad}|\rangle$. —— (thick black solid line), $Re_\lambda = 106$, $\bar{\Delta}_{train}/\bar{\Delta} = 1$; —— (thick red solid line), $Re_\lambda = 106$, $\bar{\Delta}_{train}/\bar{\Delta} = 1/2$; —— (thick blue solid line), $Re_\lambda = 106$, $\bar{\Delta}_{train}/\bar{\Delta} = 2$; —— (thick green solid line), $Re_\lambda = 286$, $\bar{\Delta}_{train}/\bar{\Delta} = 1$.

of the training data, respectively. As shown in figure 12(*a*), SL-106H, SL-286H and SL-106 + 286H predict the energy spectra more accurately than DSM and S-106H at all wavenumbers on a coarser resolution (24^3). On a finer resolution of 96^3, SL-106H, SL-286H and SL-106 + 286H predict the energy spectra more accurately than DSM and S-106H in the range of $k \leqslant 6$ (figure 12*b*). This indicates that a proper choice of the normalisation factor for the output SGS stress enables the present ANN-SGS mixed models to perform accurately on an untrained coarser and finer grid resolution.

Using $\langle|\tau^{grad}|\rangle$ as the normalisation factor, ANN-SGS models trained with only forced homogeneous isotropic turbulence data are applied to LES for decaying homogeneous isotropic turbulence to assess the generalizability to untrained transient flow. Table 5 shows the initial Reynolds numbers and grid resolution of test LES cases for decaying isotropic turbulence. The numerical methods are the same as those used for LES of forced isotropic turbulence. A fully converged instantaneous flow field of fDNS of forced homogeneous

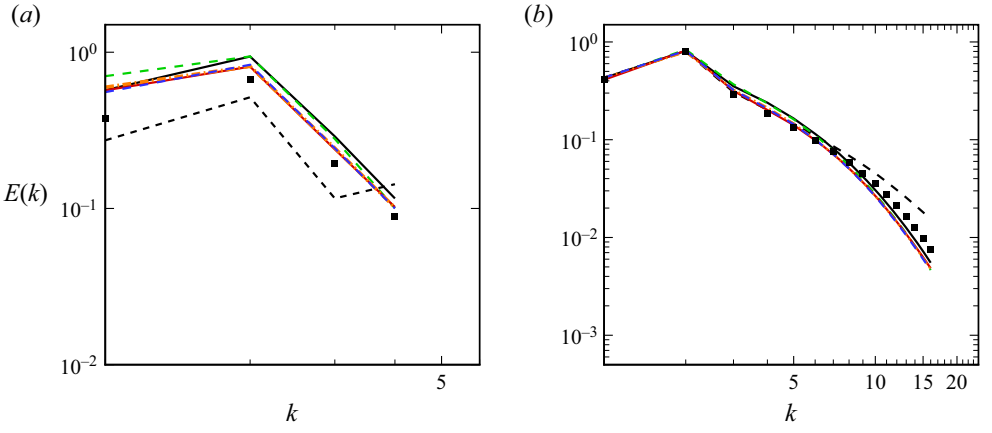

Figure 12. Energy spectra from fDNS and LES of forced homogeneous isotropic turbulence at $Re_\lambda = 106$ with a grid resolution of (*a*) 24^3 and (*b*) 96^3 (two-times coarser and finer resolution than that of training data, respectively). Here ■, fDNS; —— (thick black solid line), DSM; – – - (thick black dashed line), no-SGS; —— (thick red solid line), SL-106H; – – - (thick blue dashed line), SL-286H; – – – (thick yellow orange dashed-dot line), SL-106 + 286H; – – – (thick green dashed line), S-106H.

LES case	Initial Re_λ	N^3	SGS model
DHIT106	106	48^3	SL-106H SL-286H SL-106 + 286H S-106H DSM
DHIT106c	106	24^3	SL-106H SL-286H S-106H DSM
DHIT106f	106	96^3	SL-106H SL-286H S-106H DSM
DHIT286	286	128^3	SL-106H SL-286H S-106H DSM

Table 5. Test LES cases for decaying homogeneous isotropic turbulence with ANN-SGS models and DSM. Here N is the number of grid points in each direction. Effects of grid resolution and the initial Reynolds number on the performance of ANN-SGS models are considered.

isotropic turbulence is selected as the initial field of decaying homogeneous isotropic turbulence. The robustness of ANN-SGS models to a random-phase initial condition is assessed in Appendix D.

Figure 13 shows energy spectra from LES of decaying homogeneous isotropic turbulence at the initial Reynolds number Re_λ of 106 with a grid resolution of 48^3. Energy spectra are obtained at $t/T_{e,0} = 1.1$, 3.3 and 6.6, where time t is normalised by the initial eddy turnover time $T_{e,0}$. Energy spectra from S-106H and DSM are found to be

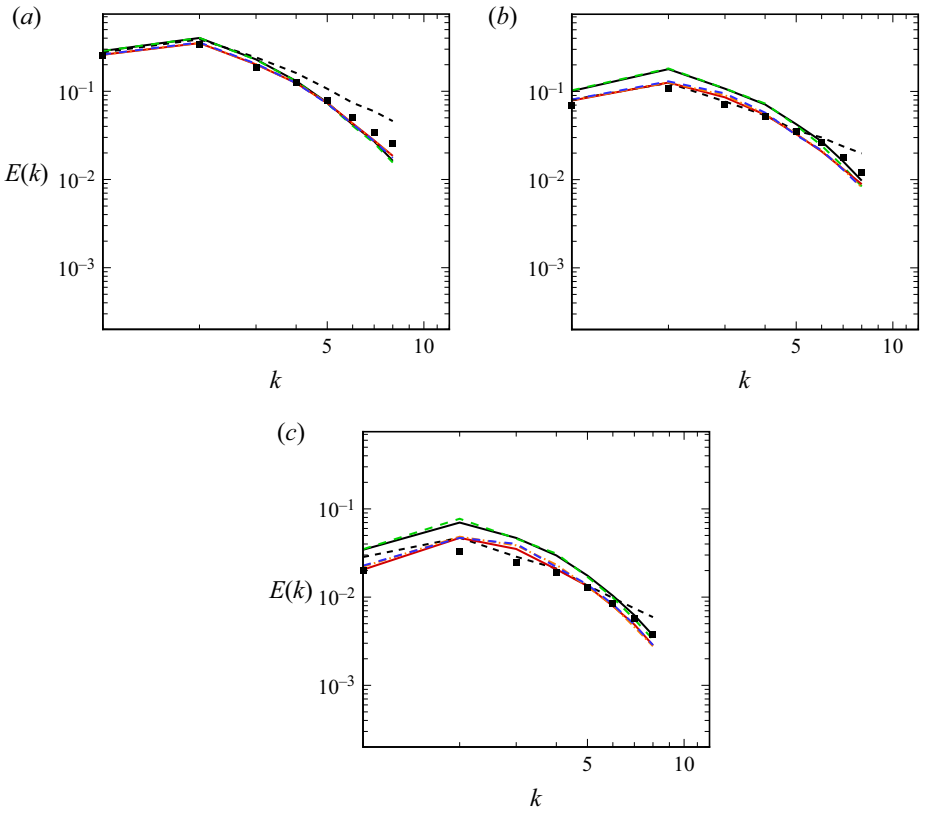

Figure 13. Energy spectra from fDNS and LES of decaying homogeneous isotropic turbulence at the initial Reynolds number Re_λ of 106 with a grid resolution of 48^3 (DHIT106 case). Results are shown for (*a*) $t/T_{e,0} = 1.1$; (*b*) $t/T_{e,0} = 3.3$; (*c*) $t/T_{e,0} = 6.6$. Here ■, fDNS; —— (thick black solid line), DSM; – – - (thick black dashed line), no-SGS; —— (thick red solid line), SL-106H; – – - (thick blue dashed line), SL-286H; – – - (thick yellow orange dashed-dot line), SL-106 + 286H; – – - (thick green dashed line), S-106H.

almost identical. This is consistent with the *a posteriori* test of forced isotropic turbulence where S-106H performs similar to DSM. Both S-106H and DSM overestimate the energy spectra in the range of $k < 5$, and errors increase as flow evolves. In contrast, energy spectra from SL-106H, SL-286H and SL-106 + 286H show better agreement with those of fDNS than DSM at all time steps.

Additionally, temporal evolution of the resolved kinetic energy and the mean SGS dissipation are investigated from the same simulations and presented in figure 14. The DSM and S-106H predict smaller SGS dissipation than that of fDNS, which leads to a slower decaying rate of the resolved kinetic energy. Compared with DSM, SL-106H, SL-286H and SL-106 + 286H significantly better predict temporal evolutions of the resolved kinetic energy and the SGS dissipation, which are in good agreement with those of fDNS.

Similarly to the results of forced isotropic turbulence, SL-106H, SL-286H and SL-106 + 286H perform significantly better than DSM for LES of decaying isotropic turbulence, which clearly indicates that the additional input variable L_{ij} is beneficial. In addition, SL-106H, SL-286H and SL-106 + 286H provide stable solutions without any *ad hoc* stabilisation procedures unlike DSM during the temporal evolution of the flow.

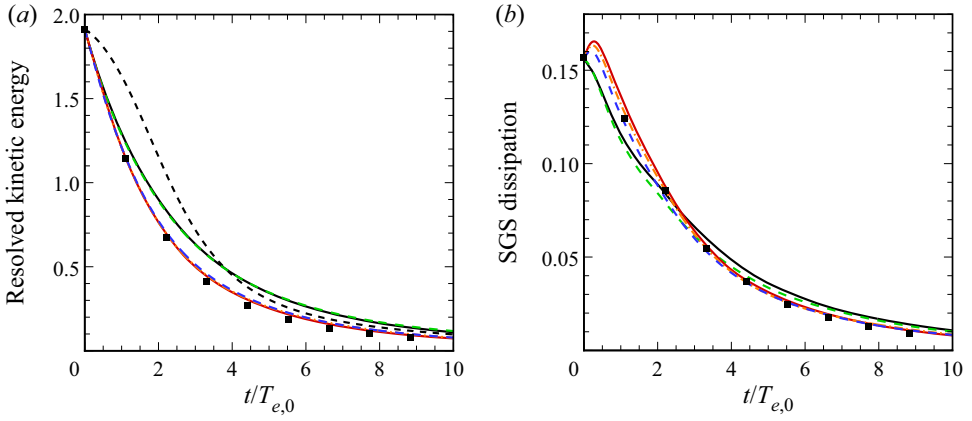

Figure 14. Results from fDNS and LES of decaying isotropic turbulence at the initial Reynolds number Re_λ of 106 with a grid resolution of 48^3 (DHIT106 case). Temporal evolution of (*a*) the resolved kinetic energy and (*b*) the mean SGS dissipation $\langle \varepsilon_{SGS} \rangle$ $(= \langle -\tau_{ij}\bar{S}_{ij} \rangle)$ are shown. Here ■, fDNS; —— (thick black solid line), DSM; – – – (thick black dashed line), no-SGS; —— (thick red solid line), SL-106H; – – – (thick blue dashed line), SL-286H; – – – (thick yellow orange dashed-dot line), SL-106 + 286H; – – – (thick green dashed line), S-106H.

Note that SL-106H, SL-286H and SL-106 + 286H show almost identical performance, although they are trained at different Reynolds numbers. This is because the present normalisation of the input and output variables enables the mapping of an ANN between the input resolved variables and the output SGS stress to remain unchanged for various flow conditions. Therefore, in the present study, training an ANN-SGS model at a single Reynolds number and on a single grid resolution is found to be sufficient for generalization to untrained flow conditions.

The performance of ANN-SGS models is further investigated through LES of decaying isotropic turbulence with different grid resolutions. Coarser (24^3) and finer (96^3) grid resolutions by a factor of 2 than that of the training dataset (48^3) are considered. These are challenging cases, as the magnitudes of the SGS stress and the resolved kinetic energy differ from those of the training data as the turbulence decays. Nevertheless, SL-106H and SL-286H perform consistently better than DSM.

The LES of decaying homogeneous isotropic turbulence at the initial Reynolds number Re_λ of 106 with a grid resolution of 24^3 is performed and results are shown in figure 15. The DSM and S-106H show similar performance; they overestimate the energy spectra at all wavenumbers, and the resolved kinetic energy decays slower than that of fDNS. On the other hand, SL-106H and SL-286H provide more accurate prediction of the energy spectra than that of DSM, especially with smaller errors at $k \leqslant 2$. Furthermore, SL-106H and SL-286H predict the temporal evolution of the resolved kinetic energy more accurately than DSM and S-106H.

Figure 16 shows results from LES of decaying homogeneous isotropic turbulence at the initial Reynolds number Re_λ of 106 with a grid resolution of 96^3. As the grid resolution becomes finer, the energy spectra and the temporal evolution of the resolved kinetic energy obtained by SL-106H and SL-286H become more accurate and almost overlap with those of fDNS. However, DSM and S-106H overestimate energy spectra in the range of $k \leqslant 6$ and predict slower decaying rates of the resolved kinetic energy.

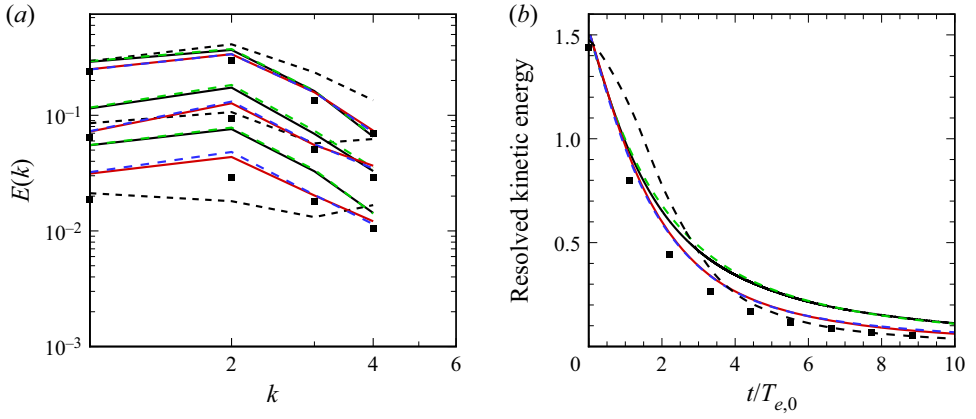

Figure 15. Results from fDNS and LES of decaying isotropic turbulence at the initial Reynolds number Re_λ of 106 with a grid resolution of 24^3 (DHIT106c case). (*a*) Energy spectra at $t/T_{e,0} = 1.1$, 3.3 and 6.6; (*b*) temporal evolution of the resolved kinetic energy. Here ■, fDNS; —— (thick black solid line), DSM; – – (thick black dashed line), no-SGS; —— (thick red dashed line), SL-106H; – – – (thick blue dashed line), SL-286H; – – – (thick green dashed line), S-106H.

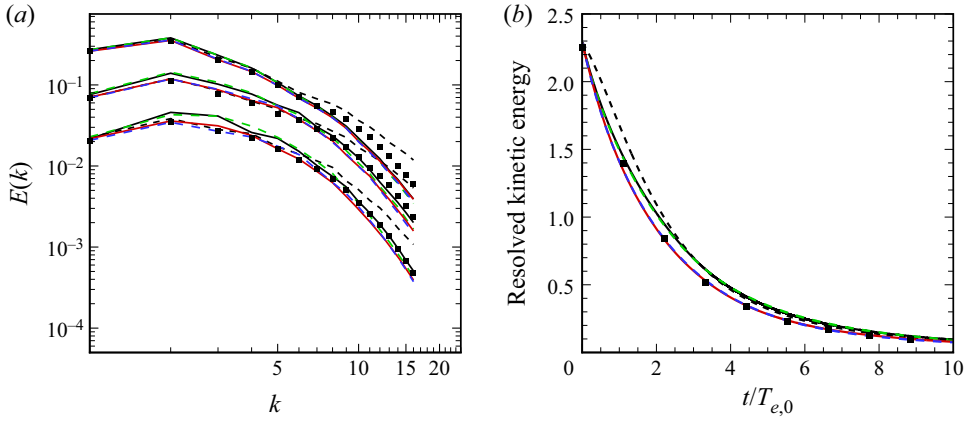

Figure 16. Results from fDNS and LES of decaying isotropic turbulence at the initial Reynolds number Re_λ of 106 with a grid resolution of 96^3 (DHIT106f case). (*a*) Energy spectra at $t/T_{e,0} = 1.1$, 3.3 and 6.6; (*b*) temporal evolution of the resolved kinetic energy. Here ■, fDNS; —— (thick black solid line), DSM; – – – (thick black dashed line), no-SGS; —— (thick red solid line), SL-106H; – – – (thick blue dashed line), SL-286H; – – – (thick green dashed line), S-106H.

The performance of ANN-SGS models is tested through LES at a higher initial Reynolds number Re_λ of 286. Figure 17 shows results from LES of decaying homogeneous isotropic turbulence with a grid resolution of 128^3, in which the cutoff wavenumber is located in the inertial range, same as in the training data. Notably, SL-106H is successfully generalized to the higher Reynolds number, and it predicts the energy spectra and the temporal evolution of the resolved kinetic energy more accurately than DSM. In figure 17(*a*), SL-106H and SL-286H accurately predict the energy spectra, which are in good agreement with those of fDNS. In contrast, DSM and S-106H slightly underestimate the energy at low wavenumbers ($k \leqslant 2$), while they overestimated the energy at $4 \leqslant k \leqslant 10$. In figure 17(*b*) temporal evolutions of the resolved kinetic energy of SL-106H and SL-286H are well

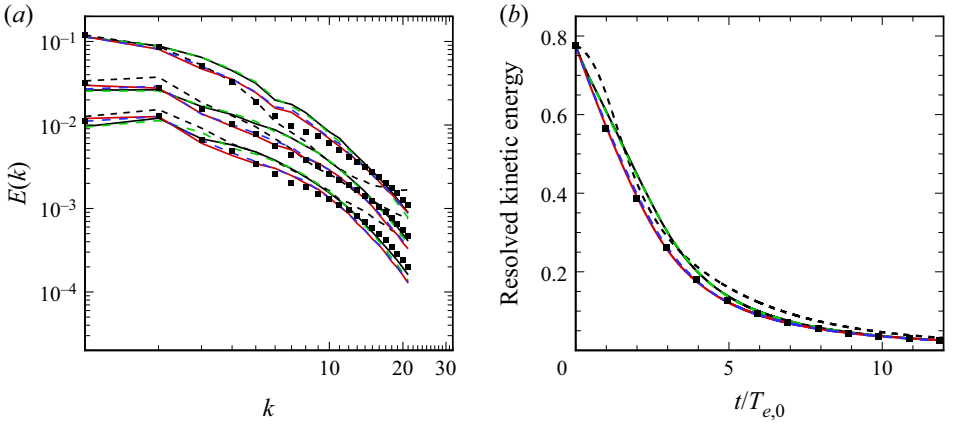

Figure 17. Results from fDNS and LES of decaying isotropic turbulence at the initial Reynolds number Re_λ of 286 with a grid resolution of 128^3 (DHIT286 case). (*a*) Energy spectra at $t/T_{e,0} = 2.0, 4.9, 7.9$; (*b*) temporal evolution of the resolved kinetic energy. Here ■, fDNS; —— (thick black solid line), DSM; – – – (thick black dashed line), no-SGS; —— (thick red solid line), SL-106H; – – – (thick blue dashed line), SL-286H; – – – (thick green dashed line), S-106H.

matched with those of fDNS at all time steps, whereas DSM and S-106H show slower decaying rates of the resolved kinetic energy until $t/T_{e,0} \approx 5$.

Despite the fact that the present ANN-SGS models are not trained for the transient characteristics of decaying isotropic turbulence, they can be successfully utilised for LES of transient decaying isotropic turbulence with various initial Reynolds numbers and grid resolution. This is again possible due to the selection of proper normalisation factors for the input and output variables such that the normalisation enables the mapping of an ANN between the input resolved variables and the output SGS stress to remain unchanged during the temporal decay of turbulence.

It is worth noting that, for wall-bounded turbulent flow, normalisation of the SGS stress using the gradient model term may not be appropriate since it is known to have an incorrect near-wall scaling (Liu *et al.* 1994). For turbulent channel flow and also for homogeneous isotropic turbulence, the magnitude of the resolved stress tensor is found to be the best alternative to the magnitude of the gradient model term. The advantage of using the resolved stress tensor for normalisation of the SGS stress over other normalisation options is discussed in Appendix E in detail.

3.3. *Comparison with algebraic dynamic mixed models*

In § 3.1 the predictive performance of SL-106H is found to meet the expectation that the use of both $\bar{S}_{ij}$ and L_{ij} as inputs could perform better than DSM due to better prediction of the SGS stress in terms of the magnitude and alignment to the true SGS stress. Consequently, it is of interest to investigate how well the ANN-SGS mixed model performs compared with the algebraic dynamic mixed models. Therefore, the performance of the developed ANN-SGS mixed model is compared with one-parameter (Zang *et al.* 1993; Vreman, Geurts & Kuerten 1994) and two-parameter (Anderson & Meneveau 1999) algebraic dynamic mixed models through LES of both forced and decaying isotropic turbulence.

The one-parameter dynamic mixed model that combines the eddy-viscosity model with the modified Leonard term ($\mathcal{L}_{ij}^m = \overline{\bar{u}_i \bar{u}_j} - \bar{\bar{u}}_i \bar{\bar{u}}_j$), which was formulated by

Zang *et al.* (1993) and later modified by Vreman *et al.* (1994), is denoted as DMM. The model coefficient of DMM is dynamically determined to close the SGS stress as

$$\tau_{ij} - \tfrac{1}{3}\delta_{ij}\tau_{kk} = -2C\bar{\Delta}^2|\bar{S}|\bar{S}_{ij} + \mathcal{L}^m_{ij} - \tfrac{1}{3}\delta_{ij}\mathcal{L}^m_{kk}, \tag{3.4}$$

where $C = \langle M_{ij}(L_{ij} - H_{ij})\rangle / \langle M_{ij}M_{ij}\rangle$, $M_{ij} = -2\hat{\bar{\Delta}}^2|\hat{\bar{S}}|\hat{\bar{S}}_{ij} + 2\bar{\Delta}^2\widehat{|\bar{S}|\bar{S}_{ij}}$, $L_{ij} = \widehat{\bar{u}_i\bar{u}_j} - \hat{\bar{u}}_i\hat{\bar{u}}_j$, $H_{ij} = \widehat{\hat{\bar{u}}_i\hat{\bar{u}}_j} - \hat{\bar{u}}\hat{\bar{u}} - (\widehat{\widehat{\bar{u}_i\bar{u}_j}} - \widehat{\bar{u}_i\bar{u}_j})$, $\mathcal{L}^m_{ij} = \overline{\bar{u}_i\bar{u}_j} - \bar{\bar{u}}_i\bar{\bar{u}}_j$.

Anderson & Meneveau (1999) formulated the dynamic two-parameter mixed model (DTM_{sim}), which combines the eddy-viscosity model with the resolved stress and calculates two model coefficients for eddy-viscosity and mixed terms using the dynamic procedure as

$$\tau_{ij} = -2C_1\bar{\Delta}^2|\bar{S}|\bar{S}_{ij} + C_2L_{ij}, \tag{3.5}$$

$$C_1 = \frac{\langle L_{ij}M_{ij}\rangle\langle N_{ij}N_{ij}\rangle - \langle L_{ij}N_{ij}\rangle\langle M_{ij}N_{ij}\rangle}{\langle M_{ij}M_{ij}\rangle\langle N_{ij}N_{ij}\rangle - \langle N_{ij}M_{ij}\rangle^2}, \tag{3.6}$$

$$C_2 = \frac{\langle L_{ij}N_{ij}\rangle\langle M_{ij}M_{ij}\rangle - \langle L_{ij}M_{ij}\rangle\langle M_{ij}N_{ij}\rangle}{\langle M_{ij}M_{ij}\rangle\langle N_{ij}N_{ij}\rangle - \langle N_{ij}M_{ij}\rangle^2}, \tag{3.7}$$

where $L_{ij} = \widehat{\bar{u}_i\bar{u}_j} - \hat{\bar{u}}_i\hat{\bar{u}}_j$, $M_{ij} = -2\hat{\bar{\Delta}}^2|\hat{\bar{S}}|\hat{\bar{S}}_{ij} + 2\bar{\Delta}^2\widehat{|\bar{S}|\bar{S}_{ij}}$, $N_{ij} = (\widetilde{\hat{\bar{u}}_i\hat{\bar{u}}_j} - \widetilde{\hat{\bar{u}}_i}\widetilde{\hat{\bar{u}}_j}) - (\widehat{\widehat{\bar{u}_i\bar{u}_j}} - \widehat{\hat{\bar{u}}_i\hat{\bar{u}}_j})$ and $\widetilde{(\cdot)}$ denotes the filtering at the $5\bar{\Delta}$ scale.

Anderson & Meneveau (1999) proposed another dynamic two-parameter mixed model (DTM_{nl}), which combines the eddy-viscosity model with the Clark model as

$$\tau_{ij} = -2C_1\bar{\Delta}^2|\bar{S}|\bar{S}_{ij} + C_2\bar{\Delta}^2\frac{\partial\bar{u}_i}{\partial x_k}\frac{\partial\bar{u}_j}{\partial x_k}, \tag{3.8}$$

where C_1 and C_2 are determined by (3.6) and (3.7), respectively, with $L_{ij} = \widehat{\bar{u}_i\bar{u}_j} - \hat{\bar{u}}_i\hat{\bar{u}}_j$, $M_{ij} = -2\hat{\bar{\Delta}}^2|\hat{\bar{S}}|\hat{\bar{S}}_{ij} + 2\bar{\Delta}^2\widehat{|\bar{S}|\bar{S}_{ij}}$, $N_{ij} = \hat{\bar{\Delta}}^2(\partial\hat{\bar{u}}_i/\partial x_k)(\partial\hat{\bar{u}}_j/\partial x_k) - \bar{\Delta}^2(\partial\bar{u}_i/\partial\widehat{x_k})(\partial\bar{u}_j/\partial x_k)$.

Table 6 shows correlation coefficients between the true and predicted SGS stresses by ANN-SGS models and algebraic SGS models from an *a priori* test of forced homogeneous isotropic turbulence at $Re_\lambda = 106$. Model DTM_{nl} shows the best correlation coefficients, while DSM shows the worst correlation coefficients among tested models with similar values to those reported by Xie *et al.* (2020*b*). Correlation coefficients from DTM_{sim} are better than those from DSM and worse than those from DMM (Salvetti & Banerjee 1995; Xie *et al.* 2020*b*). Model S-106H shows poor correlation coefficients similar to DSM, while SL-106H shows comparable correlation coefficients to those of DMM. The p.d.f.s of the SGS stress τ_{23} in figure 18(*b*) show a similar trend. The DSM shows the most inaccurate p.d.f. of τ_{23}, while DTM_{sim} and SL-106H show similarly improved prediction. The DMM and DTM_{nl} show more accurate p.d.f.s of the SGS stress compared with SL-106H. However, it is found from the following *a posteriori* test that higher correlation coefficients of the SGS stress in an *a priori* test do not guarantee more accurate LES results as also reported by Park *et al.* (2005) and Park & Choi (2021).

Table 7 shows correlation coefficients between $\bar{S}_{ij}$ and the predicted SGS stress τ^{model}_{ij}. Model S-106H shows high absolute magnitudes of $Corr(\bar{S}_{ij}, \tau_{ij})$ similar to those of DSM, as discussed in § 3.1. Both DMM and DTM_{nl} show closer values of $Corr(\bar{S}_{ij}, \tau_{ij})$ to those of fDNS compared with DSM. On the other hand, SL-106H predicts $Corr(\bar{S}_{ij}, \tau_{ij})$ most

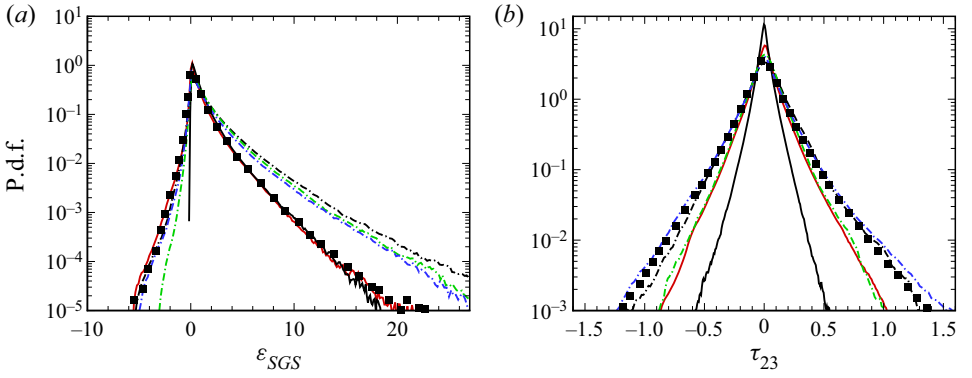

Figure 18. Results from an *a priori* test of forced homogeneous isotropic turbulence at $Re_\lambda = 106$. (*a*) The p.d.f. of the SGS dissipation ε_{SGS} ($= -\tau_{ij}\bar{S}_{ij}$); (*b*) p.d.f. of τ_{23}. Here ■, fDNS; —— (thick black solid line), DSM; – – – (thick black dashed-dot line), DMM; – – – (thick blue dashed-dot line), DTM_{nl}; – – – (thick green dashed-dot line), DTM_{sim}; —— (thick red solid line), SL-106H.

	τ_{11}	τ_{22}	τ_{33}	τ_{12}	τ_{13}	τ_{23}
S-106H	0.3581	0.3538	0.3509	0.3692	0.3663	0.3661
SL-106H	0.7102	0.7176	0.7162	0.7057	0.7040	0.7172
DSM	0.2890	0.2849	0.2718	0.2940	0.2989	0.3006
DMM	0.7088	0.7057	0.7079	0.7066	0.7066	0.7170
DTM_{nl}	0.9116	0.9109	0.9120	0.9111	0.9104	0.9135
DTM_{sim}	0.5239	0.5233	0.5181	0.5233	0.5254	0.5353

Table 6. Correlation coefficients ($Corr(\tau_{ij}^{fDNS}, \tau_{ij}^{model})$) between the traceless parts of the true SGS stress (τ_{ij}^{fDNS}) and the predicted SGS stress (τ_{ij}^{model}) from an *a priori* test of forced homogeneous isotropic turbulence at $Re_\lambda = 106$.

	$Corr(\bar{S}_{12}, \tau_{12})$	$Corr(\bar{S}_{13}, \tau_{13})$	$Corr(\bar{S}_{23}, \tau_{23})$
fDNS	−0.2806	−0.2849	−0.2825
S-106H	−0.8217	−0.8370	−0.8172
SL-106H	−0.3992	−0.3993	−0.3806
DSM	−0.9482	−0.9494	−0.9486
DMM	−0.5726	−0.5930	−0.5700
DTM_{nl}	−0.4291	−0.4365	−0.4301
DTM_{sim}	−0.7892	−0.8005	−0.7853

Table 7. Correlation coefficients ($Corr(\bar{S}_{ij}, \tau_{ij})$) between $\bar{S}_{ij}$ and the predicted SGS stress from an *a priori* test of forced homogeneous isotropic turbulence at $Re_\lambda = 106$.

closely to those of fDNS. In addition, SL-106H shows the most accurate prediction of the p.d.f. of the SGS dissipation, while the dynamic mixed models overestimate the forward scatter (figure 18*a*). The DSM is not capable of predicting the backscatter.

Figure 19 shows energy spectra from LES of forced isotropic turbulence at $Re_\lambda = 106$ with a grid resolution of 48^3, including those from the algebraic dynamic mixed models. Except for DSM, all models well predict the energy spectrum in the range of $k < 5$.

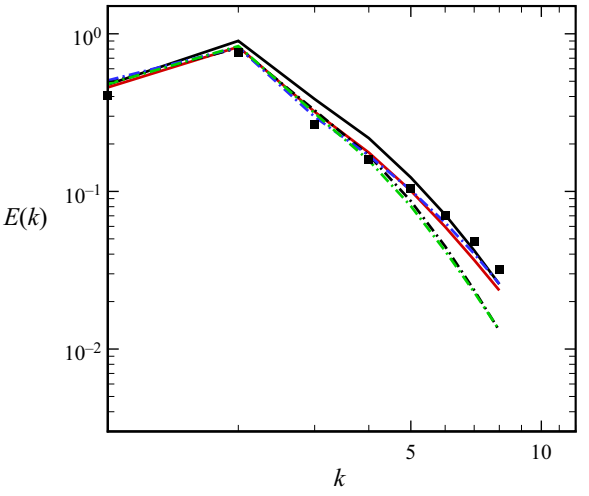

Figure 19. Energy spectra from fDNS and LES of forced homogeneous isotropic turbulence at $Re_\lambda = 106$ with a grid resolution of 48^3. Here ■, fDNS; —— (thick black solid line), DSM; – – – (thick black dashed-dot line), DMM; – – – (thick blue dashed-dot line), DTM_{nl}; – – – (thick green dashed-dot line), DTM_{sim}; —— (thick red solid line), SL-106H.

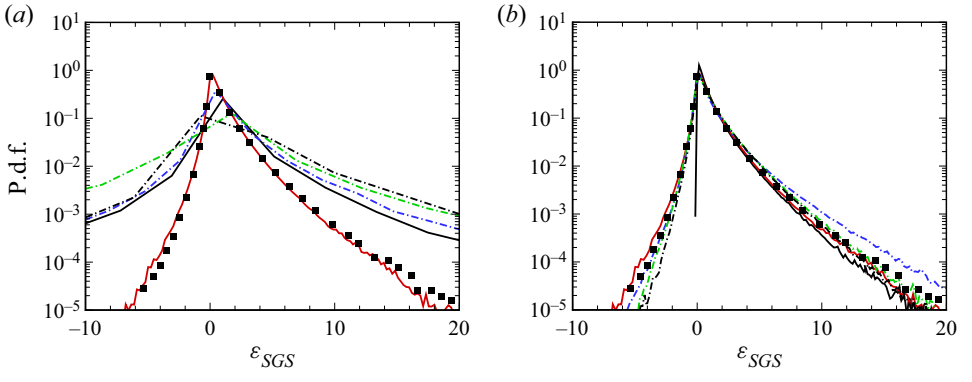

Figure 20. The p.d.f. of the SGS dissipation ε_{SGS} from LES of forced homogeneous isotropic turbulence at $Re_\lambda = 106$ with a grid resolution of 48^3. (*a*) Without *ad hoc* stabilisation; (*b*) with *ad hoc* stabilisation including averaging of the model coefficients in statistically homogeneous directions and clipping of the negative model coefficients. Here ■, fDNS; —— (thick black solid line), DSM; – – – (thick black dashed-dot line), DMM; – – – (thick blue dashed-dot line), DTM_{nl}; – – – (thick green dashed-dot line), DTM_{sim}; —— (thick red solid line), SL-106H.

However, energy spectra of DMM and DTM_{sim} deviate from that of fDNS in the range of $k \geqslant 5$, showing large errors near the cutoff wavenumber. Model DTM_{nl} accurately predicts the energy spectrum at all wavenumbers. Model SL-106H produces the energy spectrum nearly identical to that of DTM_{nl}. Both SL-106H and DTM_{sim} accurately predict the SGS dissipation, whereas DSM and DMM underestimate the backscatter and DTM_{nl} overestimates the forward scatter as shown in figure 20(*b*).

Note that the algebraic dynamic SGS models tested in the present study are stable only after applying *ad hoc* procedures (i.e. averaging of the model coefficients in statistically homogeneous directions and clipping of the negative model coefficients). A possible reason for this problem can be found from the p.d.f. of the SGS dissipation without *ad hoc*

procedures, as shown in figure 20(*a*). The dynamic Smagorinsky and algebraic dynamic mixed models significantly overestimate both backscatter and forward scatter when the *ad hoc* procedures are not applied. The excessive backscatter causes LES to diverge within tens of time steps. In contrast, LES with SL-106H is stable without any *ad hoc* procedures, since SL-106H accurately predicts the p.d.f. of the SGS dissipation, which is a notable advantage of the present ANN-SGS mixed model.

Additionally, LES of decaying isotropic turbulence at the initial Reynolds number Re_λ of 106 with a grid resolution of 48^3 is performed, and the results are shown in figures 21 and 22. Similarly to the results from LES of forced isotropic turbulence, DMM accurately predicts energy spectra at $k < 5$ but underpredicts the energy at $k \geqslant 5$. On the other hand, energy spectra of DTM_{nl} are accurate at $k \geqslant 5$ but the energy of large scale at $k \leqslant 2$ is slightly overestimated at $t/T_{e,0} = 3.3$ and 6.6. Model DTM_{sim} provides similar energy spectra, resolved kinetic energy and SGS dissipation to those of DSM after $t/T_{e,0} \geqslant 1.62$ since the model coefficient C_2 of (3.5) becomes negative and is clipped as zero after that time. The same issue in decaying isotropic turbulence is reported by Anderson & Meneveau (1999); the similarity coefficient of DTM_{sim} becomes negative when the grid resolution is too coarse so that the test-filter size exceeds the integral scale. Compared with the algebraic dynamic mixed models, SL-106H predicts most accurately the energy spectra at all time steps; especially, it shows the smallest error in the range of $k < 5$. In addition, SL-106H most accurately predicts the temporal evolution of the resolved kinetic energy and the mean SGS dissipation, as shown in figure 22. This indicates that the present ANN-SGS mixed model with input tensors of $\bar{S}_{ij}$ and L_{ij} is able to predict the decay of isotropic turbulence more accurately than the algebraic dynamic mixed models.

3.4. *Computational cost of ANN-SGS models*

Computational cost is an important factor of ANN-SGS models, as it is one of the main obstacles to the practical application of the models. Previous studies (Wang *et al.* 2018; Xie & Wang 2019; Xie *et al.* 2020*a*; Yuan *et al.* 2020; Park & Choi 2021) reported that ANN-SGS models are computationally more expansive than DSM, which can be considered a major disadvantage. Therefore, a parameter study of the present ANN-SGS mixed model with the number of neurons per hidden layer is conducted to find an optimal size of the ANN, as the computational time for forward propagation of an ANN depends on the size of the ANN.

Five different ANNs with 12 to 48 neurons and 2 to 4 hidden layers are considered. The ANN-SGS mixed models with the five different ANNs are trained with the fDNS dataset of forced isotropic turbulence at $Re_\lambda = 106$. Figure 23 shows results from LES of decaying homogeneous isotropic turbulence with a grid resolution of 48^3 using ANN-SGS mixed models with ANNs of five different sizes. It is found that 12 neurons and 2 hidden layers are sufficient, and additional neurons or hidden layers do not improve the performance of the ANN-SGS mixed model. However, the computational time to evaluate the SGS stress increases with the number of neurons as ratios of DSM : $12n$: $24n$: $48n = 1 : 0.71 : 0.89 : 1.42$, where n denotes the number of neurons per hidden layer. Therefore, in the present study an ANN with 12 neurons at each of the two hidden layers is selected.

The computational cost of the developed ANN-SGS mixed model is compared with those of the algebraic dynamic SGS models. For a fair comparison, the matrix operations of the ANN are implemented on the LES solver. The weight matrices and the bias vectors of the trained ANN are saved and transferred to the solver to perform a forward propagation of the ANN. All simulations are conducted using 16 CPU cores of Intel(R) Xeon(R)

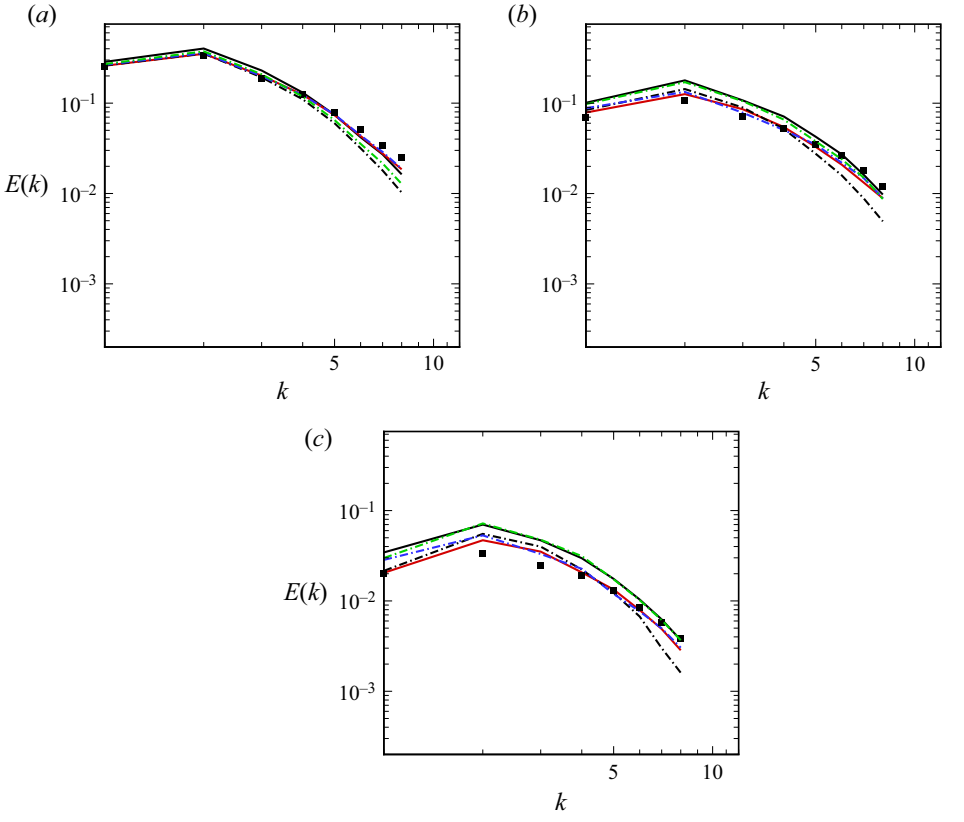

Figure 21. Energy spectra from fDNS and LES of decaying isotropic turbulence at the initial Reynolds number $Re_\lambda = 106$ with a grid resolution of 48^3 (DHIT106 case). Results are shown for (*a*) $t/T_{e,0} = 1.1$; (*b*) $t/T_{e,0} = 3.3$; (*c*) $t/T_{e,0} = 6.6$. Here ■, fDNS; —— (thick black solid line), DSM; – – – (thick black dashed-dot line), DMM; – – – (thick blue dashed-dot line), DTM_{nl}; – – – (thick green dashed-dot line), DTM_{sim}; —— (thick red solid line), SL-106H.

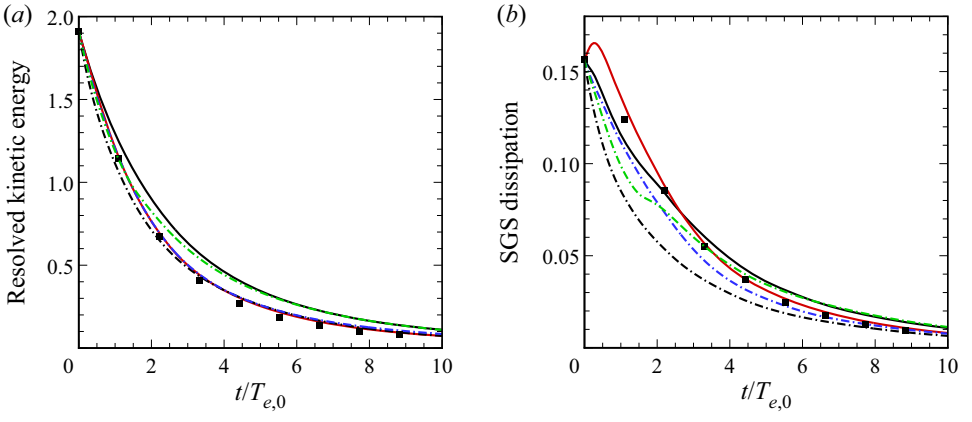

Figure 22. Results from fDNS and LES of decaying isotropic turbulence at the initial Reynolds number Re_λ of 106 with a grid resolution of 48^3 (DHIT106 case). Temporal evolution of (*a*) the resolved kinetic energy and (*b*) the mean SGS dissipation $\langle \varepsilon_{SGS} \rangle$ $(= \langle -\tau_{ij}\bar{S}_{ij} \rangle)$ are shown. Here ■, fDNS; —— (thick black solid line), DSM; – – – (thick black dashed-dot line), DMM; – – – (thick blue dashed-dot line), DTM_{nl}; – – – (thick green dashed-dot line), DTM_{sim}; —— (thick red solid line), SL-106H.

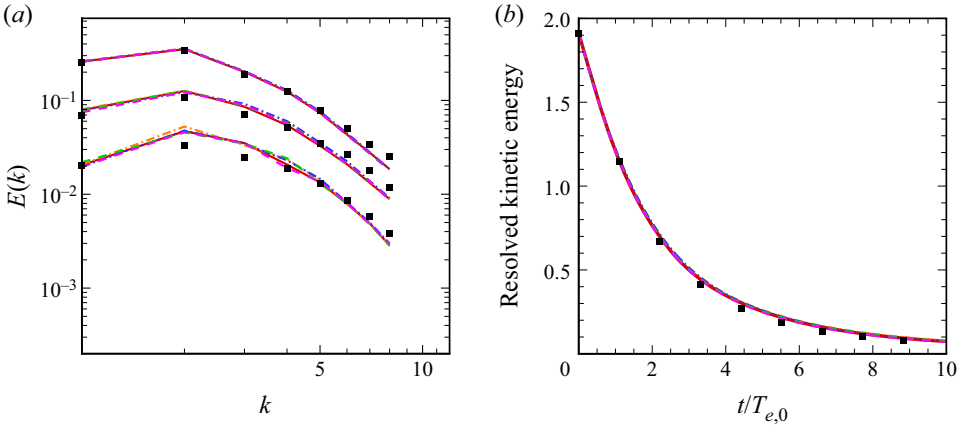

Figure 23. Results from fDNS and LES of decaying isotropic turbulence at the initial Reynolds number Re_λ of 106 with a grid resolution of 48^3. (*a*) Energy spectra at $t/T_{e,0} = 1.1$, 3.3 and 6.6; (*b*) temporal evolution of the resolved kinetic energy. Here ■, fDNS; ANN-SGS mixed model with —— (thick red solid line), 12 neurons and 2 hidden layers; – – – (thick yellow orange dashed-dot line), 24 neurons and 2 hidden layers; – – – (thick blue dashed-dot line), 48 neurons and 2 hidden layers; – – - (thick green dashed line), 12 neurons and 3 hidden layers; – – - (thick magenta dashed line), 12 neurons and 4 hidden layers.

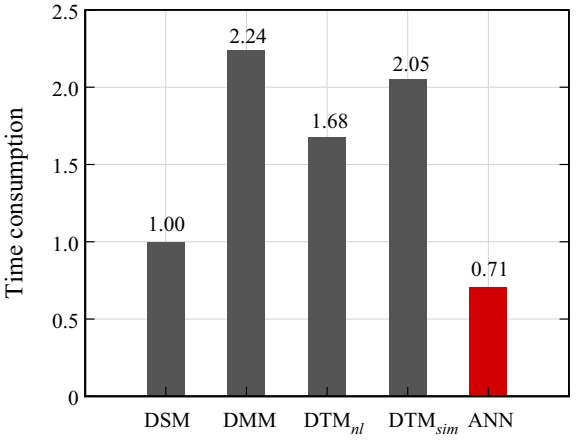

Figure 24. Ratio of computational time of tested SGS models for evaluating the SGS stress. Computational time is normalised to that of DSM.

E5-2650 v2, and the time consumption for evaluating the SGS stress tensors during the same 100 time steps are compared. Figure 24 shows ratios of the computational time of the tested SGS models for evaluating the SGS stress. The algebraic dynamic mixed models require 1.6 to 2.2 times greater computational time than DSM to calculate the SGS stress. It is noteworthy that the developed ANN-SGS mixed model is computationally cheaper than the algebraic dynamic mixed models and even than DSM.

3.5. *Training and testing for turbulent channel flow*

In this section application of the developed ANN-SGS mixed model to a wall-bounded flow is discussed. Turbulent channel flow at $Re_\tau = 180$ and 395 is considered. The predictive capabilities of the ANN-SGS mixed model that uses both $\bar{S}_{ij}$ and L_{ij} as

Re_τ	L_x	L_z	$N_x \times N_y \times N_z$	Δx^+	Δz^+	Δy^+_{min}	Δy^+_c
180	$4\pi\delta$	$\frac{4}{3}\pi\delta$	$192 \times 192 \times 192$	11.8	3.9	0.1	4.6
395	$2\pi\delta$	$\pi\delta$	$192 \times 192 \times 192$	13.0	6.5	0.2	10.0

Table 8. Parameters for DNS of turbulent channel flow. Here L_x and L_z are the streamwise and spanwise domain sizes, respectively; δ is the channel half-width, and N_x, N_y and N_z are numbers of grid points in the streamwise, wall-normal, and spanwise directions, respectively; Δx^+ and Δz^+ are the streamwise and the spanwise grid sizes in wall units, respectively; Δy^+_{min} and Δy^+_c are the wall-normal grid sizes at the wall and the centreline, respectively.

inputs and the ANN-SGS model with $\bar{S}_{ij}$ as the only input are investigated through *a posteriori* tests for a turbulent channel flow with various untrained Reynolds number and grid resolution. Additionally, it is further investigated whether the ANN-SGS mixed model trained with both channel flow and homogeneous isotropic turbulence at a certain condition is capable of providing accurate solutions for both types of flow at untrained conditions. Lastly, results from LES of turbulent channel flow with the ANN-SGS mixed model that is trained only with homogeneous isotropic turbulence are discussed.

Direct numerical simulations are performed with parameters summarized in table 8 to construct training datasets and reference solutions for LES. A fourth-order finite-difference code by Bose, Moin & You (2010) is utilised to conduct DNS and LES. The convection terms are discretized in a skew-symmetric form (Morinishi *et al.* 1998). A semi-implicit method is used for time marching. The viscous diffusion terms in the wall-normal direction are integrated implicitly with the Crank–Nicolson method, and the other terms are explicitly advanced with the third-order Runge–Kutta method (Morinishi *et al.* 1998; Bose *et al.* 2010; Kang & You 2021).

The fDNS dataset of a turbulent channel flow at $Re_\tau = 180$ is constructed by applying the grid and test filters with $\bar{\Delta} = 4\Delta_{DNS}$ and $\hat{\bar{\Delta}} = 8\Delta_{DNS}$ to instantaneous DNS fields, where Δ_{DNS} is the grid spacing of DNS. The filter width $\bar{\Delta}$ of the fDNS dataset is the same as the grid size of LES with $N_x \times N_y \times N_z = 48 \times 48 \times 48$ cells at $Re_\tau = 180$. Fourth-order commutative discrete filters by Vasilyev, Lund & Moin (1998) are utilised to construct the fDNS dataset and to conduct test filtering of LES. A total of 3.5×10^7 data points are sampled from five instantaneous velocity fields of fDNS after flow becomes fully developed, and 2.8×10^7 data points are used for training, whereas the rest are used for testing. It has been found that training with more than 2.8×10^7 data points (four instantaneous fDNS fields) does not show meaningful alteration of the ANN performance.

The ANN-SGS models are trained from scratch using the fDNS dataset of a turbulent channel flow by the same method in § 2.4, except for normalisation of the SGS stress. The normalisation factor of the SGS stress is estimated using the resolved stress tensor L_{ij} instead of the gradient model term since it is reported that the gradient model term has incorrect near-wall scaling (Liu *et al.* 1994) in contrast to the resolved stress tensor.

Each ANN-SGS model is named following the same rules as in § 2.4. The characters C and H at the end of the model names denote channel flow and homogeneous isotropic turbulence, respectively, and represent flow with which each ANN-SGS model is trained. For example, S-180C uses $\bar{S}_{ij}$ as the input, whereas SL-180C uses $\bar{S}_{ij}$ and L_{ij} as inputs, and both models are trained with turbulent channel flow at $Re_\tau = 180$. Model SL-106H180C is trained with both channel flow at $Re_\tau = 180$ and homogeneous isotropic turbulence at $Re_\lambda = 106$; SL-106H is only trained with homogeneous isotropic turbulence at $Re_\lambda = 106$.

	SL-180C	S-180C	SL-106H	DSM	DMM
$Corr(\tau_{xy}^{fDNS}, \tau_{xy}^{model})$	0.6528	0.4860	0.4149	0.1855	0.8797
$Corr(\varepsilon_{SGS}^{fDNS}, \varepsilon_{SGS}^{model})$	0.7994	0.6997	0.4203	0.2689	0.9053

Table 9. Correlation coefficients ($Corr(\tau_{xy}^{fDNS}, \tau_{xy}^{model})$, $Corr(\varepsilon_{SGS}^{fDNS}, \varepsilon_{SGS}^{model})$) from an *a priori* test of turbulent channel flow at $Re_\tau = 180$.

For training of SL-106H180C, the same amount of fDNS data points (2.8×10^7) from both homogeneous isotropic turbulence and turbulent channel flow are used to prevent the model from being biased. In addition, the same number of training samples are provided with the mini-batch size of 128 by extracting 64 fDNS data from homogeneous isotropic turbulence and turbulent channel flow, respectively.

Trained ANN-SGS models are initially evaluated in an *a priori* test of a turbulent channel flow at $Re_\tau = 180$ (table 9). The DSM shows poor correlation coefficients of the SGS stress and the SGS dissipation as reported by Park & Choi (2021). The SGS stress from DMM shows the best correlation coefficient of 0.88, a similar value reported by Salvetti & Banerjee (1995). Model SL-106H shows higher correlation coefficients than those of DSM even though the model is not trained with turbulent channel flow. Model SL-180C is more accurate than S-180C in predicting the SGS stress and the SGS dissipation, indicating that the use of L_{ij} in addition to $\bar{S}_{ij}$ as an input is also beneficial to the prediction of the SGS stress for channel flow.

In order to investigate the generalizability of the ANN-SGS models, the models are tested for LES of turbulent channel flow at various conditions listed in table 10. The Reynolds number and the grid size of LES180 case are the same as those of the training data (i.e. $Re_\tau = 180$, $N_x \times N_y \times N_z = 48 \times 48 \times 48$), and the remaining four cases correspond to untrained Reynolds number and grid resolution conditions.

Figure 25 shows results of the LES180 case. The DSM overpredicts the mean streamwise velocity and the streamwise velocity fluctuations $\bar{u}'_{rms}$, while underpredicts the wall-normal velocity fluctuations $\bar{v}'_{rms}$ and the spanwise velocity fluctuations $\bar{w}'_{rms}$. The overprediction of the mean streamwise velocity by DSM is consistent with the results of the previous studies (Horiuti 1997; Park & Choi 2021; Kim *et al.* 2022). In addition, it has been reported that LES with DSM exhibits overprediction of $\bar{u}'_{rms}$ and underpredictions of $\bar{v}'_{rms}$ and $\bar{w}'_{rms}$ (Park & Mahesh 2009; You & Moin 2007, 2009). The larger errors of LES with DSM than those of the no-SGS case in the prediction of velocity fluctuations have also been reported by Morinishi & Vasilyev (2001) and Cabot (1994). The DSM also shows slight underprediction of the mean Reynolds shear stress at $y^+ < 30$. Large-eddy simulation without an SGS model (no-SGS) underpredicts the mean streamwise velocity and overpredicts the Reynolds shear stress. However, SL-180C more accurately predicts the mean velocity, root-mean-squared (r.m.s.) velocity fluctuations, and the mean Reynolds shear stress than DSM and no-SGS. Model S-180C performs similar to SL-180C in terms of the velocity fluctuations and the Reynolds shear stress. However, S-180C shows slight underprediction of the mean streamwise velocity, compared with SL-180C. Model SL-106H180C shows almost identical performance to SL-180C, while showing slightly better prediction of the mean Reynolds shear stress at $y^+ > 40$. Interestingly, SL-106H is stable and accurately predicts the velocity fluctuations, despite the fact that it was trained only for homogeneous isotropic turbulence. The Reynolds shear stress of SL-106H shows

LES case	Re_τ	(L_x, L_z)	(N_x, N_y, N_z)	$(\Delta x^+, \Delta z^+)$	$(\Delta y^+_{min}, \Delta y^+_c)$	Model
LES180	180	$(4\pi\delta, \frac{4}{3}\pi\delta)$	(48, 48, 48)	(47.2, 15.7)	(0.33, 18.2)	SL-180C S-180C SL-106H180C SL-106H DSM no-SGS
LES180c	180	$(4\pi\delta, \frac{4}{3}\pi\delta)$	(32, 48, 32)	(70.8, 23.6)	(0.33, 18.2)	SL-180C SL-106H180C DSM no-SGS
LES180f	180	$(4\pi\delta, \frac{4}{3}\pi\delta)$	(64, 64, 64)	(35.4, 11.8)	(0.24, 13.7)	SL-180C SL-106H180C DSM no-SGS
LES395	395	$(2\pi\delta, \pi\delta)$	(48, 48, 48)	(52.0, 26.0)	(0.72, 40.0)	SL-180C S-180C SL-106H180C DSM no-SGS
LES395f	395	$(2\pi\delta, \pi\delta)$	(64, 64, 64)	(39.0, 19.5)	(0.53, 30.1)	SL-180C S-180C SL-106H180C DSM no-SGS

Table 10. Parameters for LES of turbulent channel flow with ANN-SGS models and DSM. The effects of grid resolution and the Reynolds number on the performance of ANN-SGS models are considered. Here L_x and L_z are the streamwise and spanwise domain sizes, respectively; δ is the channel half-width, and N_x, N_y and N_z are numbers of grid points in the streamwise, wall-normal, and spanwise directions, respectively; Δx^+ and Δz^+ are the streamwise and spanwise grid sizes in wall units, respectively; Δy^+_{min} and Δy^+_c are the wall-normal grid sizes at the wall and the centreline, respectively.

a similar error near $y^+ = 25$ and smaller errors at $y^+ > 45$, compared with that of DSM. However, SL-106H underpredicts the mean streamwise velocity, which is similar to that of no-SGS. Model SL-106H may inaccurately predict the SGS stress at wall-bounded flow since the mean of the SGS shear stress (off-diagonal components) vanishes (Kang *et al.* 2003) in homogeneous isotropic turbulence. Therefore, training an ANN-SGS model for a turbulent channel flow dataset seems to be essential to accurately predict the mean streamwise velocity.

Table 11 shows the averaged wall shear stress and the skin-friction coefficients ($C_f = 2\langle\tau_w\rangle/\rho U_b^2$, where τ_w is the wall shear stress and the bulk mean velocity $U_b = 1/2\delta \int_{-\delta}^{+\delta} \langle\bar{u}\rangle \mathrm{d}y$) of fDNS and LES for the LES180 case. Models SL-180C, S-180C and SL-106H180C predict the wall shear stress more accurately than DSM, while SL-106H shows a slightly larger deviation from that of DSM. On the other hand, the no-SGS case overestimates C_f, while LES with DSM underestimates C_f. The overestimation of C_f by the no-SGS case is also reported by Vreman (2004), although the computed Re_τ by the no-SGS case is in good agreement with that of DNS. Model SL-180C shows the most accurate prediction of C_f among tested models.

Figure 26 shows results in LES180c and LES180f cases that test the performance of ANN-SGS models on an untrained grid resolution. On a coarser grid resolution

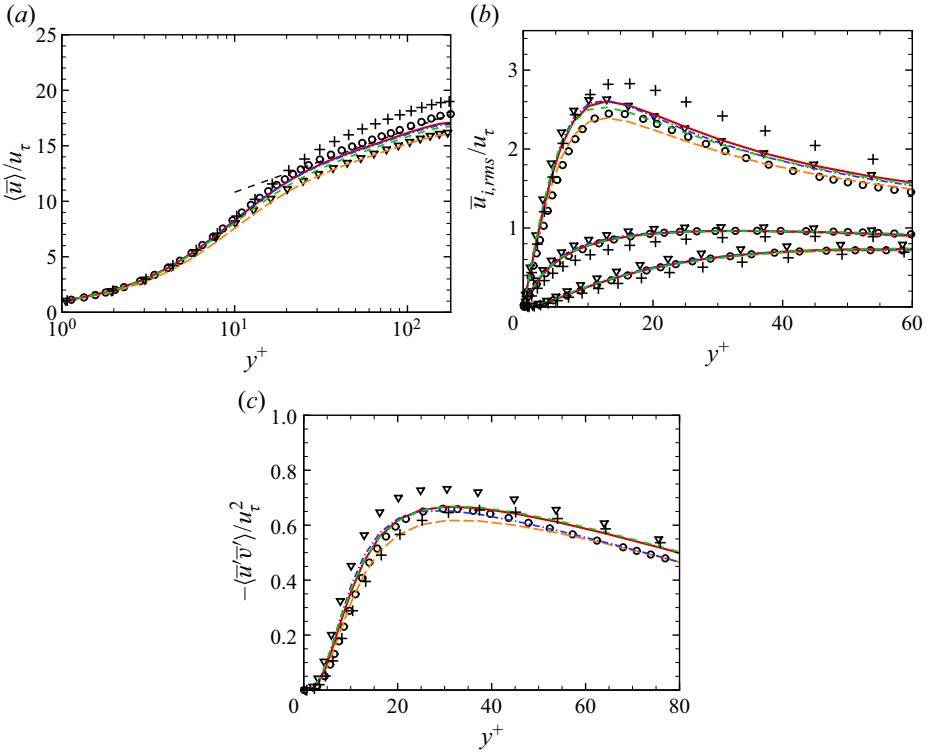

Figure 25. Results from fDNS and LES of turbulent channel flow at $Re_\tau = 180$ with a grid resolution of $48 \times 48 \times 48$ (LES180). (*a*) The mean streamwise velocity; (*b*) root-mean-squared (r.m.s.) velocity fluctuations; (*c*) the mean Reynolds shear stress $\langle\bar{u}'\bar{v}'\rangle$, where $\langle\cdot\rangle$ denotes averaging over the x–z plane and time. The three sets of curves in (*b*) represent $\bar{u}_{rms}/u_\tau$, $\bar{w}_{rms}/u_\tau$ and $\bar{v}_{rms}/u_\tau$ from top to bottom, respectively. Here ◯, fDNS; +, DSM; ∇, no-SGS; —— (thick red solid line), SL-180C; – – – (thick green dashed line), S-180C; – – – (thick blue dashed-dot line), SL-106H180C; – – (thick yellow orange dashed line), SL-106H; – – – (thick black dashed line), the law of the wall $\langle\bar{u}\rangle/u_\tau = 0.41^{-1}\log y^+ + 5.2$.

	fDNS	DSM	no-SGS	SL-180C	S-180C	SL-106H180C	SL-106H
$\langle\tau_w\rangle/\rho$	1.0109	0.9817	1.0067	1.0023	1.0276	1.0277	1.0413
error (%)	0.0	−2.89 %	−0.42 %	−0.85 %	1.65 %	1.66 %	3.00 %
C_f	0.0085	0.0072	0.0103	0.0092	0.0098	0.0096	0.0109

Table 11. Averaged wall shear stress $\langle\tau_w\rangle/\rho$ and the skin-friction coefficient C_f from fDNS and LES of a turbulent channel flow at $Re_\tau = 180$ with a grid resolution of $48 \times 48 \times 48$ (LES180), where $\langle\cdot\rangle$ denotes averaging over the x–z plane and time. Here $C_f = 2\langle\tau_w\rangle/\rho U_b^2$, where τ_w is the wall shear stress and the bulk mean velocity $U_b = 1/2\delta \int_{-\delta}^{+\delta}\langle\bar{u}\rangle \mathrm{d}y$.

(LES180c), DSM shows large errors in the prediction of the mean velocity and velocity fluctuations. Although DSM more accurately predicts the Reynolds shear stress than SL-180C and SL-106H180C (figure 26*e*), the mean streamwise velocity and the velocity fluctuations predicted by SL-180C and SL-106H180C are significantly better than those of DSM (figure 26*a*,*c*).

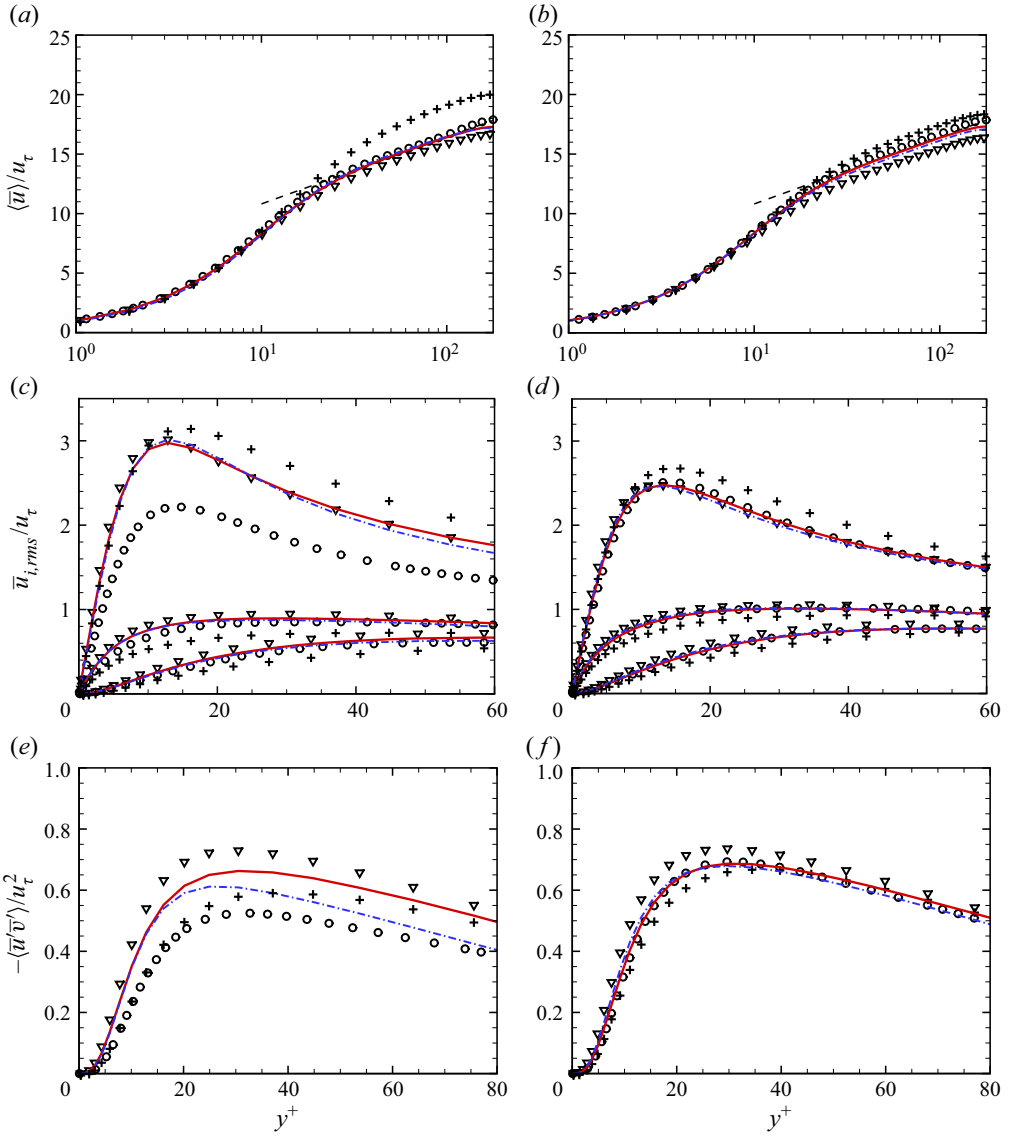

Figure 26. Results from fDNS and LES of turbulent channel flow at $Re_\tau = 180$ with a grid resolution of $32 \times 48 \times 32$ (*a*,*c*,*e*; LES180c) and $64 \times 64 \times 64$ (*b*,*d*,*f*; LES180f). (*a*,*b*) The mean streamwise velocity; (*c*,*d*) r.m.s. velocity fluctuations; (*e*,*f*) the mean Reynolds shear stress $\langle\bar{u}'\bar{v}'\rangle$, where $\langle\cdot\rangle$ denotes averaging over the x–z plane and time. The three sets of curves in (*c*,*d*) represent $\bar{u}_{rms}/u_\tau$, $\bar{w}_{rms}/u_\tau$ and $\bar{v}_{rms}/u_\tau$ from top to bottom, respectively. Here ◯, fDNS; +, DSM; ∇, no-SGS; —— (thick red solid line), SL-180C; – – – (thick blue dashed-dot line), SL-106H180C; – – - (thick black dashed line), the law of the wall $\langle\bar{u}\rangle/u_\tau = 0.41^{-1}\log y^+ + 5.2$.

On a finer grid resolution (LES180f), DSM slightly overpredicts the mean streamwise velocity. The DSM is less accurate than SL-180C and SL-106H180C in the prediction of the velocity fluctuations and the Reynolds shear stress. In contrast, all results of SL-180C and SL-106H180C are in excellent agreement with those of fDNS (figure 26*b*,*d*,*f*). Models SL-180C and SL-106H180C are found to perform better than DSM regardless of grid resolution.

The developed ANN-SGS models are tested for LES at a higher Reynolds number Re_τ of 395, and results are shown in figure 27. The DSM overpredicts the mean streamwise velocity in the LES395 and LES395f cases as shown in figures 27(*a*) and 27(*b*). Model S-180C underpredicts the mean streamwise velocity in both LES395 and LES395f cases, and the error becomes larger on a finer grid resolution (figure 27*a*,*b*). On the other hand, the mean velocity profiles of SL-180C and SL-106H180C are found to be closer to those of fDNS and less sensitive to grid resolution than DSM and S-180C.

In figures 27(*c*) and 27(*d*), DSM overpredicts $\bar{u}'_{rms}$ while it underpredicts $\bar{v}'_{rms}$ and $\bar{w}'_{rms}$. In contrast, S-180C, SL-180C and SL-106H180C show similar predictions of $\bar{u}'_{rms}$, $\bar{v}'_{rms}$ and $\bar{w}'_{rms}$ that are more accurate than those of DSM. In figures 27(*e*) and 27(*f*), DSM and S-180C similarly overpredict the Reynolds shear stress, while the Reynolds shear stress of SL-180C shows good agreement with that of fDNS. As SL-180C more accurately predicts the mean streamwise velocity and the Reynolds shear stress than S-180C, it can be concluded that the use of L_{ij} in addition to the $\bar{S}_{ij}$ as an input improves the performance of the ANN-SGS model for a turbulent channel flow, similarly to the case of homogeneous isotropic turbulence. In LES of a turbulent channel flow (figures 25, 26 and 27), SL-106H180C performs similarly to SL-180C, especially in the prediction of the mean velocity and the velocity fluctuations.

In figure 28 a qualitative comparison of vortical structures is shown by isosurfaces of Q that is defined as the second invariant of the velocity gradient tensor from fDNS and LES for the LES395f case. Similar scales and distributions of flow structures to those of fDNS are observed by SL-180C, S-180C and DSM, while significantly more vortical structures are found in the flow field of no-SGS due to the lack of SGS dissipation (Park & Choi 2021).

Additionally, it is tested whether SL-106H180C provides accurate solutions for LES of decaying isotropic turbulence, and the results are shown in figure 29. Model SL-106H180C shows almost identical performance to SL-106H in the prediction of energy spectra and the resolved kinetic energy. Therefore, the present ANN-SGS mixed model that is trained with isotropic turbulence and turbulent channel flow at a given Reynolds number and grid resolution condition (SL-106H180C) is found to be capable of accurately and stably predicting both turbulent channel flow and isotropic turbulence flow at untrained Reynolds number and grid resolution conditions.

3.6. *Normalisation of input and output variables for turbulent channel flow*

In § 3.5 the input and output variables of ANN-SGS models are normalised with volume-averaged quantities as done in homogeneous isotropic turbulence. However, as flow variables are inhomogeneous in the wall-normal direction in the case of a turbulent channel flow, normalisation with plane-averaged quantities can also be considered. Thus, two different normalisations for ANN-SGS models using plane-averaged and volume-averaged quantities (denoted as plane-wise normalisation and volume-wise normalisation hereafter, respectively) are compared in this section. For plane-wise normalisation, variables are normalised in every wall-parallel plane with plane-averaged quantities. The additional character V or P is added at the end of the model names to denote volume-wise normalisation or plane-wise normalisation, respectively.

Although, as shown in figures 30(*d*) and 30(*e*), SL-180C-P is found to be more accurate in the prediction of the mean SGS shear stress, SL-180C-V provides a more accurate prediction of the backscatter. However, as shown in figures 30(*a*), 30(*b*) and 30(*c*), no significant differences in the mean streamwise velocity, r.m.s. velocity fluctuations and

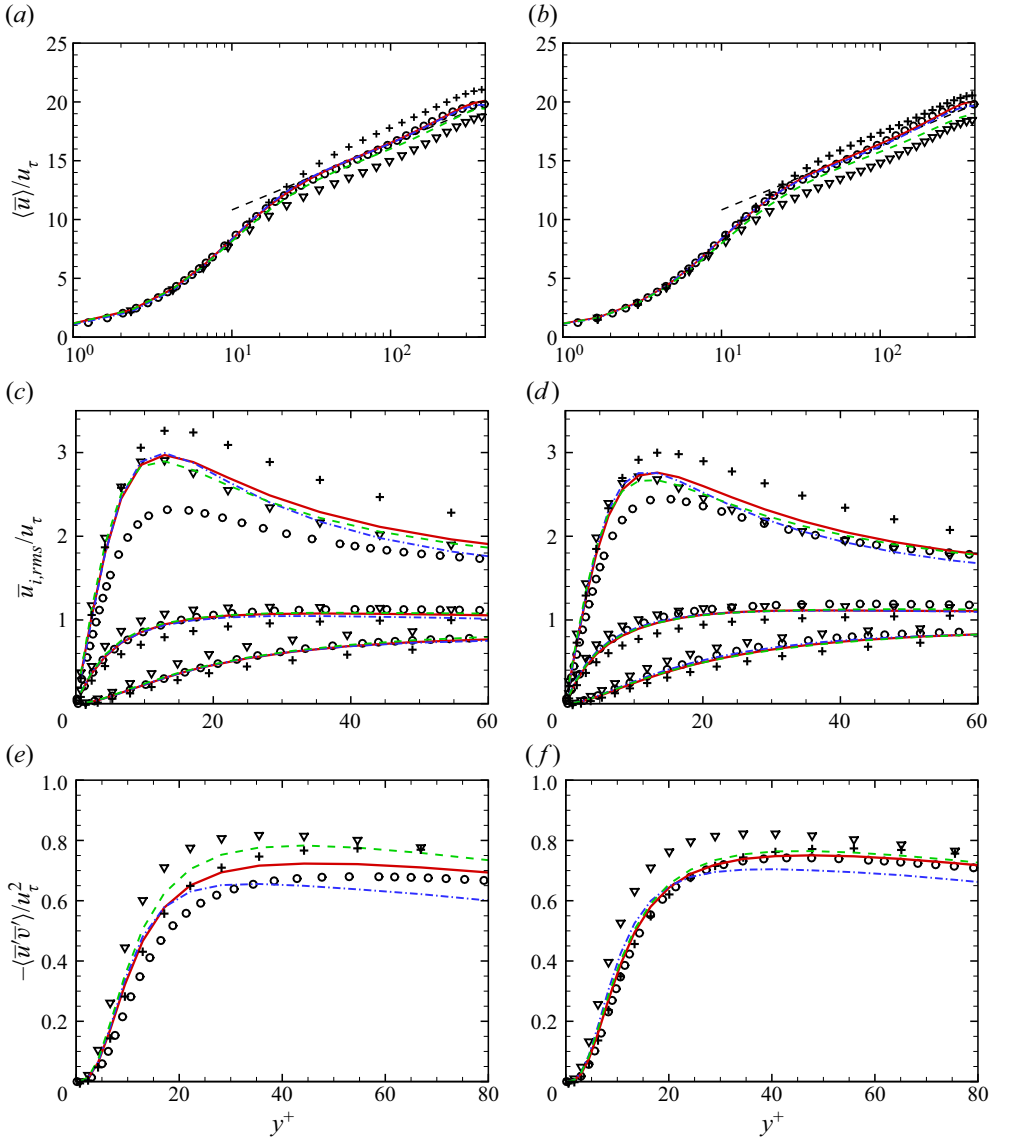

Figure 27. Results from fDNS and LES of a turbulent channel flow at $Re_\tau = 395$ with a grid resolution of $48 \times 48 \times 48$ (*a*,*c*,*e*; LES395) and $64 \times 64 \times 64$ (*b*,*d*,*f*; LES395f). (*a*,*b*) The mean streamwise velocity; (*c*,*d*) r.m.s. velocity fluctuations; (*e*,*f*) the mean Reynolds shear stress $\langle\bar{u}'\bar{v}'\rangle$, where $\langle\cdot\rangle$ denotes averaging over the x–z plane and time. The three sets of curves in (*c*,*d*) represent $\bar{u}_{rms}/u_\tau$, $\bar{w}_{rms}/u_\tau$ and $\bar{v}_{rms}/u_\tau$ from top to bottom, respectively. Here ◯, fDNS; +, DSM; ∇, no-SGS; —— (thick red solid line), SL-180C; – – – (thick green dashed line), S-180C; – – – (thick blue dashed-dot line), SL-106H180C; – – – (thick black dashed line), the law of the wall $\langle\bar{u}\rangle/u_\tau = 0.41^{-1}\log y^+ + 5.2$.

the Reynolds shear stress in SL-180C-P and SL-180C-V are found. The same trends are observed in the comparison of results from S-180C-P and S-180C-V. The volume-wise averaging is not taken on the output SGS stress itself but only on the normalisation factor that is used for regularising the input and output data range. In addition, important physical characteristics of SL-180C-V, such as the near-wall behaviour of the SGS stress (figure 30*d*) and the backscatter (figure 30*e*), remain accurate even when volume-wise

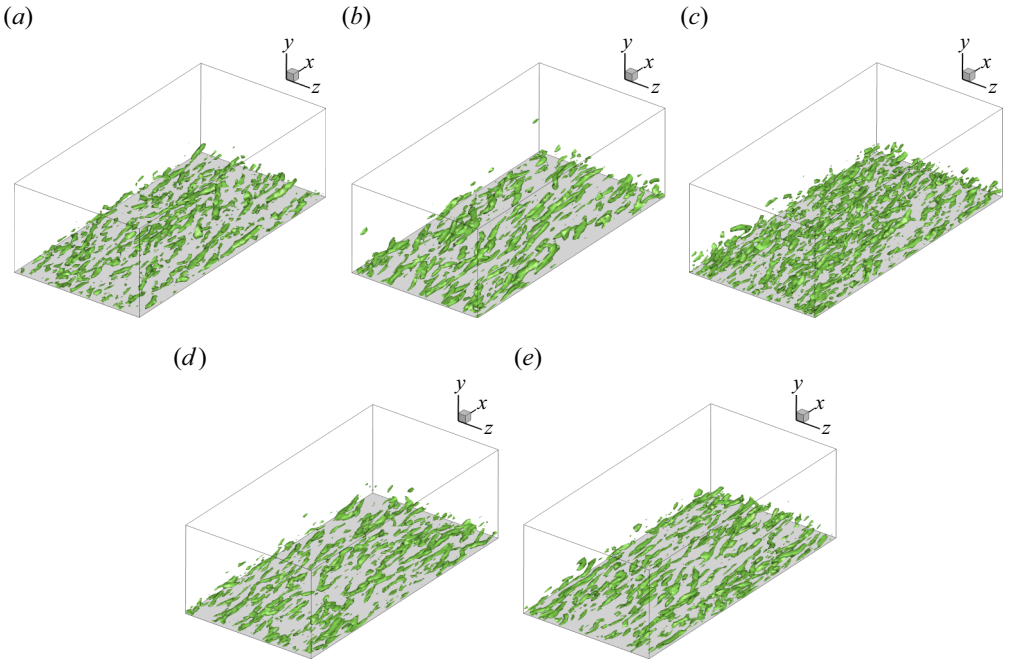

Figure 28. Isosurfaces of $Q = 0.0025u_\tau^4/\nu^2$ from fDNS and LES of a turbulent channel flow at $Re_\tau = 395$ with a grid resolution of $64 \times 64 \times 64$ (LES395f). Results are shown for (*a*) fDNS, (*b*) DSM, (*c*) no-SGS, (*d*) SL-180C, (*e*) S-180C.

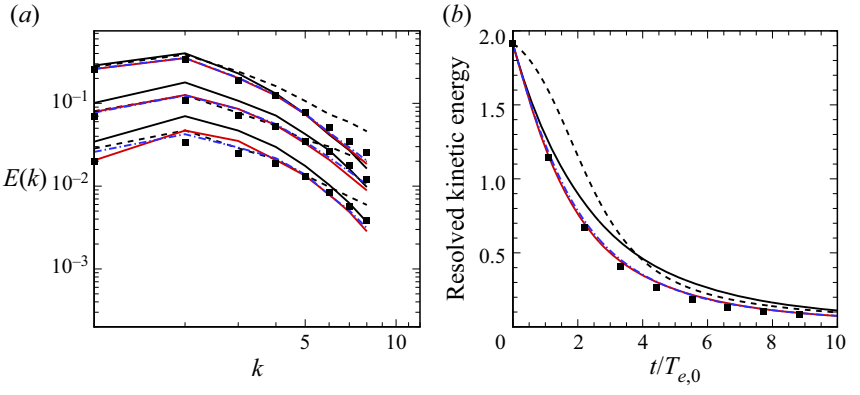

Figure 29. Results from fDNS and LES of decaying isotropic turbulence at the initial Reynolds number Re_λ of 106 with a grid resolution of 48^3. (*a*) Energy spectra at $t/T_{e,0} = 1.1$, 3.3 and 6.6; (*b*) temporal evolution of the resolved kinetic energy. Here ■, fDNS; —— (thick black solid line), DSM; – – - (thick black dashed line), no-SGS; – – - (thick blue dashed-dot line), SL-106H180C; —— (thick red solid line), SL-106H.

normalisation is used. However, it is worth noting that an ANN-SGS model trained with plane-wise normalisation is applicable only when statistically homogeneous directions exist.

On the other hand, as shown in figure 30(*a*), it is found that the plane-wise normalisation in SL-106H-P produces the mean streamwise velocity more accurately than the volume-wise normalisation in SL-106H-V. The mean SGS shear stress by SL-106H-V

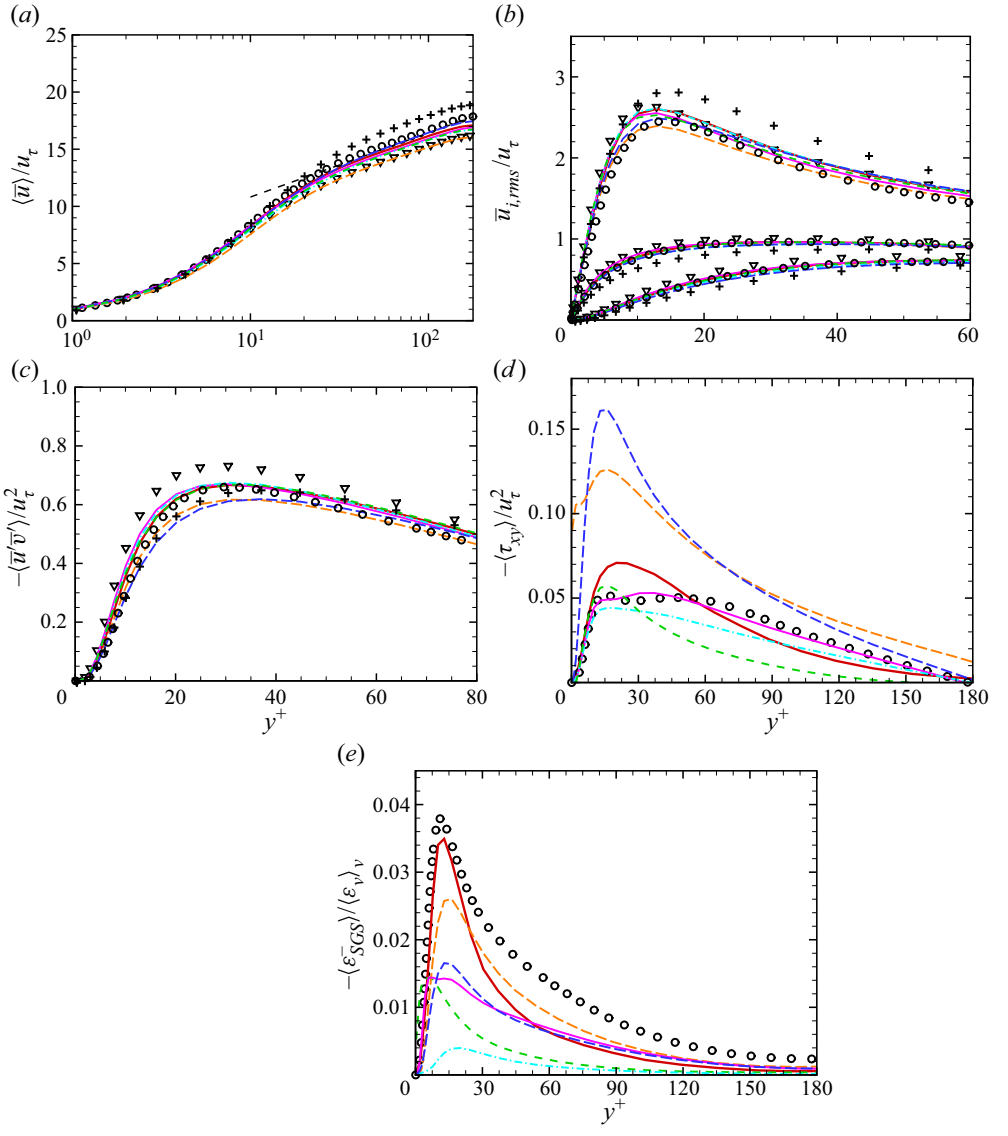

Figure 30. Results from fDNS and LES of a turbulent channel flow at $Re_\tau = 180$ with a grid resolution of 48 × 48 × 48 (LES180). (*a*) The mean streamwise velocity; (*b*) r.m.s. velocity fluctuations; (*c*) the mean Reynolds shear stress $\langle\bar{u}'\bar{v}'\rangle$; (*d*) the mean SGS shear stress $\langle\tau_{xy}\rangle$; (*e*) the mean backscatter $\langle\varepsilon_{SGS}^-\rangle = \frac{1}{2}\langle\varepsilon_{SGS} - |\varepsilon_{SGS}|\rangle$, where $\langle\cdot\rangle$ denotes averaging over the x–z plane and time. The three sets of curves in (*b*) represent $\bar{u}_{rms}/u_\tau$, $\bar{w}_{rms}/u_\tau$ and $\bar{v}_{rms}/u_\tau$ from top to bottom, respectively. Here ◯, fDNS; +, DSM; ∇, no-SGS; —— (thick red solid line), SL-180C-V; – – – (thick green dashed line), S-180C-V; – – (thick yellow orange dashed line), SL-106H-V; —— (thick magenta solid line), SL-180C-P; – – – (thick cyan dashed-dot line), S-180C-P; – – (thick blue dashed line), SL-106H-P; – – – (thick black dashed line), the law of the wall $\langle\bar{u}\rangle/u_\tau = 0.41^{-1}\log y^+ + 5.2$.

does not vanish at the wall since SL-106H-V was not trained with the SGS stress distribution near the wall (figure 30*d*). Compared with SL-180C-V that is trained with channel flow, the mean SGS shear stress is overall overestimated by SL-106H-V, leading to an underestimated Reynolds shear stress (figure 30*c*). Interestingly, the mean SGS shear stress by SL-106H-P vanishes at the wall, which seems to improve the prediction

of the mean streamwise velocity, regardless of the inaccurate prediction of the mean SGS shear stress. Therefore, plane-wise normalisation is found to improve the applicability of the ANN-based mixed SGS model that is trained only with the homogeneous isotropic turbulence to an untrained turbulent channel flow.

Regardless of the normalisation method, providing L_{ij} in addition to the $\bar{S}_{ij}$ as an input is beneficial to the prediction of the backscatter and the mean SGS shear stress (figure 30*d*,*e*). Although the mean streamwise velocity and r.m.s.velocity fluctuations from SL-180C-V and S-180C-V are similar to each other, S-180C-V significantly underestimates the backscatter, which is consistent with the results from LES of homogeneous isotropic turbulence. In addition, SL-180C-V more accurately predicts the mean SGS shear stress than S-180C-V. The similar trend is observed in the comparison of SL-180C-P and S-180C-P. Model SL-180C-P is found to more accurately predict the mean SGS shear stress and the backscatter. Owing to the better prediction of the SGS shear stress and backscatter, SL-180C is considered to better predict channel flow at a higher Reynolds number $Re_\tau = 395$ than S-180C as shown in figure 27.

3.7. *Application of ANN-SGS models trained with homogeneous isotropic turbulence to turbulent channel flow*

In this section it is discussed how SL-106H that is trained only with homogeneous isotropic turbulence is partially successful in the prediction of the SGS stress for a turbulent channel flow. As discussed in § 3.1, the ANN-SGS mixed model combines two input tensors ($\bar{S}_{ij}$ and L_{ij}) to produce the SGS stress. Therefore, the investigation of statistical relations between each input tensor and the true SGS stress for homogeneous isotropic turbulence and a turbulent channel flow is important.

Correlation coefficients between each input tensor and the true SGS stress for both flows from *a priori* tests are shown in tables 12 and 13. Because $Corr(\bar{S}_{ij}, \tau_{ij})$ and $Corr(L_{ij}, \tau_{ij})$ from fDNS are different in the two flows, it can be concluded that $\bar{S}_{ij}$ and L_{ij} contribute differently to the prediction of the SGS stress. In particular, the absolute value of $Corr(\bar{S}_{ij}, \tau_{ij})$ from fDNS is close to zero in a turbulent channel flow (see table 13) while it is close to 0.3 in homogeneous isotropic turbulence (see table 12), which implies that the relative importance of $\bar{S}_{ij}$ for the prediction of τ_{ij} should be considerably different. Such difference in relative importance of $\bar{S}_{ij}$ is particularly noticeable in the observation of the near-wall behaviours of both input tensors and the SGS stress. As shown in figure 31(*a*), in fDNS, $\langle \bar{S}_{xy} \rangle$ increases as y^+ approaches 0 whereas $\langle \tau_{xy} \rangle$ decreases from the peak value near the wall as shown in figure 31(*d*). On the other hand, $\langle L_{xy} \rangle$ shows a similar distribution to $\langle \tau_{xy} \rangle$ as shown in figures 31(*b*) and 31(*d*).

These observations explain the incorrect prediction of $\langle \tau_{xy} \rangle$ near the wall by S-106H-V in figure 31(*d*) since S-106H-V only uses $\bar{S}_{xy}$ to produce τ_{xy}. The absolute value of $Corr(\bar{S}_{xy}, \tau_{xy})$ from S-106H-V in a turbulent channel flow is close to 1 indicating that S-106H-V predicts the SGS stress nearly aligned with $\bar{S}_{ij}$. This leads to the prediction of $\langle \tau_{xy} \rangle$ by S-106H-V of which the near-wall behaviour mimics that of $\langle \bar{S}_{xy} \rangle$. Consequently, S-106H-V significantly overestimates the mean SGS dissipation $\langle \varepsilon_{SGS} \rangle$ near the wall (figure 31*e*).

Model SL-106H-V, on the other hand, predicts $\langle \tau_{xy} \rangle$ near the wall more accurately than S-106H-V. This is because (i) SL-106H-V highly relies on L_{ij} to predict the tensor alignment of τ_{ij} that can be confirmed from tables 12 and 13 where $Corr(L_{ij}, \tau_{ij})$ values of SL-106H are higher than 0.8 for both types of flow, and (ii) L_{ij} has high similarity to

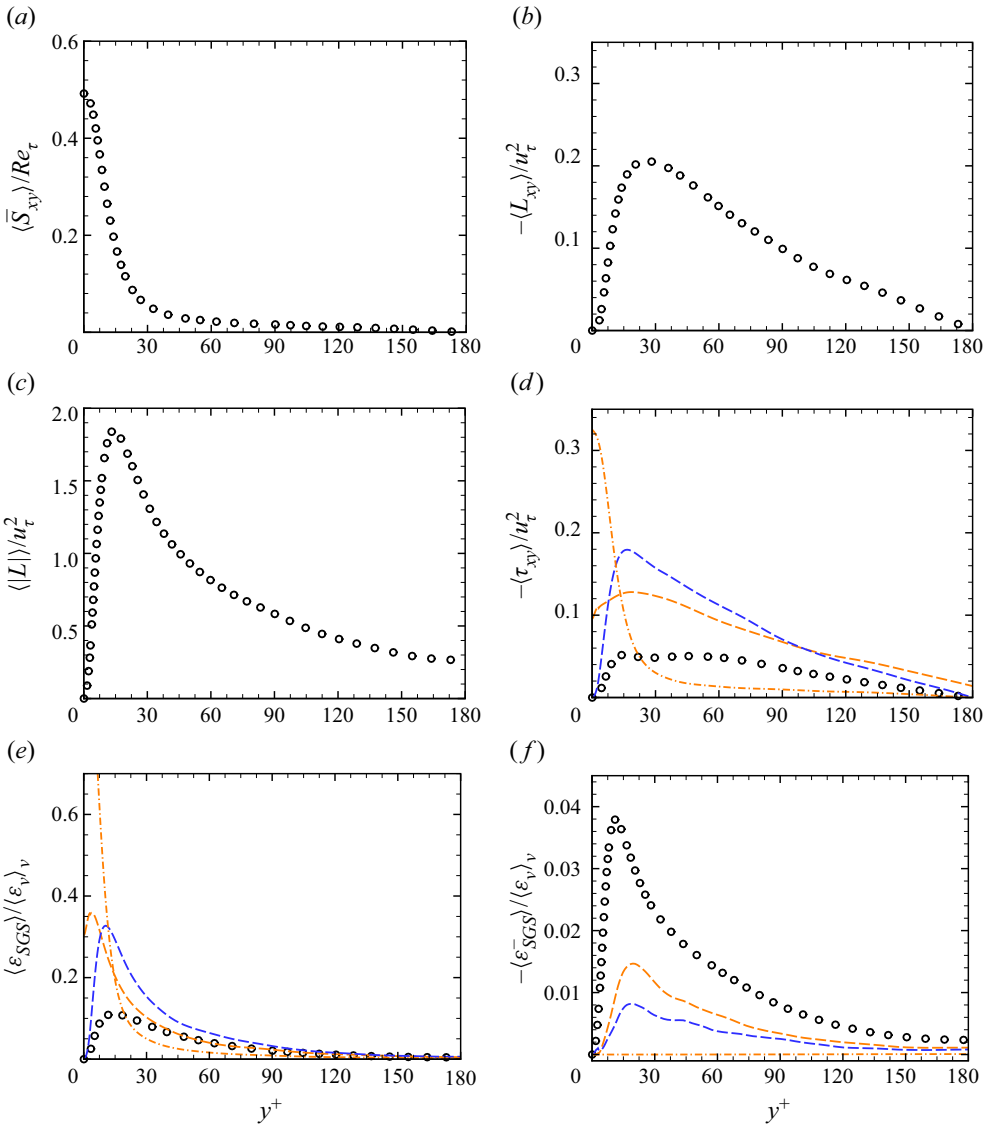

Figure 31. Results from an *a priori* test of a turbulent channel flow at $Re_\tau = 180$. (*a*) Strain-rate tensor $\langle \bar{S}_{xy} \rangle$, (*b*) resolved stress tensor $\langle L_{xy} \rangle$, (*c*) L_2 norm of resolved stress tensor $\langle |L| \rangle$, (*d*) SGS shear stress $\langle \tau_{xy} \rangle$, (*e*) SGS dissipation $\langle \varepsilon_{SGS} \rangle$ and (*f*) backscatter $\langle \varepsilon^-_{SGS} \rangle = \frac{1}{2} \langle \varepsilon_{SGS} - |\varepsilon_{SGS}| \rangle$, where $\langle \cdot \rangle$ denotes averaging over the x–z plane and time. Here ◯, fDNS; – – (thick yellow orange dashed line), SL-106H-V; – – – (thick yellow orange dashed-dot line), S-106H-V; – – (thick blue dashed line), SL-106H-P.

the SGS stress in terms of the correlation coefficient to the true SGS stress (table 13) and the near-wall behaviour (figure 31). It is noteworthy that Zang *et al.* (1993) reported that the scale-similarity part of the dynamic mixed model (the modified Leonard term) shows significant contribution to the Reynolds stress near the wall, while the contribution of the eddy-viscosity part is negligible.

Consequently, SL-106H-V shows an improved near-wall behaviour of the mean SGS shear stress $\langle \tau_{xy} \rangle$ as it is influenced by the near-wall behaviour of the mean resolved stress $\langle L_{xy} \rangle$. Model SL-106H-P shows the best near-wall behaviour among the tested models

	fDNS	SL-106H	S-106H
$Corr(\bar{S}_{12}, \tau_{12})$	−0.2806	−0.3992	−0.8217
$Corr(\bar{S}_{13}, \tau_{13})$	−0.2849	−0.3993	−0.8370
$Corr(\bar{S}_{23}, \tau_{23})$	−0.2825	−0.3806	−0.8172
$Corr(L_{12}, \tau_{12})$	0.6620	0.9553	0.3505
$Corr(L_{13}, \tau_{13})$	0.6712	0.9423	0.3200
$Corr(L_{23}, \tau_{23})$	0.6878	0.9518	0.3507

Table 12. Correlation coefficients ($Corr(\bar{S}_{ij}, \tau_{ij})$, $Corr(L_{ij}, \tau_{ij})$) between the input variables and the predicted SGS stress by ANN-SGS models from an *a priori* test of forced homogeneous isotropic turbulence at $Re_\lambda = 106$.

since the L_2 norm of L_{ij}, which is multiplied to the output of SL-106H-P for rescaling, shows a correct near-wall behaviour at the wall (figure 31*c*).

However, SL-106H-V and SL-106H-P show higher absolute values of $Corr(\bar{S}_{xy}, \tau_{xy})$ than those of SL-180C-V and fDNS in channel flow (table 13), which indicates the contribution of $\bar{S}_{ij}$ for τ_{ij} is overestimated. Since $Corr(\bar{S}_{xy}, \tau_{xy})$ of fDNS has a small absolute value of 0.08 in channel flow, alignment of τ_{ij} is inaccurately predicted when the contribution of $\bar{S}_{ij}$ is overestimated. This explains the overprediction of the SGS stress and the SGS dissipation in figures 31(*d*) and 31(*e*).

It is also investigated whether SL-106H-V and SL-106H-P can reflect the anisotropy of L_{ij} to produce τ_{ij} in a turbulent channel flow. In order to quantitatively compare the anisotropy of the predicted SGS stress by ANN-SGS models, the anisotropy invariant maps (Lumley & Newman 1977) of the SGS anisotropy tensor are examined in figure 32. The SGS anisotropy tensor is defined as (Rasam *et al.* 2016; Inagaki & Kobayashi 2020)

$$a_{ij} = \frac{\langle \tau_{ij} \rangle}{\langle \tau_{kk} \rangle} - \frac{1}{3}\delta_{ij}, \tag{3.9}$$

where $\langle \cdot \rangle$ denotes averaging over the x–z plane and time. The anisotropy invariant maps are constructed based on the two invariants of the anisotropy tensor a_{ij},

$$II = a_{ij}a_{ij}, \quad III = a_{ik}a_{kj}a_{ji}, \tag{3.10a,b}$$

where II and III are the second and third invariants of a_{ij}, respectively. The invariant map lies in the region bounded by the limits of the two-component turbulence state ($II = 2/9 + 2III$) and the axisymmetric turbulence state ($II = 3/2(4/3|III|)^{2/3}$). The triangular region defined by the limits represents the realizability condition for the invariants of the SGS tensor.

In the invariant map, the two-component turbulence ($II = 2/9 + 2III$), which is the condition in which the wall-normal component is negligible relative to the other two components, occurs at the wall (Inagaki & Kobayashi 2020). The right curved edgy is the axisymmetric turbulence in which the streamwise component is larger than the other two components (Rasam *et al.* 2016). The origin corresponds to the isotropic turbulence state that occurs at the channel centreline.

The invariant map for SL-180C-V approaches the top right corner and ends at the two-component limit as it approaches the wall, indicating that SL-180C-V represents the anisotropy of the SGS stress similar to the true SGS stress. The invariant map of L_{ij} indicates that L_{ij} itself has similar anisotropy to that of the true SGS stress.

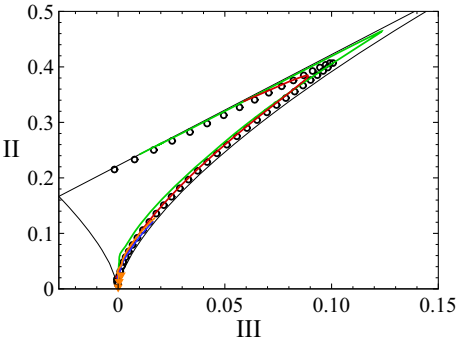

Figure 32. Anisotropy invariant maps of the SGS stress anisotropy tensor from an *a priori* test of a turbulent channel flow at $Re_\tau = 180$. Here ◯, fDNS; —— (thick green solid line), L_{ij}; —— (thick red solid line), SL-180C-V; —— (thick yellow orange solid line), SL-106H-V; —— (thick blue solid line), SL-106H-P; ▼ (yellow orange triangle), S-106H-V.

Since the invariant map of S-106H-V remains near the origin, it is concluded that the SGS stress predicted by S-106H-V is isotropic. On the other hand, the SGS stress from SL-106H-V and SL-106H-P show larger anisotropy than that of S-106H-V as the invariant maps follow the axisymmetric limit, which represents the streamwise component becoming larger than the other two components. Due to the large contribution of L_{ij} for predicting τ_{ij} by SL-106H-V and SL-106H-P, they represent a limited magnitude of anisotropy by indirectly accounting for the anisotropy of L_{ij}. However, the anisotropy magnitude is significantly underestimated and the invariant map does not approach the two-component turbulence state at the wall. This indicates that SL-106H-V and SL-106H-P are not fully capable of representing the asymptotic behaviour of the SGS stress near the wall since they are not trained with channel flow.

In figure 33 results from an *a posteriori* test of a turbulent channel flow are presented to compare the ANN-SGS models trained only with homogeneous isotropic turbulence. Model S-106H-V shows a significant underprediction of the mean streamwise velocity due to the inaccurate prediction of the SGS shear stress and the SGS dissipation, although the model employs the same normalisation of variables with SL-106H-V. Model S-106H-V also shows poor prediction of the r.m.s.velocity fluctuations and the mean Reynolds shear stress. Compared with SL-106H-V, SL-106H-P that employs plane-wise normalisation further improves the near-wall behaviour of the SGS shear stress and the prediction of the mean streamwise velocity since the rescaling factor ($\langle |L| \rangle_{x-z}$) becomes zero at the wall (figure 31*c*).

In summary, since the strain-rate tensor that is almost aligned with the SGS stress in S-106H-V is poorly correlated to the true SGS stress and has an inaccurate near-wall behaviour, proper normalisation of variables is not enough for accurate prediction of a turbulent channel flow. Improved results by SL-106H-V and SL-106H-P are explained as they predict the SGS stress using L_{ij} that has high similarity to the true SGS stress in terms of the near-wall behaviour and anisotropy. Therefore, the most important factor for generalization to an untrained turbulent channel flow is considered to be the use of L_{ij}.

4. Conclusions

In the present study an ANN-based mixed SGS model applicable to LES of turbulent flow under untrained Reynolds number and grid resolution conditions has been developed.

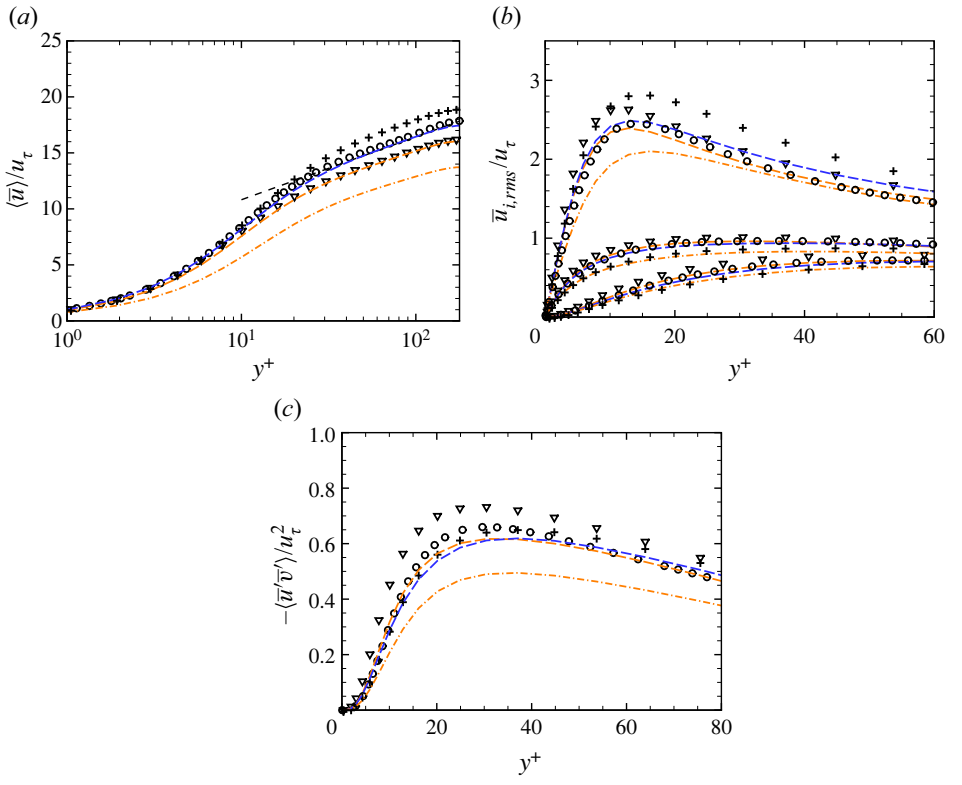

Figure 33. Results from fDNS and LES of a turbulent channel flow at $Re_\tau = 180$ with a grid resolution of $48 \times 48 \times 48$ (LES180). (*a*) The mean streamwise velocity; (*b*) r.m.s. velocity fluctuations; (*c*) the mean Reynolds shear stress $\langle\bar{u}'\bar{v}'\rangle$, where $\langle\cdot\rangle$ denotes averaging over the x–z plane and time. The three sets of curves in (*b*) represent $\bar{u}_{rms}/u_\tau$, $\bar{w}_{rms}/u_\tau$ and $\bar{v}_{rms}/u_\tau$ from top to bottom, respectively. Here ◯, fDNS; +, DSM; ∇, no-SGS; – – (thick yellow orange dashed line), SL-106H-V; – – – (thick yellow orange dashed-dot line), S-106H-V; – – (thick blue dashed line), SL-106H-P; – – - (thick black dashed line), the law of the wall $\langle\bar{u}\rangle/u_\tau = 0.41^{-1}\log y^+ + 5.2$.

The predictive capabilities of two different ANN-SGS models that use either the resolved strain-rate tensor ($\bar{S}_{ij}$) as the only input (ANN-SGS model) or the combination of the resolved strain-rate tensor and the resolved stress tensor ($\bar{S}_{ij}$ and L_{ij}) as the inputs (ANN-SGS mixed model) to predict the six components of the SGS stress tensor have been examined for forced and decaying isotropic turbulence and turbulent flow through a channel.

From *a priori* tests with forced isotropic turbulence, it was found that the ANN-SGS model with the resolved strain-rate tensor as the only input predicts the SGS stress that is nearly aligned with the given input strain-rate tensor instead of the true SGS stress. In addition, in an *a posteriori* test for the same flow, the ANN-SGS model showed almost identical performance to that of the algebraic DSM in terms of the energy spectrum and p.d.f.s of the SGS dissipation and the SGS stress. To improve the accuracy of the predicted SGS stress as well as its misalignment to the true SGS stress, the ANN-SGS mixed model has been devised using the resolved stress tensor as an additional input based on the concept of the algebraic dynamic mixed SGS models.

The ANN-SGS mixed model has been found to predict the SGS stress with higher correlation coefficients to the true SGS stress and to provide more accurate p.d.f.s of the

SGS dissipation and SGS stress than the ANN-SGS model. In addition, the ANN-SGS mixed model has been found to predict the SGS stress with closer alignment with the true SGS stress than the ANN-SGS model. At the same time, the present ANN-SGS mixed model has been found to perform better than the algebraic DSM and the ANN-SGS model in an *a posteriori* test with forced isotropic turbulence in terms of the energy spectrum and the p.d.f. of the SGS dissipation.

The present ANN-SGS mixed model also has additional advantages over the algebraic dynamic SGS models in that the model predicts the SGS stress with less computational cost and does not necessitate *ad hoc* stabilisation procedures for numerical stability. Compared with the algebraic dynamic mixed models (Zang *et al.* 1993; Vreman *et al.* 1994; Anderson & Meneveau 1999), the present ANN-SGS mixed model has been found to more accurately predict energy spectra and temporal evolution of the resolved kinetic energy of decaying isotropic turbulence without any *ad hoc* stabilisation procedures. The computational time required for the ANN-SGS mixed model to produce the SGS stress has been found to be notably less than that of the algebraic dynamic mixed models and even that of the DSM.

For generalization of the ANN-SGS models to LES of untrained flows, it has been found that proper selection of normalisation factors such that distributions of the normalised input and output variables remain unchanged as the Reynolds number and grid resolution vary is crucial. From *a priori* and *a posteriori* studies with forced and decaying homogeneous isotropic turbulence and turbulent channel flow, it has been found that averaged L_2 norms of the gradient model term and the resolved stress term can be the good scaling factor $\langle|\tau|\rangle$ for normalisation of the output SGS stress tensor as $\tau_{ij}^* = \tau_{ij}/\langle|\tau|\rangle$, while the magnitudes of the resolved strain-rate tensor and the resolved stress tensor are sufficient for normalisation of the input variables as $\bar{S}_{ij}^* = \bar{S}_{ij}/\langle|\bar{S}|\rangle$ and $L_{ij}^* = L_{ij}/\langle|L|\rangle$ since they maintain the most constant distributions of the input and output variables for various Reynolds numbers and grid resolution.

The present ANN-SGS mixed model trained only with forced homogeneous isotropic turbulence has been found to be successfully generalized for LES of untrained transient decaying homogeneous isotropic turbulence. The ANN-SGS mixed model has been found to predict energy spectra and temporal evolution of the resolved kinetic energy more accurately than DSM and the ANN-SGS model. Furthermore, the ANN-SGS mixed model has shown consistently good performance in LES of decaying homogeneous isotropic turbulence with various untrained initial Reynolds numbers and grid resolution.

Lastly, it has been investigated whether the developed ANN-SGS mixed model can be applied to a wall-bounded turbulent flow. The present ANN-SGS mixed model has been found to be capable of predicting the SGS stress and thereby the mean and fluctuating velocity fields of a turbulent channel flow. If the model was trained with a turbulent channel flow at a certain Reynolds number and a certain grid resolution, the model accurately predicted a turbulent channel flow even at an untrained Reynolds number and on an untrained grid resolution. The ANN-SGS mixed model trained with forced homogeneous isotopic turbulence only has been found to also be capable of predicting the Reynolds shear stress and velocity fluctuations favourably with a marginal underprediction of the mean velocity profile. Generalization of the ANN-SGS mixed model to an untrained turbulent channel flow is considered to be realizable as the model predicts the SGS stress using L_{ij} that has high similarity to the true SGS stress in terms of the near-wall behaviour and the anisotropy. Interestingly, the ANN-SGS mixed model trained with both homogeneous isotropic turbulence and turbulent channel flow has provided consistently accurate and stable solutions for both types of flow.

	fDNS	SL-180C-V	SL-106H-V	S-106H-V	SL-106H-P
$Corr(\tau_{xy}^{fDNS}, \tau_{xy}^{ANN})$	—	0.6528	0.4149	0.0796	0.4404
$Corr(\bar{S}_{xy}, \tau_{xy})$	−0.0765	−0.1224	−0.5559	−0.9945	−0.3194
$Corr(L_{xy}, \tau_{xy})$	0.4581	0.6923	0.8687	0.1446	0.9141
$Corr(\varepsilon_{SGS}^{fDNS}, \varepsilon_{SGS}^{ANN})$	—	0.7994	0.4203	0.1416	0.5705

Table 13. Correlation coefficients ($Corr(\tau_{xy}^{fDNS}, \tau_{xy}^{ANN})$, $Corr(\bar{S}_{xy}, \tau_{xy})$, $Corr(L_{xy}, \tau_{xy})$, $Corr(\varepsilon_{SGS}^{fDNS}, \varepsilon_{SGS}^{ANN})$) from an *a priori* test of a turbulent channel flow at $Re_\tau = 180$.

DNS case	$q^2/2$	ε	λ	Re_λ
Langford & Moser (1999)	41.1	62.9	0.209	164
Present study with the negative viscosity forcing	30.2	60.3	0.183	122.9
Present study with the deterministic viscosity forcing	41.2	64.5	0.235	164.7

Table 14. Comparison of turbulence statistics from DNS of Langford & Moser (1999) and those from the present DNS using the negative viscosity forcing and the deterministic forcing. Here $q^2/2$ is kinetic energy, ε is dissipation, λ is the Taylor microscale and Re_λ is the Taylor-scale Reynolds number.

Funding. This work was supported by the National Research Foundation of Korea (NRF) under grant number NRF-2021R1A2C2092146 and the Samsung Research Funding Center of Samsung Electronics under project number SRFC-TB1703-51.

Declaration of interests. The authors report no conflict of interest.

Author ORCIDs.
Myeongseok Kang https://orcid.org/0000-0003-0043-4880;
Youngmin Jeon https://orcid.org/0000-0003-4261-0280;
Donghyun You https://orcid.org/0000-0003-2470-5411.

Appendix A. Forcing schemes used at $Re_\lambda = 164$

While Langford & Moser (1999) reported the use of a negative viscosity forcing for simulating forced homogeneous isotropic turbulence at $Re_\lambda = 164$, both the deterministic forcing and the negative viscosity forcing are used in the present study. The energy spectrum reported in Langford & Moser (1999) is almost identical to that of the case in which the deterministic forcing is used as shown in figure 1(*b*). Furthermore, the value of Re_λ calculated from the cases with the deterministic forcing and the negative viscosity forcing are found to be 165 and 123 (table 14), respectively, where the former case is close to the reported value of 164 by Langford & Moser (1999). Turbulence statistics reported in Langford & Moser (1999) have also been successfully reproduced using the deterministic forcing as shown in table 14.

While the major differences in the energy spectra obtained using different types of forcing schemes are observed to be in the forcing wavenumber range as shown in figure 1(*b*), the characteristics of each forcing scheme can be inferred from (2.3) and (2.4). The deterministic forcing scheme (2.4) acting on each wavenumber shell is weighted by the Fourier coefficient of the velocity at each wavenumber shell. In forced homogeneous isotropic turbulence higher energy is contained at lower wavenumbers; therefore, such

weighting gives higher energy contents at lower wavenumbers in the forcing range that can be seen in the energy spectra of the cases with the deterministic forcing scheme in figures 1(*b*) and 1(*c*). The negative viscosity forcing (2.3), on the other hand, weights relatively more on higher wavenumber shells in the forcing range due to $|\boldsymbol{k}|^2$, leading to higher energy levels at higher forcing wavenumbers. This is consistent with the energy spectra in figures 1(*a*) and 1(*b*) in the forcing range. This trend was also observed in the energy spectra by Jiménez *et al.* (1993) in which a negative viscosity forcing was used.

In order to accurately reproduce the DNS results of Langford & Moser (1999), the deterministic forcing scheme is adopted in the present study.

Appendix B. Energy spectra at $Re_\lambda = 286$

Although the overall energy spectra of the present DNS and those obtained by Chumakov (2008) are similar, a slight underprediction by the present DNS is observed. To investigate the reason for the difference, the energy dissipation rate ε is estimated by

$$\varepsilon = \nu^3/\eta^4, \tag{B1}$$

where η is the Kolmogorov length scale. This allows us to estimate the energy dissipation rate for the DNS result of forced homogeneous isotropic turbulence, as η is available in both the present study and the study by Chumakov (2008). While it is expected for the well-converged statistics of forced homogeneous isotropic turbulence to have ε close to the prescribed mean dissipation rate of 0.12, ε estimated from η of the present DNS result and Chumakov (2008) are 0.12 and 0.16, respectively. Therefore, the DNS database used in the present study is considered to provide better converged statistics, which explains the difference.

Appendix C. *A posteriori* tests with different inputs

In the present study consideration of the resolved stress L_{ij} as an input in addition to the resolved strain-rate tensor $\bar{S}_{ij}$ is found to significantly improve the performance of the ANN-SGS model. The alternative terms of the resolved stress L_{ij} can be found in the literature on various mixed SGS models (Bardina *et al.* 1983; Liu *et al.* 1994; Salvetti & Banerjee 1995; Anderson & Meneveau 1999). Thus, in this section the modified Leonard term ($\mathcal{L}^m_{ij} = \overline{\bar{u}_i\bar{u}_j} - \bar{\bar{u}}_i\bar{\bar{u}}_j$) (Bardina *et al.* 1983; Germano 1986; Salvetti & Banerjee 1995), the resolved stress ($L_{ij} = \widehat{\bar{u}_i\bar{u}_j} - \hat{\bar{u}}_i\hat{\bar{u}}_j$) (Liu *et al.* 1994) and the gradient model term ($\frac{1}{12}\bar{\Delta}^2(\partial\bar{u}_i/\partial x_k)(\partial\bar{u}_j/\partial x_k)$) from the Clark model (Anderson & Meneveau 1999) are considered as inputs to the ANN, in addition to the resolved strain-rate tensor $\bar{S}_{ij}$. The performance of ANN-SGS models are compared by conducting LES of decaying isotropic turbulence with a grid resolution of 48^3 and 24^3.

Figure 34 shows results from LES of decaying homogeneous isotropic turbulence with a grid resolution of 48^3. The ANN-SGS model with $\bar{S}_{ij}$ and the gradient model term as inputs is found to predict the temporal evolution of the resolved kinetic energy most accurately, but shows the largest error in the prediction of energy spectra at $k = 1$. On the other hand, the performance of the ANN-SGS model with $\bar{S}_{ij}$ and the modified Leonard term as inputs is found to be similar to that of the ANN-SGS model with $\bar{S}_{ij}$ and L_{ij} as inputs in predicting the energy spectra and the decaying kinetic energy.

Figure 35 shows results from LES of decaying homogeneous isotropic turbulence with a grid resolution of 24^3. Temporal evolution of the resolved kinetic energy predicted by

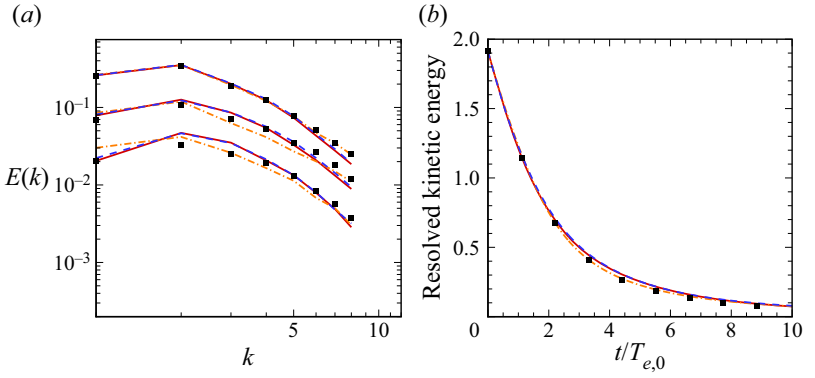

Figure 34. Results from fDNS and LES of decaying isotropic turbulence at the initial Reynolds number Re_λ of 106 with a grid resolution of 48^3. (*a*) Energy spectra at $t/T_{e,0} = 1.1$, 3.3 and 6.6; (*b*) temporal evolution of the resolved kinetic energy. Here ■, fDNS; —— (thick red solid line), ANN-SGS model with $\bar{S}_{ij}$ and L_{ij}; – – – (thick blue dashed line), ANN-SGS model with $\bar{S}_{ij}$ and the modified Leonard term; – – – (thick yellow orange dashed-dot line), ANN-SGS model with $\bar{S}_{ij}$ and the gradient model term.

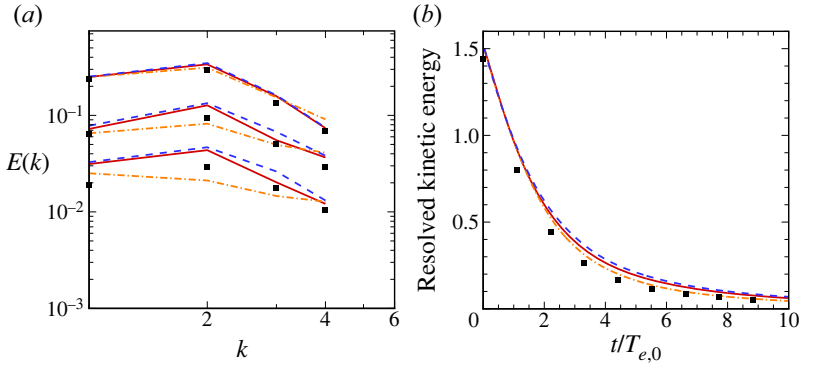

Figure 35. Results from fDNS and LES of decaying isotropic turbulence at the initial Reynolds number Re_λ of 106 with a grid resolution of 24^3 (two-times coarser resolution than that of training data). (*a*) Energy spectra at $t/T_{e,0} = 1.1$, 3.3 and 6.6; (*b*) temporal evolution of the resolved kinetic energy. Here ■, fDNS; —— (thick red solid line), ANN-SGS model with $\bar{S}_{ij}$ and L_{ij}; – – – (thick blue dashed line), ANN-SGS model with $\bar{S}_{ij}$ and the modified Leonard term; – – – (thick yellow orange dashed-dot line), ANN-SGS model with $\bar{S}_{ij}$ and the gradient model term.

the ANN-SGS model with $\bar{S}_{ij}$ and the gradient model term as inputs shows the smallest error (see figure 35*b*). However, this model has significantly large errors in the energy spectra at $k = 2$ (see figure 35*a*). The gradient model is derived using Taylor series expansion of a filtered velocity field with a fourth-order leading error term in $\bar{\Delta}$ (Vreman, Geurts & Kuerten 1996; Horiuti 1997). Therefore, the truncation error of the gradient term increases when grid resolution becomes coarse, which is a possible reason for the inaccurate prediction of the energy spectra in figure 35(*a*). Thus, ANN-SGS models are more robust to the change in grid resolution when the resolved stress L_{ij} or the modified Leonard term $\mathcal{L}^m_{ij}$ is provided as an input in addition to $\bar{S}_{ij}$. In the present study, the resolved stress L_{ij} and $\bar{S}_{ij}$ are considered as the best combination of input variables for the ANN-SGS model, as it shows the best performance and ensures robustness.

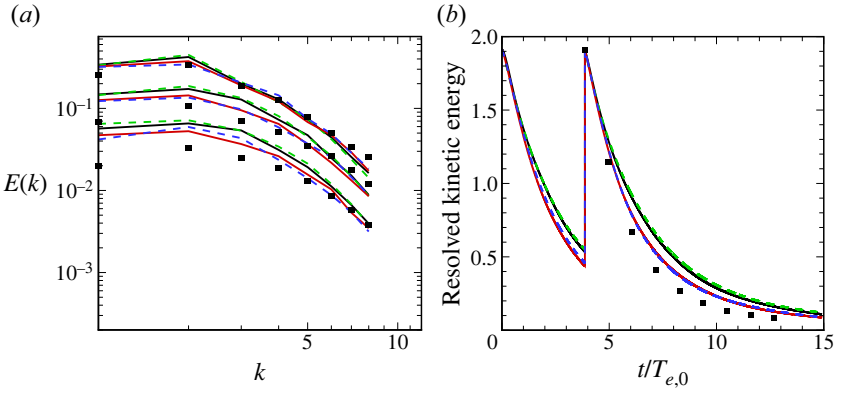

Figure 36. Results from fDNS and LES of decaying isotropic turbulence at the initial Reynolds number Re_λ of 106 with a random-phase initial field. (*a*) Energy spectra at $t/T_{e,0} = 1.1$, 3.3 and 6.6; (*b*) temporal evolution of the resolved kinetic energy. Here ■, fDNS; —— (thick black solid line), DSM; —— (thick red solid line), SL-106H; – – - (thick blue dashed line), SL-286H; – – - (thick green dashed line), S-106H.

Appendix D. *A posteriori* test of decaying isotropic turbulence with a random-phase initial condition

To assess the robustness of the present ANN-SGS models to the initial conditions, LES of decaying isotropic turbulence with a random-phase initial condition is performed using the rescaling method of Kang *et al.* (2003). The three-dimensional energy spectrum from a fully converged flow field of forced isotropic turbulence at $Re_\lambda = 106$ is given as the initial energy distribution. The simulation is started with random-phase Fourier modes until $t/T_{e,0} = 3.87$ when the derivative skewness becomes steady. Thereafter, the velocity field is rescaled to have the initial energy spectrum of fDNS (Kang *et al.* 2003). Results with SL-106H, SL-286H and S-106H are compared with those of DSM and fDNS.

Despite the fact that the random-phase initial field as well as the transient development of the flow is not included in the training data, the performance and stability of ANN-SGS models are maintained. Models SL-106H and SL-286H predict the energy spectra more accurately, whereas DSM and S-106H show large errors at $k \leqslant 5$, as shown in figure 36(*a*). Similarly, SL-106H and SL-286H predict the temporal evolution of the resolved kinetic energy more accurately than DSM and S-106H, as shown in figure 36(*b*).

Appendix E. Comparison of input and output normalisation

Normalisation of the present study is compared with wall-unit normalisation in which input and output variables are normalised in wall units: u_τ and ν/u_τ as velocity and length scales, respectively (i.e. $\bar{S}_{ij}^+ = \frac{1}{2}(\partial \bar{u}_i{}^+/\partial x_j^+ + \partial \bar{u}_j{}^+/\partial x_i^+)$, L_{ij}/u_τ^2, τ_{ij}/u_τ^2). It is found that ANN-SGS mixed models with both the proposed normalisation (discussed in § 3.2) and the wall-unit normalisation provide the same results in LES of channel flow on the trained grid resolution (LES180).

Figure 37 shows LES results of a turbulent channel flow on coarser and finer grid resolutions than a trained resolution (LES180c and LES180f cases). On a coarser resolution (LES180c) the wall-unit normalisation leads to an underestimation of the mean streamwise velocity with similar errors to that of no-SGS and an overestimation of the Reynolds shear stress and r.m.s.velocity fluctuations. In contrast, the Reynolds shear stress and r.m.s.velocity fluctuations by wall-unit normalisation are underestimated on a

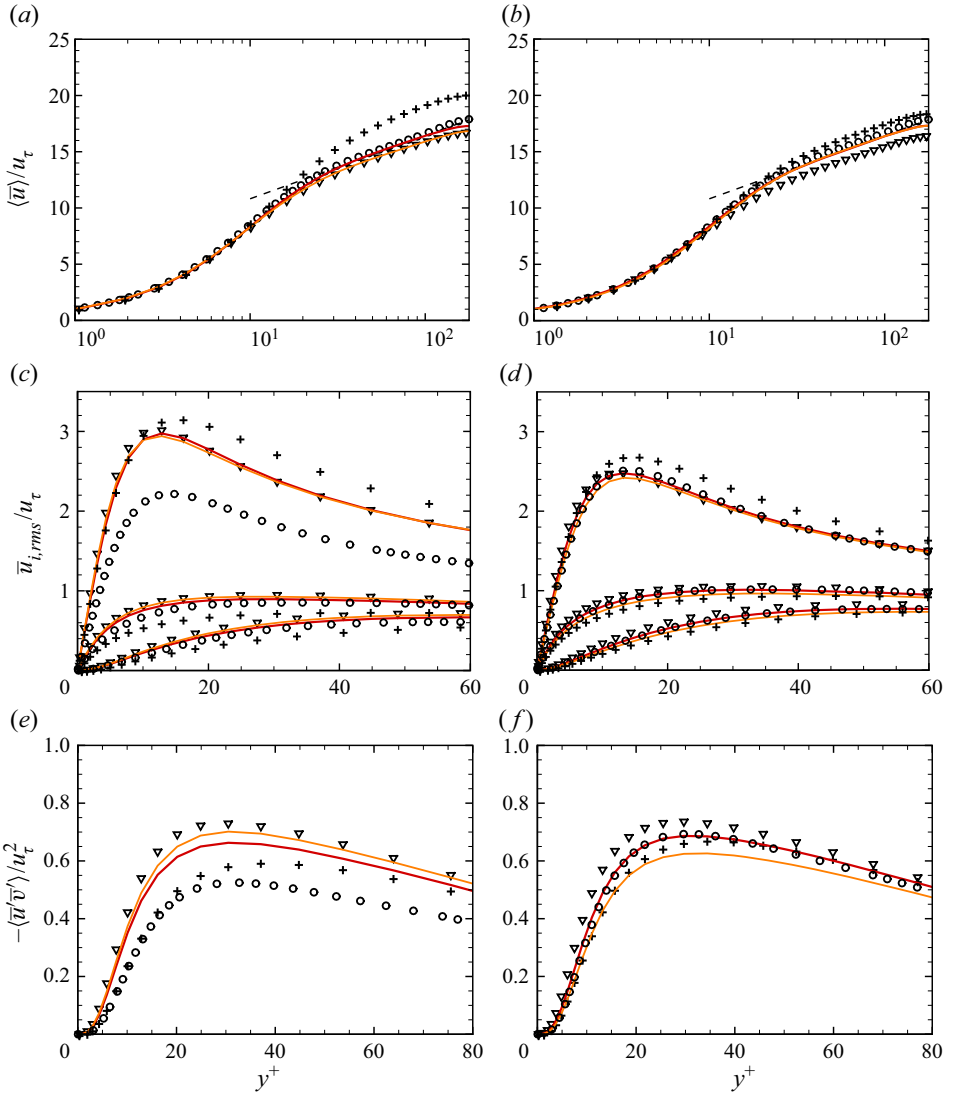

Figure 37. Results from fDNS and LES of a turbulent channel flow at $Re_\tau = 180$ with a grid resolution of $32 \times 48 \times 32$ (*a*,*c*,*e*; LES180c) and $64 \times 64 \times 64$ (*b*,*d*,*f*); LES180f). (*a*,*b*) The mean streamwise velocity; (*c*,*d*) r.m.s. velocity fluctuations; (*e*,*f*) the mean Reynolds shear stress $\langle\bar{u}'\bar{v}'\rangle$, where $\langle\cdot\rangle$ denotes averaging over the x–z plane and time. The three sets of curves in (*c*,*d*) represent $\bar{u}_{rms}/u_\tau$, $\bar{w}_{rms}/u_\tau$ and $\bar{v}_{rms}/u_\tau$ from top to bottom, respectively. Here ◯, fDNS; +, DSM; ∇, no-SGS; —— (thick red solid line), SL-180C with the proposed normalisation (§ 3.2); —— (thick orange solid line), SL-180C with wall-unit normalisation; – – – (thick black dashed line), the law of the wall $\langle\bar{u}\rangle/u_\tau = 0.41^{-1}\log y^+ + 5.2$.

finer resolution (LES180f). This indicates that the normalisation method proposed in the present study shows better generalization to different grid resolutions. Since the wall-unit normalisation does not account for the change of the filter width, the magnitude of the SGS stress is inaccurately predicted on an untrained grid resolution.

For LES of forced and decaying isotropic turbulence, results from the normalisation of input and output variables using the Taylor microscale λ, the r.m.s.velocity fluctuation u' as a characteristic length and velocity scales are compared with those obtained using

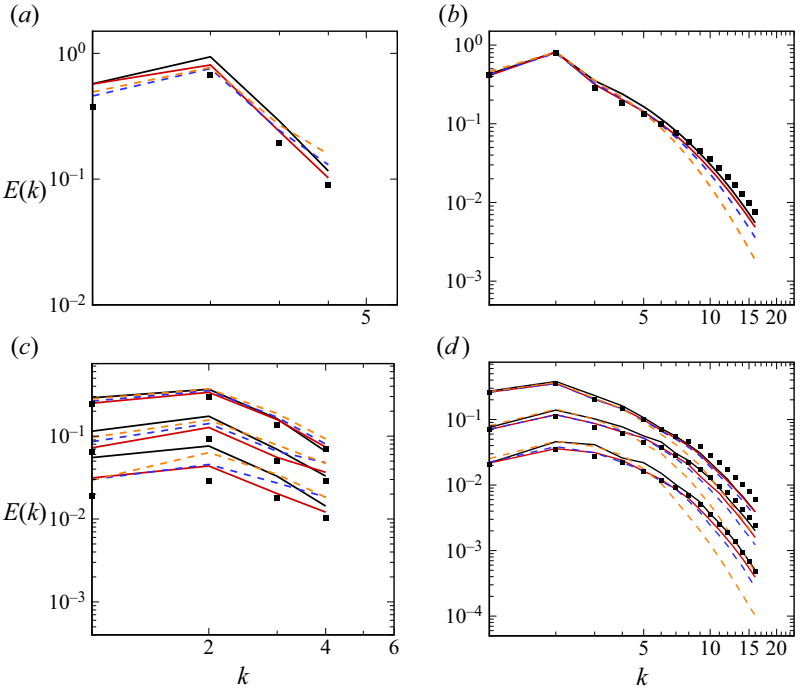

Figure 38. Energy spectra from fDNS and LES of forced homogeneous isotropic turbulence at $Re_\lambda = 106$ with a grid resolution of (*a*) 24^3 and (*b*) 96^3. Energy spectra from fDNS and LES of decaying homogeneous isotropic turbulence at the initial $Re_\lambda = 106$ with a grid resolution of (*c*) 24^3 and (*d*) 96^3 (coarser and finer resolution by a factor of 2 than that of training data, respectively). Here ■, fDNS; —— (thick black solid line), DSM; —— (thick red solid line), SL-106H with output normalisation using $\langle|\tau_{grad}|\rangle$; – – – (thick blue dashed line), SL-106H with output normalisation using $\langle|L|\rangle$; – – – (thick orange dashed line), SL-106H with normalisation using u' and λ.

the normalisation method proposed in the present study. Energy spectra from LES of forced and decaying isotropic turbulence on an untrained grid resolution are presented in figure 38. On a coarser resolution (24^3), normalisation with u' and λ results in overprediction of energy spectra at high wavenumbers $k \geqslant 3$. Moreover, the errors at $k = 2$ significantly increase as the flow decays when the input and output are normalised with u' and λ (figure 38*c*). In figures 38(*b*) and 38(*d*), normalisation with u' and λ also leads to underprediction of energy spectra at high wavenumbers $k > 6$ on a finer grid resolution (96^3), and errors at $k \leqslant 4$ increase when the flow decays. Similarly to the discussion about wall-unit normalisation in channel flow, since the normalisation using u' and λ is not capable of accounting for the change of the SGS stress magnitude, the model becomes inaccurate on an untrained grid resolution.

Lastly, results obtained with output normalisation using the resolved stress tensor ($\tau_{ij}^* = \tau_{ij}/\langle|L|\rangle$) and the gradient term ($\tau_{ij}^* = \tau_{ij}/\langle|\tau_{grad}|\rangle$) are compared. Although the use of $\langle|L|\rangle$ for output normalisation tends to overpredict energy spectra on a coarser resolution (24^3), it produces similar results in forced and decaying isotropic turbulence to those of the case using $\langle|\tau_{grad}|\rangle$ for output normalisation on a finer grid resolution (96^3).

Therefore, it is concluded that the gradient term is the best option for normalising the output variable in homogeneous isotropic turbulence. Nevertheless, output normalisation

with $\langle |L| \rangle$ also shows generalization performance comparable to that of output normalisation with the gradient term on a sufficient grid resolution and considerably better generalization performance compared with normalisation using characteristic velocity and length scales of target flows (e.g. u' and λ for isotropic turbulence or u_τ and ν/u_τ for channel flow), and it has an advantage for LES of wall-bounded flow. It is worth noting that an ANN trained with normalisation using characteristic length and velocity scales of certain flow is not applicable for untrained flow types since the characteristic scales are different.

References

Anderson, R. & Meneveau, C. 1999 Effects of the similarity model in finite-difference LES of isotropic turbulence using a Lagrangian dynamic mixed model. *Flow Turbul. Combust.* **62**, 201–225.

Bardina, J., Ferziger, J. & Reynolds, W.C. 1983 Improved turbulence models based on large eddy simulation of homogeneous, incompressible, turbulent flows. PhD thesis, Stanford University, Stanford, CA.

Bose, S.T., Moin, P. & You, D. 2010 Grid-independent large-eddy simulation using explicit filtering. *Phys. Fluids* **22** (10), 105103.

Cabot, W. 1994 Local dynamic subgrid-scale models in channel flow. In *Annual Research Briefs – 1994*, pp. 143–159. Center for Turbulence Research, Stanford University/NASA Ames Research Center.

Canuto, C., Hussaini, M., Quarteroni, A. & Zang, T. 1988 *Spectral Methods in Fluid Dynamics*. Springer.

Chumakov, S.G. 2007 Scaling properties of subgrid-scale energy dissipation. *Phys. Fluids* **19** (5), 058104.

Chumakov, S.G. 2008 *A priori* study of subgrid-scale flux of a passive scalar in isotropic homogeneous turbulence. *Phys. Rev.* E **78** (3), 036313.

Deardorff, J.W. 1970 A numerical study of three-dimensional turbulent channel flow at large Reynolds numbers. *J. Fluid Mech.* **41** (2), 453–480.

Gawlikowski, J., Tassi, C.R.N., Ali, M., Lee, J., Humt, M., Feng, J., Kruspe, A., Triebel, R., Jung, P., Roscher, R., *et al.* 2021 A survey of uncertainty in deep neural networks. arXiv:2107.03342.

Germano, M. 1986 A proposal for a redefinition of the turbulent stresses in the filtered Navier–Stokes equations. *Phys. Fluids* **29** (7), 2323–2324.

Germano, M., Piomelli, U., Moin, P. & Cabot, W.H. 1991 A dynamic subgrid-scale eddy viscosity model. *Phys. Fluids* A **3** (7), 1760.

Horiuti, K. 1997 A new dynamic two-parameter mixed model for large-eddy simulation. *Phys. Fluids* **9** (11), 3443–3464.

Inagaki, K. & Kobayashi, H. 2020 Role of various scale-similarity models in stabilized mixed subgrid-scale model. *Phys. Fluids* **32** (7), 075108.

Jiménez, J., Wray, A.A., Saffman, P.G. & Rogallo, R.S. 1993 The structure of intense vorticity in isotropic turbulence. *J. Fluid Mech.* **255**, 65–90.

Kang, H.S., Chester, S. & Meneveau, C. 2003 Decaying turbulence in an active-grid-generated flow and comparisons with large-eddy simulation. *J. Fluid Mech.* **480**, 129–160.

Kang, M. & You, D. 2021 Development of numerical methods and subgrid-scale models for compressible large eddy simulation in complex geometries. PhD thesis, Pohang University of Science and Technology, Pohang.

Kim, J., Kim, H., Kim, J. & Lee, C. 2022 Deep reinforcement learning for large-eddy simulation modeling in wall-bounded turbulence. *Phys. Fluids* **34** (10), 105132.

Langford, J.A. & Moser, R.D. 1999 Optimal LES formulations for isotropic turbulence. *J. Fluid Mech.* **398**, 321–346.

Lilly, D.K. 1967 The representation of small-scale turbulence in numerical simulation experiments. In *Proceedings of the IBM Scientific Computing Symposium on Environmental Science, Yorktown Heights, NY* (ed. H.H. Goldstine), pp. 195–210.

Lilly, D.K. 1992 A proposed modification of the Germano subgrid-scale closure method. *Phys. Fluids* A **4** (3), 633.

Liu, S., Meneveau, C. & Katz, J. 1994 On the properties of similarity subgrid-scale models as deduced from measurements in a turbulent jet. *J. Fluid Mech.* **275**, 83–119.

Lumley, J.L. & Newman, G.R. 1977 The return to isotropy of homogeneous turbulence. *J. Fluid Mech.* **82** (1), 161–178.

MACHIELS, L. 1997 Predictability of small-scale motion in isotropic fluid turbulence. *Phys. Rev. Lett.* **79** (18), 3411.

MAULIK, R., SAN, O., RASHEED, A. & VEDULA, P. 2018 Data-driven deconvolution for large eddy simulations of Kraichnan turbulence. *Phys. Fluids* **30** (12), 125109.

MAULIK, R., SAN, O., RASHEED, A. & VEDULA, P. 2019 Subgrid modelling for two-dimensional turbulence using neural networks. *J. Fluid Mech.* **858**, 122–144.

MENEGUZ, E. & REEKS, M.R. 2011 Statistical properties of particle segregation in homogeneous isotropic turbulence. *J. Fluid Mech.* **686**, 338–351.

MOHAN, P., FITZSIMMONS, N. & MOSER, R.D. 2017 Scaling of Lyapunov exponents in homogeneous isotropic turbulence. *Phys. Rev. Fluids* **2** (11), 114606.

MORENO-TORRES, J.G., RAEDER, T., ALAIZ-RODRÍGUEZ, R., CHAWLA, N.V. & HERRERA, F. 2012 A unifying view on dataset shift in classification. *Pattern Recogn.* **45** (1), 521–530.

MORINISHI, Y., LUND, T.S., VASILYEV, O.V. & MOIN, P. 1998 Fully conservative higher order finite difference schemes for incompressible flow. *J. Comput. Phys.* **143** (1), 90–124.

MORINISHI, Y. & VASILYEV, O.V. 2001 A recommended modification to the dynamic two-parameter mixed subgrid scale model for large eddy simulation of wall bounded turbulent flow. *Phys. Fluids* **13** (11), 3400–3410.

PARK, J. & CHOI, H. 2021 Toward neural-network-based large eddy simulation: application to turbulent channel flow. *J. Fluid Mech.* **914**, A16.

PARK, N., LEE, J. & CHOI, H. 2005 Toward improved consistency of *a priori* tests with *a posteriori* tests in large eddy simulation. *Phys. Fluids* **17** (1), 015103.

PARK, N. & MAHESH, K. 2009 Reduction of the germano-identity error in the dynamic smagorinsky model. *Phys. Fluids* **21** (6), 065106.

PASZKE, A., GROSS, S., CHINTALA, S., CHANAN, G., YANG, E., DEVITO, Z., LIN, Z., DESMAISON, A., ANTIGA, L. & LERER, A. 2017 Automatic differentiation in PyTorch. In *31st Conference on Neural Information Processing Systems (NIPS 2017), Long Beach, CA*.

PIOMELLI, U., MOIN, P. & FERZIGER, J.H. 1988 Model consistency in large eddy simulation of turbulent channel flows. *Phys. Fluids* **31** (7), 1884–1891.

POPE, S.B. 2001 *Turbulent Flows*. Cambridge University Press.

QUIÑONERO-CANDELA, J., SUGIYAMA, M., SCHWAIGHOFER, A. & LAWRENCE, N.D. 2009 *Dataset Shift in Machine Learning (Neural Information Processing)*. MIT.

RASAM, A., POURANSARI, Z., VERVISCH, L. & JOHANSSON, A.V. 2016 Assessment of subgrid-scale stress statistics in non-premixed turbulent wall-jet flames. *J. Turbul.* **17** (5), 471–490.

SALVETTI, M.V. & BANERJEE, S. 1995 A priori tests of a new dynamic subgrid-scale model for finite-difference large-eddy simulations. *Phys. Fluids* **7** (11), 2831–2847.

DA SILVA, C.B. & MÉTAIS, O. 2002 On the influence of coherent structures upon interscale interactions in turbulent plane jets. *J. Fluid Mech.* **473**, 103–145.

SILVIS, M.H., REMMERSWAAL, R.A. & VERSTAPPEN, R. 2017 Physical consistency of subgrid-scale models for large-eddy simulation of incompressible turbulent flows. *Phys. Fluids* **29** (1), 015105.

SMAGORINSKY, J. 1963 General circulation experiments with the primitive equations: I. The basic experiment. *Mon. Weath. Rev.* **91** (3), 99–164.

SOLA, J. & SEVILLA, J. 1997 Importance of input data normalization for the application of neural networks to complex industrial problems. *IEEE Trans. Nucl. Sci.* **44** (3), 1464–1468.

VASILYEV, O.V., LUND, T.S. & MOIN, P. 1998 A general class of commutative filters for LES in complex geometries. *J. Comput. Phys.* **146** (1), 82–104.

VREMAN, A.W. 2004 An eddy-viscosity subgrid-scale model for turbulent shear flow: algebraic theory and applications. *Phys. Fluids* **16** (10), 3670–3681.

VREMAN, B., GEURTS, B. & KUERTEN, H. 1994 On the formulation of the dynamic mixed subgrid-scale model. *Phys. Fluids* **6** (12), 4057–4059.

VREMAN, B., GEURTS, B. & KUERTEN, H. 1996 Large-eddy simulation of the temporal mixing layer using the Clark model. *Theor. Comput. Fluid Dyn.* **8** (4), 309–324.

WANG, Z., LUO, K., LI, D., TAN, J. & FAN, J. 2018 Investigations of data-driven closure for subgrid-scale stress in large-eddy simulation. *Phys. Fluids* **30** (12), 125101.

XIE, C., LI, K., MA, C. & WANG, J. 2019 Modeling subgrid-scale force and divergence of heat flux of compressible isotropic turbulence by artificial neural network. *Phys. Rev. Fluids* **4** (10), 104605.

XIE, C. & WANG, J. 2019 Artificial neural network approach to large-eddy simulation of compressible isotropic turbulence. *Phys. Rev.* E **99** (5), 053113.

XIE, C., WANG, J. & WEINAN, E. 2020*a* Modeling subgrid-scale forces by spatial artificial neural networks in large eddy simulation of turbulence. *Phys. Rev. Fluids* **5** (5), 054606.

XIE, C., YUAN, Z. & WANG, J. 2020*b* Artificial neural network-based nonlinear algebraic models for large eddy simulation of turbulence. *Phys. Fluids* **32** (11), 115101.

XU, B., WANG, N., CHEN, T. & LI, M. 2015 Empirical evaluation of rectified activations in convolutional network. arXiv:1505.00853.

YANG, C.Y. & LEI, U. 1998 The role of the turbulent scales in the settling velocity of heavy particles in homogeneous isotropic turbulence. *J. Fluid Mech.* **371**, 179–205.

YOU, D. & MOIN, P. 2007 A dynamic global-coefficient subgrid-scale eddy-viscosity model for large-eddy simulation in complex geometries. *Phys. Fluids* **19** (6), 065110.

YOU, D. & MOIN, P. 2009 A dynamic global-coefficient subgrid-scale model for large-eddy simulation of turbulent scalar transport in complex geometries. *Phys. Fluids* **21** (4), 045109.

YUAN, Z., XIE, C. & WANG, J. 2020 Deconvolutional artificial neural network models for large eddy simulation of turbulence. *Phys. Fluids* **32** (11), 115106.

ZANG, Y., STREET, R.L. & KOSEFF, J.R. 1993 A dynamic mixed subgrid-scale model and its application to turbulent recirculating flows. *Phys. Fluids* A **5** (12), 3186–3196.

ZHOU, Z., HE, G., WANG, S. & JIN, G. 2019 Subgrid-scale model for large-eddy simulation of isotropic turbulent flows using an artificial neural network. *Comput. Fluids* **195**, 104319.